AD-A199 582

②

DTIC
ELECTE
SEP 3 0 1988
S D
D

REPORT DOCUMENTATION PAGE

Form Approved
OMB No. 0704-0188

1a. REPORT SECURITY CLASSIFICATION UNCLASSIFIED	1b. RESTRICTIVE MARKINGS
2a. SECURITY CLASSIFICATION AUTHORITY	3. DISTRIBUTION/AVAILABILITY OF REPORT Approved for public release; distribution unlimited.
2b. DECLASSIFICATION/DOWNGRADING SCHEDULE	
4. PERFORMING ORGANIZATION REPORT NUMBER(S) N00014-85-C-0141-TR7	5. MONITORING ORGANIZATION REPORT NUMBER(S)

6a. NAME OF PERFORMING ORGANIZATION Washington State University	6b. OFFICE SYMBOL (If applicable)	7a. NAME OF MONITORING ORGANIZATION Office of Naval Research
6c. ADDRESS (City, State, and ZIP Code) Department of Physics Washington State University Pullman, WA 99164-2814		7b. ADDRESS (City, State, and ZIP Code) Physics Division Code 1112 Arlington, VA 22217-5000
8a. NAME OF FUNDING/SPONSORING ORGANIZATION	8b. OFFICE SYMBOL (If applicable)	9. PROCUREMENT INSTRUMENT IDENTIFICATION NUMBER N00014-85-C-0141
8c. ADDRESS (City, State, and ZIP Code)		10. SOURCE OF FUNDING NUMBERS

PROGRAM ELEMENT NO.	PROJECT NO.	TASK NO.	WORK UNIT ACCESSION NO.
61153N	4126934		

11. TITLE (Include Security Classification)
Observation of Brewster Angle Light Scattering from Air Bubbles Rising in Water

12. PERSONAL AUTHOR(S)
Baumer, S. M.

13a. TYPE OF REPORT	13b. TIME COVERED	14. DATE OF REPORT (Year, Month, Day)	15. PAGE COUNT
Technical	FROM 870715 TO 880815	880825	xii + 104 = 116

16. SUPPLEMENTARY NOTATION
This is the M.S. thesis of from Stefan M. Baumer. The contract P.I. was P. L. Marston, Telephone (509) 335-5343 or 335-5931.

17. COSATI CODES			18. SUBJECT TERMS (Continue on reverse if necessary and identify by block number)
FIELD	GROUP	SUB-GROUP	Light Scattering, Microbubbles, Bubbles, Bubble Detection, Cavitation. Theses
20	01		
20	06		

19. ABSTRACT (Continue on reverse if necessary and identify by block number)

Air bubbles rising freely through distilled water were illuminated by laser light with incident polarization of the electric field parallel to the plane of incidence. The radii a of the bubbles investigated were in the range $50\ \mu m \leq a \leq 100\ \mu m$. At Brewster's angle of incidence $i_B = \arctan(m) = 36.9°$, the Fresnel reflection coefficient vanishes, where m is the relative index of refraction for a water-air interface, $m = 0.75$. Therefore a minimum in scattered intensity should be observed at the Brewster scattering angle $\theta_B = 180° - 2i_B = 106.2°$. Furthermore interference patterns caused by different classes of rays should

20. DISTRIBUTION/AVAILABILITY OF ABSTRACT ☒ UNCLASSIFIED/UNLIMITED ☐ SAME AS RPT ☐ DTIC USERS	21. ABSTRACT SECURITY CLASSIFICATION UNCLASSIFIED	
22a. NAME OF RESPONSIBLE INDIVIDUAL L. E. Hargrove	22b. TELEPHONE (Include Area Code) (202) 696-4221	22c. OFFICE SYMBOL ONR Code 1112

DD Form 1473, JUN 86 Previous editions are obsolete. SECURITY CLASSIFICATION OF THIS PAGE
UNCLASSIFIED

88 9 30 034

19. ABSTRACT (continued)

change drastically for angles around Brewster scattering angle, θ_B. Experiments were done to detect these two phenomena by photographing the scattering light. The scattered intensity as a function of angle was inferred by scanning the photographs with a microdensitometer. In order to confirm the experimental results, they were compared with Mie theory calculation for scattering from spherical bubbles. Features of the scattering pattern due to ray interference could be understood using geometrical optics. The experiment confirmed that the observed features of the scattering pattern near θ_B are those predicted of a bubble having a clean surface. Since it has been previously calculated that the scattering pattern would be significantly different near θ_B if the surface of the bubble is coated by contamination, it is plausible that such a coating could be characterized optically. It is thought that the acoustics and dynamics of microbubbles in the ocean, or in other environments, may be affected by such coatings. The present observations could be compared with observations of the scattering from coated bubbles if such observations become available. Keywords → to field 18

Theta sub B

OBSERVATION OF BREWSTER ANGLE LIGHT SCATTERING FROM AIR BUBBLES RISING IN WATER

By

STEFAN M. BÄUMER

A thesis submitted in partial fulfillment of the requirements
for the degree

MASTER OF SCIENCE IN PHYSICS

WASHINGTON STATE UNIVERSITY
DEPARTMENT OF PHYSICS

August 1988

Technical Report, Contract N00014-85-C-0141

To the Faculty of Washington State University:

The members of the Committee appointed to examine the thesis of *STEFAN BÄUMER* find it satisfactory and recommend that it be accepted.

Philip L. Marston
Chair

ACKNOWLEGMENTS

I would like to express my gratitude to Dr. Philip L. Marston. As my thesis advisor he was of great help in preparing this work. It was always inspiring and motivating to discuss all problems and results with him. Thank you for your patience and advice.

Furthermore I would like to thank all my fellow graduate students and the members of the Marston research group for the positive, friendly and open atmosphere in this department. Among these I would like to give special thanks to W. Pat Arnott for all the helpful discussions concerning the experiment and my many computing questions. I enjoyed being here..

I am also grateful to the Washington State University Shock Dynamics Research Laboratory for letting me use their microdensitometer. Without this devise large parts of the data analysis would not have been possible. Also I would like to thank the staff of the Washington State University Technical Services Instrument Shop for their assistance in building the scattering chamber.

For funding I would like to express gratitude to the Office of Naval Research (Physics Division). Their funding provided the equipment necessary to do this research. My stay at Washington State University (WSU) was sponsored in part by the Office of International education at WSU and by the Landesamt für Ausbildungsförderung, Hamburg, Germany. I am very grateful for their support.

OBSERVATION OF BREWSTER ANGLE LIGHT SCATTERING FROM AIR BUBBLES RISING IN WATER

Abstract

by Stefan M. Bäumer, M.S.
Washington State University
August 1988

Chair: Philip L. Marston

Air bubbles rising freely through distilled water were illuminated by laser light with incident polarization of the electric field parallel to the plane of incidence. The radii a of the bubbles investigated were in the range $50\ \mu m \le a \le 100\ \mu m$. At Brewster's angle of incidence $i_B = \arctan(m) = 36.9°$, the Fresnel reflection coefficient vanishes, where m is the relative index of refraction for a water - air interface, $m = 0.75$. Therefore a minimum in scattered intensity should be observed at the Brewster scattering angle $\theta_B = 180° - 2i_B = 106.2°$. Furthermore interference patterns caused by different classes of rays should change drastically for angles around Brewster scattering angle θ_B. Experiments were done to detect these two phenomena by photographing the scattered light. The scattered intensity as a function of angle was inferred by scanning the photographs with a microdensitometer. In order to confirm the experimental results, they were compared with Mie theory calculation for scattering from spherical bubbles. Features of the scattering pattern due to ray interference could be understood using geometrical optics. The experiment confirmed that the observed features of the scattering pattern near θ_B are those predicted of a bubble having a clean surface. Since it has been previously calculated that the scattering pattern would be significantly different near θ_B if the surface of the bubble is

coated by contamination, it is plausible that such a coating could be characterized optically. It is thought that the acoustics and dynamics of microbubbles in the ocean, or in other environments, may be affected by such coatings. The present observations could be compared with observations of the scattering from coated bubbles if such observations become available.

TABLE OF CONTENTS

Page

Chapter

LIST OF TABLES

LIST OF ILLUSTRATIONS

Page

Meinen Eltern

Chapter 1

Introduction

Light scattering from small particles has been of interest for a long time for various reasons. One particular class of scatterers has attracted some recent attention: air bubbles in dielectric media. Some research has been done in this field experimentally and theoretically[1-11]. However there are still areas in which little or no research was done. One of these areas is Brewster angle light scattering. Investigations on this particular topic in scattering will be presented in the following work. Experimental data will be shown and compared with theoretical results. The motivation for this work is twofold: interest in the phenomena itself and possible applications for identifying and classifying microbubbles in water[7].

First the theory of Brewster's angle will be described and a model will be presented which was used in understanding the phenomena and in calculating theoretical data. Chapter three describes the experiment, and in chapters four and five results will be presented and discussed.

Chapter 2

Theory

2.1 Derivation of Brewster's angle

If an electromagnetic light wave propagates through a medium and hits an interface with another medium, two phenomena occur: refraction and reflection. Refraction and reflection are qualitatively described by Snell's law and the law of reflection. The direction of the refracted light is given by Snell's law

$$n_1 \sin i_1 = n_1' \sin i_1' \qquad (1)$$

where n_1 and n_1' are the indices of refraction for media 1 and 2, i_1 and i_1' are angle of incidence and angle of refraction.

The direction of the reflected light is determined by the law of reflection

$$i_1 = i_r$$

where i_r is the angle of reflection.

In addition there is the boundary condition that both the reflected and refracted ray are in the same plane as the incident ray.

If we are not only interested in the direction of the light but also in the magnitude of the reflected and refracted light wave, we have to use Fresnel's reflection and transmission coefficients.

$$E_{out} = r\, E_{in}$$

The outgoing electric field amplitude E_{out} equals the Fresnel coefficient r times the incident electric field amplitude E_{in}. The Fresnel coefficients depend on i_1 and i_1' and also on the incident polarization of the light. Therefore we have four such coefficients, two for reflection and two for transmission. The following list is taken from Klein-Furtak[19].

$$r_p = \frac{\tan(i_1 - i_1')}{\tan(i_1 + i_1')}$$ Fresnel reflection coefficient, electric field parallel polarized

$$r_s = -\frac{\sin(i_1 - i_1')}{\sin(i_1 + i_1')}$$ Fresnel reflection coefficient, electric field perpendicular polarized

$$t_p = \frac{2 \sin i_1' \cos i_1}{\sin(i_1 + i_1') \cos(i_1 - i_1')}$$ Fresnel transmission coefficient electric field parallel polarized

$$t_s = \frac{2 \sin i_1' \cos i_1}{\sin(i_1 + i_1')}$$ Fresnel transmission coefficient, electric field perpendicular polarized

Parallel and perpendicular always refer to the plane of incidence, which in this case is identical with the plane of the paper in the following figures.

As we examine the reflection coefficient for parallel polarized light, we notice that if

$$i_1 + i_1' = 90° \qquad (2)$$

$$\lim_{i_1 + i_1' \to 90°} r_p = \lim \frac{\tan(i_1 - i_1')}{\tan(i_1 + i_1')} = 0$$

The reflection coefficient for parallel polarized light incident r_p goes to zero. Applying this special condition (2) to Snell's law (1) we find

$$n_1 \sin i_1 = n_1' \sin i_1' = n_1' \sin(90° - i_1) = n_1' \cos i_1$$

$$\tan i_1 = \frac{n_1'}{n_1} \qquad (3)$$

So condition (2) leads to the definition of a special angle of incidence.The angle defined through equation (3) is called Brewster's angle i_B, named after Sir David Brewster (1781 - 1868), who derived this law in 1815 empirically[21]. At Brewster's angle no parallel polarized light is reflected, all parallel polarized light is transmitted.

2.2 Brewster angle and Brewster scattering angle for air bubbles in water

Now we want to apply this general relation to the specific case of the water - air interface of an air bubble freely rising through water. First of all the size range of interest for bubbles in this experiment is $50\ \mu m \leq a \leq 100\ \mu m$, where a is the bubble radius. As shown in previous work[4,11,13] microbubbles of that size can be well modeled as spheres. The sphere model will be used throughout all calculations. Since the radii of the bubbles of interest are a lot larger than the wavelength of the light, we can treat all interfaces of the bubbles locally as plane interfaces, and apply the above derived formulas directly.

If a light wave is incident on the water - air interface, as shown in figure 1, it makes a local angle of incidence i with the local normal defined by the extension of a line from the

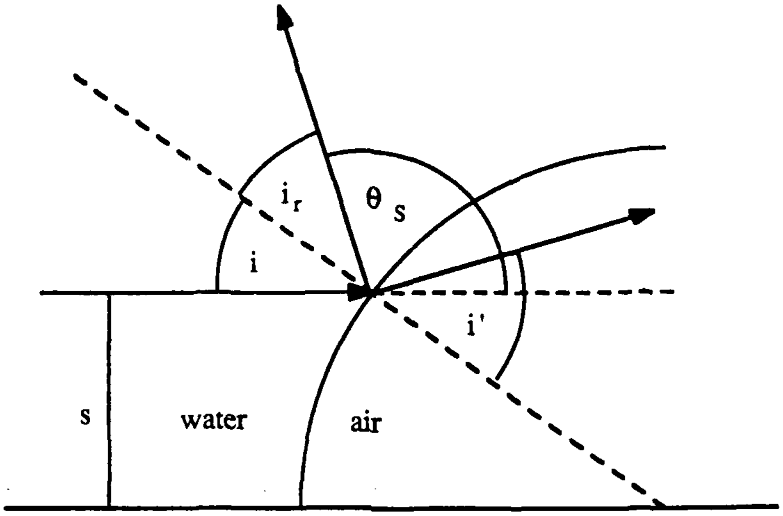

Figure 1: Geometry of light rays incident onto an air bubble in water

center of the bubble to the point of incidence. Applying Snell's law and the law of reflection we also mark the angle of reflection i_r which has the same magnitude as i, and the angle of refraction i'. The scattering angle θ_S is defined by the forward scattering direction as indicated in figure 1. Lastly there is the impact parameter s, which is defined by the distance of the incident light ray to the optical axis, where the optical axis goes through the center of the bubble. Now that we have named all components we need to completely describe the geometry of our problem. The next step is to calculate Brewster's angle in case of water to air transmission. Using equation (3) we calculate

$$i_B = \arctan m = \arctan 0.75 = 36.9° \qquad (4)$$

which is Brewster's angle for light going from water into air. In this equation m is the relative index of refraction defined by

$$m = \frac{n_a}{n_w} \qquad (5)$$

As the numerical value m = 0.75 was taken. Although the ratio n_a/n_w of the actual values for n_a and n_w at 514.5 nm is slightly different (n_a=1.0002929, n_w=1.334, m=0.74984)[15,12], m=0.75 has proven to be a very good approximation in all calculations[1,4]. Going back to figure (1) we find the scattering angle to be

$$\theta_S = 180° - 2\,i \qquad (6)$$

Using the Brewster angle incident (equation 4), we can compute the Brewster scattering angle θ_B.

$$\theta_B = 180° - 2\,i_B = 106.2°$$

Besides understanding how to model the reflection of light of the surface of a bubble we also have to know what happens to the light rays that are transmitted into the air bubble. It is of particular interest whether light with an incident angle other than Brewster's angle is transmitted out of the bubble at the Brewster scattering angle θ_B after internal reflections . This is because if light is emitted near the same direction as Brewster scattering angle, we expect to see modulated interference patterns, because the observed light comes from the same source but travels paths of different lengths. The interference patterns then provide information about the bubble. To gain information about all light rays scattered in the same direction we apply the following generalized formula for finding scattering angles from bubbles[11,17]:

$$\theta_S = h(2pi_r - 2i - \pi (p - 2g - 1)) \qquad (7)$$

θ_S, i, i_r are as before and

p number of internal chords for the light ray

g number of trips around the bubble for internally reflected light rays

h +1 for rays entering above the optical axis

-1 for rays entering below the optical axis

For the special case of $p = 0$, $g = 0$ we get the result of equation (6), Brewster's scattering angle. If we scan through different incident angles from 0° to the critical angle $i_c=\arcsin(m)$, we see whether θ_S goes through Brewster's scattering angle. We do not get a contribution from one-chord rays, but one two-chord ray and two three-chord rays contribute (table 1). However finding the exact angle of incidence for those rays is a non trivial problem, since Snell's law (1) and equation (7) have to be solved simultaneously. That leads to a transcendental equation which we solved numerically by rewriting equations (4) and (6) as

$$\theta_B = 2 \arctan (m^{-1}) \qquad (8)$$

and finding the roots of $f(i) = 0$, where

$$f(i) = 2 \arctan(m^{-1}) - h(2pi_r - 2i - \pi (p - 2g - 1)) \qquad (9)$$

The result is shown in table 2.

With this information we are now able to calculate the impact parameters s for the relevant rays

$$s = a \sin i \qquad (10)$$

Knowing the impact parameters and applying Snell's law enables us to draw a ray diagram for Brewster angle scattering (figure 2). In the notation used, the first number stands for

Table 1: Numerical search for Brewster scattering angle for different types of rays

```
Number of chords in the bubble
2
Number of trips around the bubble
0

Angle of incidence   Scattering angle
        1               176.6665
        2               173.3316
        3               169.9943
        4               166.6531
        5               163.3069
        6               159.9541
        7               156.5936
        8               153.2239
        9               149.8436
       10               146.4511
       11               143.0450
       12               139.6236
       13               136.1853
       14               132.7281
       15               129.2503
       16               125.7499
       17               122.2246
       18               118.6722
       19               115.0902
       20               111.4759
       21               107.8265
       22               104.1388
       23               100.4093
       24                96.6344
       25                92.8097
       26                88.9307
       27                84.9923
       28                80.9887
       29                76.9133
       30                72.7587
       31                68.5167
       32                64.1775
       33                59.7298
       34                55.1606
       35                50.4544
       36                45.5925
       37                40.5527
       38                35.3073
       39                29.8218
       40                24.0521
       41                17.9406
       42                11.4091
       43                 4.3477
       44                -3.4068
       45               -12.1151
       46               -22.2425
       47               -34.7835
       48               -52.9896
```

```
Number of chords in the bubble
3
Number of trips around the bubble
0

Angle of incidence   Scattering angle
        1                353.9997
        2                347.9975
        3                341.9915
        4                335.9797
        5                329.9603
        6                323.9312
        7                317.8904
        8                311.8358
        9                305.7654
       10                299.6767
       11                293.5675
       12                287.4355
       13                281.2779
       14                275.0922
       15                268.8755
       16                262.6248
       17                256.3369
       18                250.0083
       19                243.6353
       20                237.2139
       21                230.7397
       22                224.2082
       23                217.6140
       24                210.9516
       25                204.2146
       26                197.3961
       27                190.4885
       28                183.4830
       29                176.3699
       30                169.1381
       31                161.7751
       32                154.2662
       33                146.5947
       34                138.7409
       35                130.6815
       36                122.3888
       37                113.8291
       38                104.9609
       39                 95.7327
       40                 86.0782
       41                 75.9109
       42                 65.1136
       43                 53.5215
       44                 40.8898
       45                 26.8273
       46                 10.6362
       47                 -9.1828
       48                -37.4844
```

```
Number of chords in the bubble
3
Number of trips around the bubble
1

Angle of incidence   Scattering angle
        1                   6.0003
        2                  12.0025
        3                  18.0085
        4                  24.0203
        5                  30.0397
        6                  36.0688
        7                  42.1096
        8                  48.1641
        9                  54.2346
       10                  60.3233
       11                  66.4325
       12                  72.5646
       13                  78.7221
       14                  84.9078
       15                  91.1245
       16                  97.3752
       17                 103.6631
       18                 109.9918
       19                 116.3648
       20                 122.7861
       21                 129.2603
       22                 135.7918
       23                 142.3860
       24                 149.0484
       25                 155.7854
       26                 162.6039
       27                 169.5115
       28                 176.5170
       29                 183.6301
       30                 190.8619
       31                 198.2249
       32                 205.7338
       33                 213.4053
       34                 221.2591
       35                 229.3185
       36                 237.6112
       37                 246.1709
       38                 255.0391
       39                 264.2673
       40                 273.9218
       41                 284.0891
       42                 294.8864
       43                 306.4785
       44                 319.1102
       45                 333.1727
       46                 349.3638
       47                 369.1828
       48                 397.4844
```

Ray	Angle of incidence
(2,1)	21.42605536°
(3,1)	37.85584125°
(3,2)	17.41117969°

Table 2: Angle of incident for all contributing rays

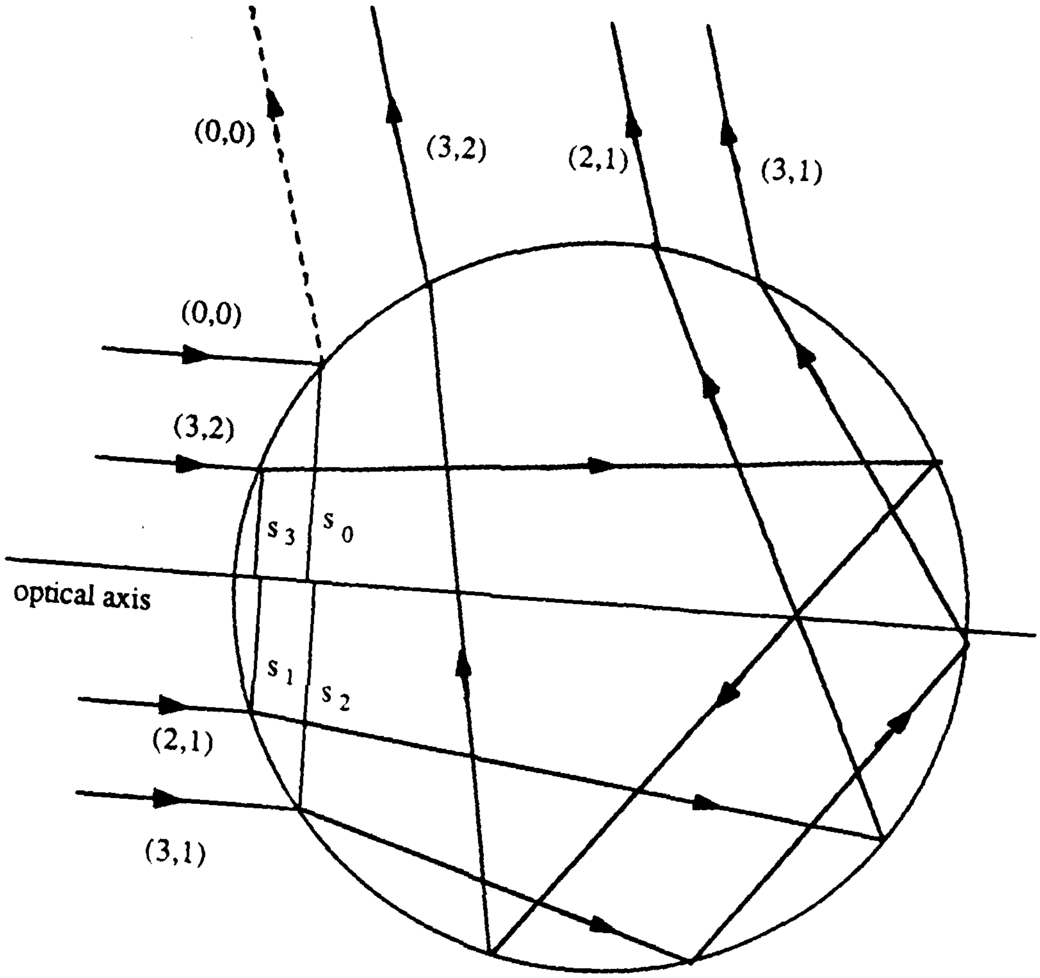

Figure 2: Ray diagram for Brewster angle light scattering

number of chords in the bubble, the second number tells how many times a ray crosses the optical axis.

2.3 Ray interference and Mie theory

Since we found several rays contributing to the scattering, we expect to see interference patterns in the Brewster angle region. To characterize the interference we use methods of geometrical optics and calculate the separation of adjacent extreme $\Delta\theta^{16}$.

$$\Delta\theta = \frac{\lambda_w}{d} \tag{11}$$

where λ_w is the wavelength of the incident light in water and d the distance at the bubble exit plane between two interfering rays. Looking at figure (2) we find by symmetry that the separation d of principal rays in the exit plane is given by the sum of their impact parameters s_0 and s_1

$$d = s_0 + s_1 \tag{12}$$

Therefore we get the final result as[1,4]

$$\Delta\theta = \frac{\lambda_w}{s_0+s_1} \tag{13}$$

Note that the greater d is, the smaller $\Delta\theta$ becomes. This means high frequency oscillations are caused by widely spaced rays.

The complete general solution for a plane wave scattered of a dielectric sphere was given by G. Mie in 1908[20]. But only recently with the advent of computers it was possible to calculate fairly easily scattered intensities over a range of angles for bubble sizes much larger than the wavelength of the used light . Figure (3) shows the Mie computation result for a bubble of typical size in this experiment. The bubble is characterized by the size parameter ka, where a is the bubble radius and $k=2\pi/\lambda_w$. All intensities in the Mie

Figure 3: Mie theory result, bubble size ka = 1000, a = 61.4 μm

Figure 3

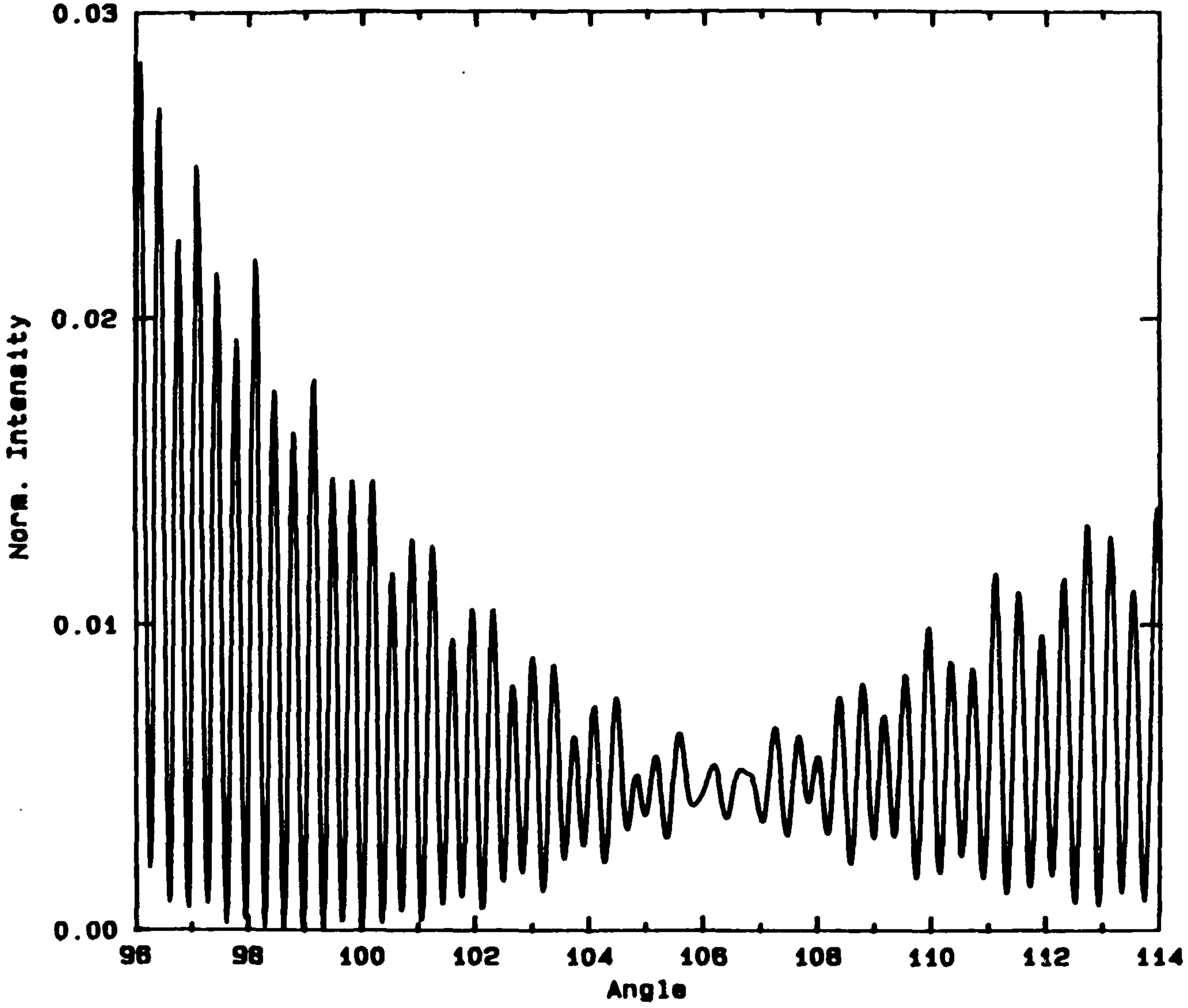
Norm. Intensity
0.03
0.02
0.01
0.00
96
98
100
102
104
106
108
110
112
114
Angle

calculations are normalized with respect to a perfectly reflecting sphere of the same size. For the computations the original MIEV0 code by W.J. Wiscombe[18] modified by S.C.Billette[9] and C.E.Dean[7] was taken. We clearly see the expected interference pattern and also a broad local minimum in intensity. A similar result is expected to be obtained in the experiment.

To describe the origin of the scattering pattern around Brewster's angle caused by interference, we now calculate d/a for Brewster angle scattering using equations 10,12. Since this quantity is proportional to $\Delta\theta$ we are able to get first information on what frequencies to expect. The result of d/a calculated for all theoretical possible interferences is shown in table 3. We notice that d/a is approximately the same for (0,0),(2,1) and (3,1),(3,2) interference. Therefore we do not expect to see a separate (3,1),(3,2) interference. A similar situation occurs between the (0,0),(3,2) and (2,1),(3,1) interferences. Hence a distinct (2,1),(3,1) frequency might also be hard to observe.

Besides this observation we also have to consider the amplitude of the contributing rays in the far field in order to make quantitative predictions about which interference patterns we expect to see. Concerning the amplitude in the far field, several considerations have to be made[11]. In our case we choose to pay attention only to one very important fact: how many interfaces each light ray hits. Every time light hits an interface, the intensity of the remaining light will be reduced because both, reflection and transmission occur. Therefore (0,0) and (2,1) are ordinarily dominant rays. Since they are widely spaced they cause the easy to detect high frequency (closely spaced) oscillations[1,4]. Around 106° the (0,0) ray goes through a local minimum in intensity. At Brewster's angle all parallel polarized light is transmitted into the bubble, none reflected. Because of that the scattered intensity also goes through a local minimum and the high frequency oscillation vanishes and then reappears. The remaining structure around 106° is caused by other interferences than those involving the (0,0) ray. The fringes around 106° are due to (2,1),(3,1) or (2,1),(3,2) interferences.

interference between		d/a = sin i + sin j
(0,0)	(2,1)	0.965300146
(0,0)	(3,1)	1.213676858
(0,0)	(3,2)	0.300773020
(2,1)	(3,1)	0.248376712
(2,1)	(3,2)	0.664527126
(3,1)	(3,2)	0.912903839

Table 3: d/a for all possible interferences with $p \leq 3$
i angle of incidence for the first ray
j angle of incidence for the second ray
$i \neq j$

Furthermore we notice a lower frequency modulation outside the Brewster angle scattering region. Because of the low frequency it is most likely caused by (0,0),(3,2) interference, since these rays are closely spaced.

The experimental goal is to find some of these effects for air bubbles rising freely through clean water:

i) the disappearance of the fringe pattern
ii) a broad local minimum in scattered intensity
iii) expected interference patterns.

Chapter 3

Experiment

3.1 Experimental set up

The basic set up which was used throughout the experiment is shown in figure 4. The light was provided by a Spectra Physics argon ion laser operating at 514.5 nm in air with a gaussian beam of 1.25 mm diameter at the $1/e^2$ point. A high quality ellipsometer grade polarizer was used to get a very accurate polarization because Brewster's angle occurs only for parallel polarized light as shown earlier. The next component in the light path was an aperture. It served to clean the laser beam, i.e. blocking out reflections from previous devices in the beam and eliminating low frequency modulations. Behind the aperture is the scattering chamber. It was specially built for this experiment and has some specifications that are worth mentioning. The following description of the chamber refers to figures 5 - 6.

The scattering chamber is built out of aluminum. It has three windows, an entrance window, an exit window, and an observation window. Through the entrance window at the front side of the chamber the laser beam enters the chamber. It is oriented so that the

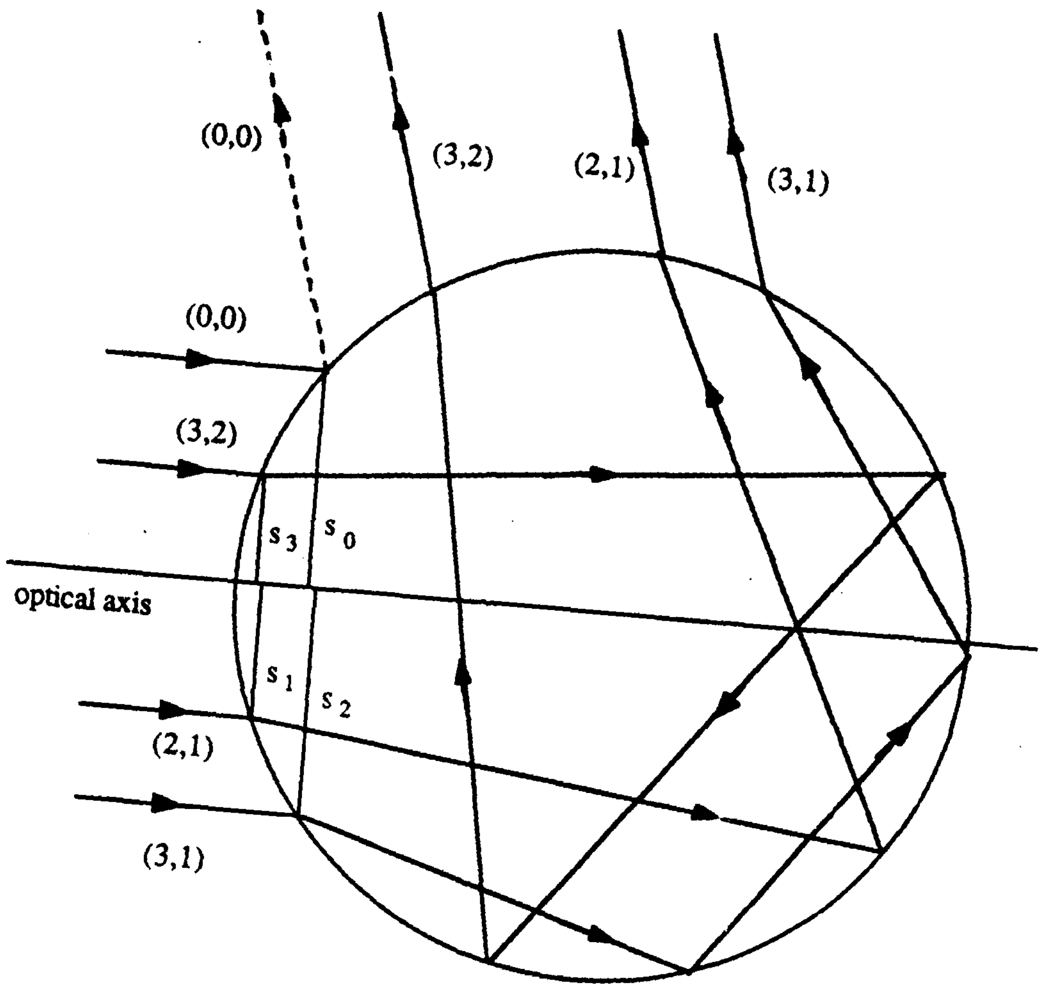

Figure 2: Ray diagram for Brewster angle light scattering

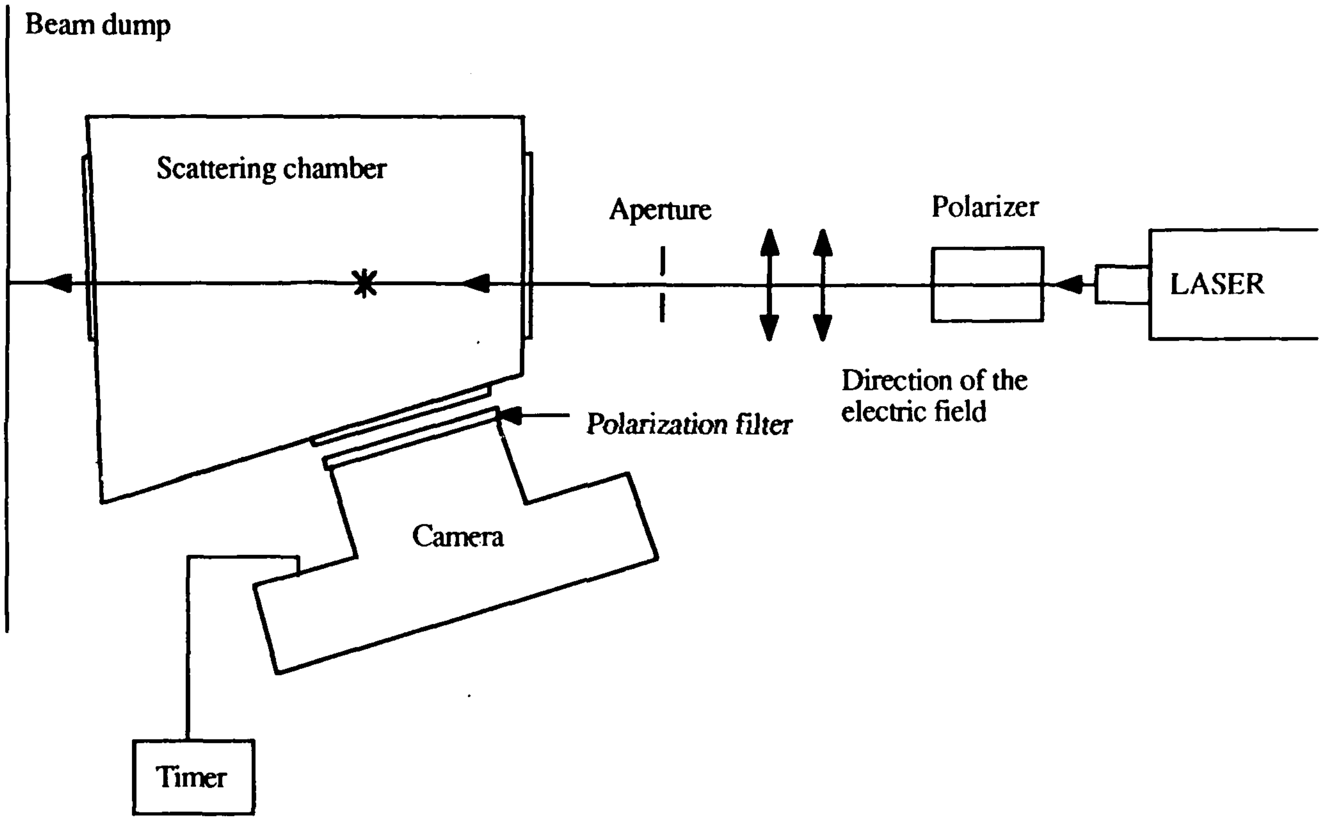

Figure 4: Experimental setup

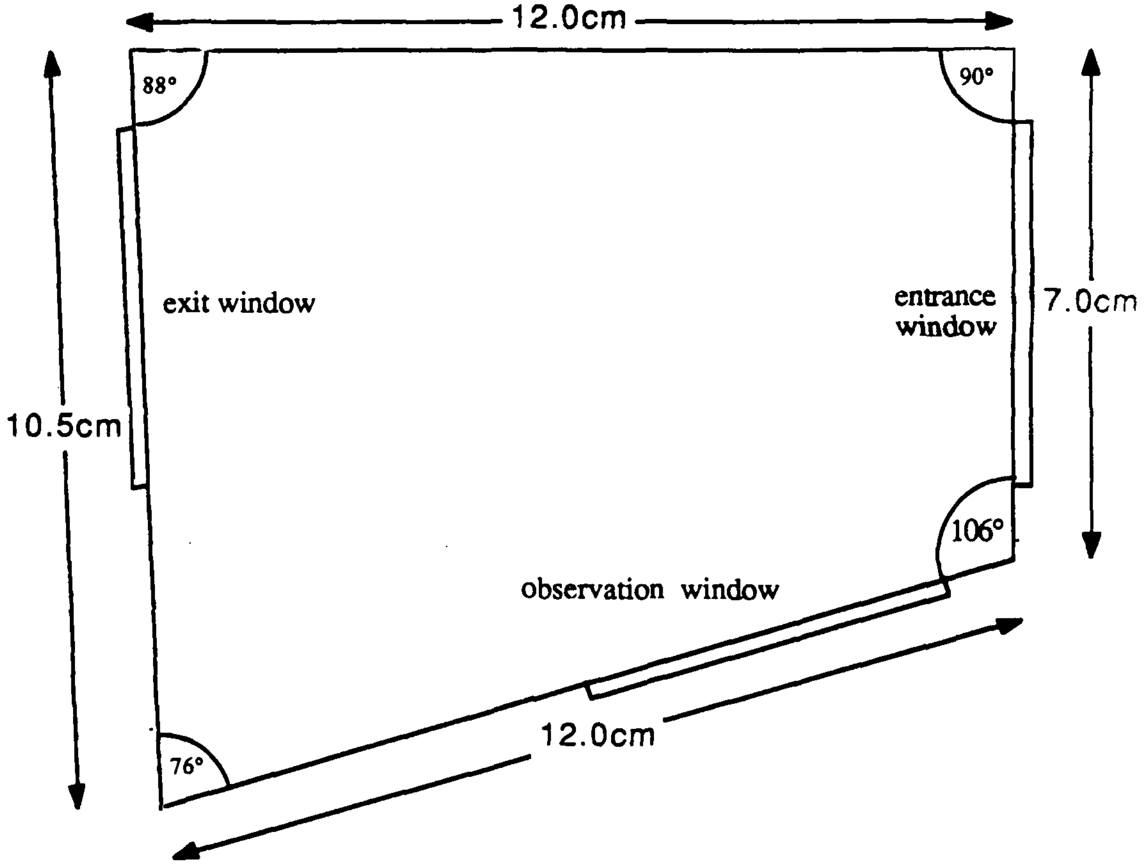

Figure 5: Scattering chamber, top view

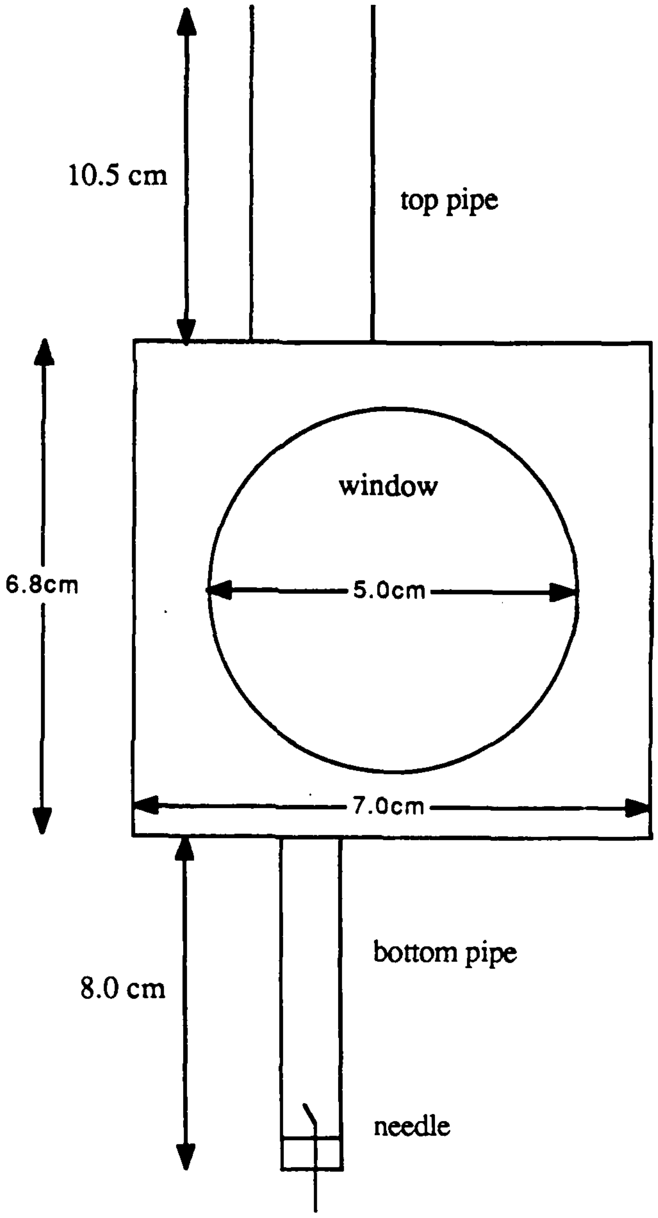

Figure 6: Scattering chamber, front view

incident light is perpendicular to the window in order to minimize refraction. The exit window at the back of the chamber is tilted 2° with respect to the entrance window. The reason for this is to avoid illumination of the bubble by the reflection from the rear window. Consider the case of parallel entrance and exit windows. We can calculate the scattering angle of the reflected light with the bubble. This gives the following result for the new scattering angle θ_S'

$$\theta_S' = 180^\circ - \theta_B = 180^\circ - 106^\circ = 74^\circ$$

This new angle θ_S' is very close to the region of critical angle scattering[3]. Although the laser beam is only partially reflected from the exit window, the effect of critical angle scattering from the reflected beam is still a lot stronger than Brewster angle scattering from the original beam in that region. So all one would see, provided parallel entrance and exit windows, would be the scattering pattern due to critical angle scattering which would completely dominate the Brewster angle effect. (A critical angle scattering pattern was actually observed with a preliminary version of the apparatus in which the exit window was not tilted.) Therefore the rear window was tilted so that the reflected beam goes off in a different direction and misses the bubble. Finally we have the observation window at one side of chamber. This window is oriented so that it is perpendicular to the scattered light coming of at 106°, the calculated Brewster scattering angle. All windows were high quality optical windows. The entrance and observation window had antireflection coatings on the outside. That helped to reduce unwanted reflected light off the windows. The whole body of the chamber, inside and outside, was anodized black in order to minimize reflections of the walls. At the bottom of the chamber a small pipe is mounted. At the bottom of this pipe a hollow needle is placed which is connected to an air supply. By regulating the air through the needle bubbles were created. While rising through this small pipe the bubble stabilizes, since almost all of the internal size oscillations damp out in a few parts of a second. On top of the chamber body, concentric with the bottom pipe, there is another pipe, larger in diameter. This pipe provides time to prepare for capturing and measuring the bubble, since it takes a couple of seconds for the bubble to rise to the top of that pipe after the scattering event.

The last component used in the experiment was a camera for recording the scattering event. It was mounted in front of the observation window. In order to reduce background scattering from the water and from the various interfaces, a polarization filter was placed in front of the camera lens. The polarization filter was set to pass light polarized parallel to the scattering plane.

Because the effect we are looking for occurs only at a specific angle, it is essential that all components remain in the same position relative to each other. To make sure of that all components were clamped to a rigid reference frame.

Doing the actual experiment consists of three parts:

i) angle calibration

ii) background determination

iii) data taking

3.2 Angle calibration

The first step in each run of the experiment is angle calibration, since the effect we are looking for occurs only at a specific angle.Therefore we need to identify angles precisely on the recorded scattering pattern. In order to get such a precise calibration, we had to add a couple of components to the basic set up (figure 7). First of all we need a reference direction. For this the back scattering direction was taken. To find the exact back scattering direction a beamsplitter was inserted in the light path. Then a retroreflector was placed behind the beamsplitter. The beam coming out of the retroreflector is reflected at 45° off the beamsplitter and then focused to a point. This point now defines the backwards direction.

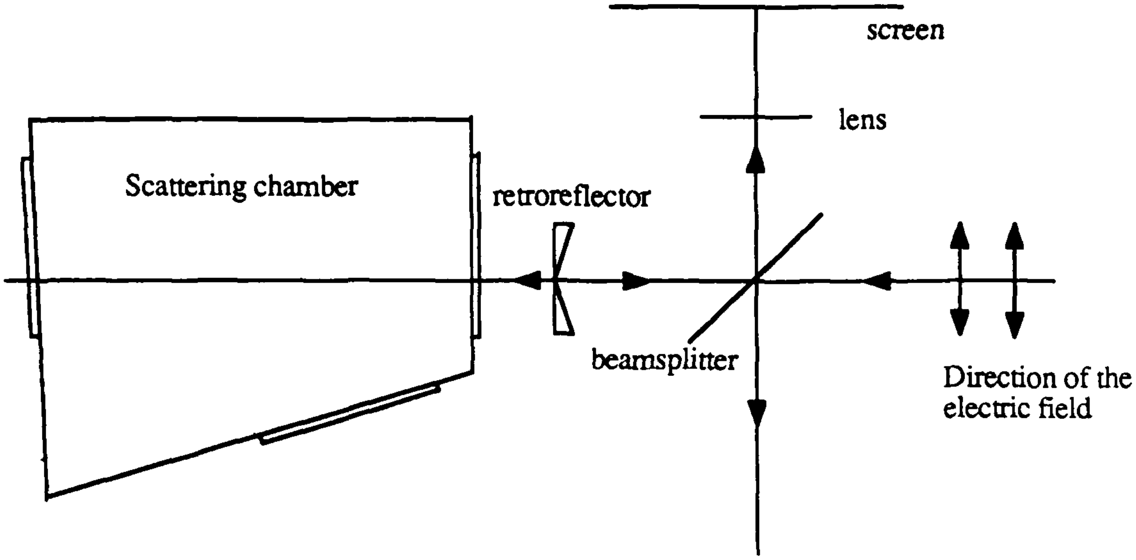

Figure 7: Angle calibration, experimental setup

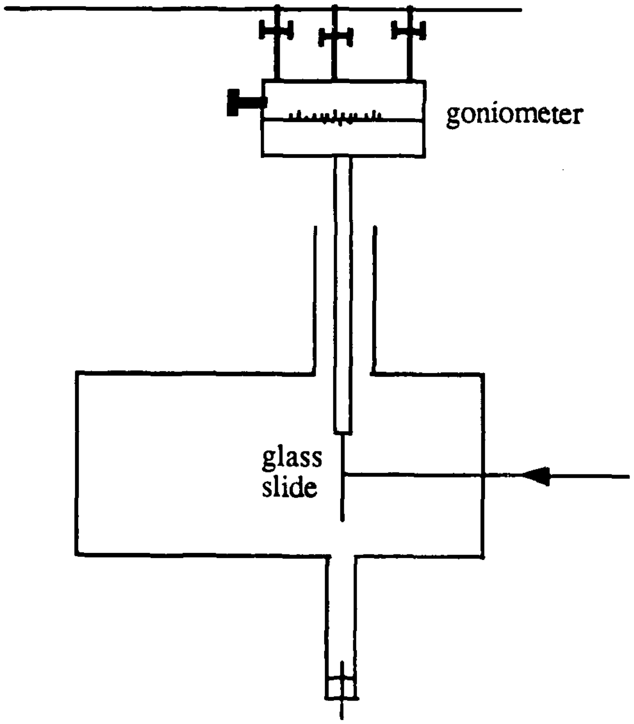

Figure 8: Angle calibration, view of the chamber

In the next step a thin glass slide, serving as a simple beam splitter, is placed in the scattering chamber (figure 8). The glass slide is mounted to the end of a rod which is connected to a goniometer. By rotating the glass slide to known amounts indicated by the goniometer, the incident light beam can be reflected in all wanted directions. But before applying this technique for angle calibration, the goniometer had to be calibrated. We rotate the glass slide so that the reflected ray of the glass slide is focused into the point defined earlier by the retroreflector. The reading the goniometer shows, now defines the reference backwards direction on the goniometer.

Finally the calibrated goniometer was used to mark reference points of exactly known angle on photographic film. The 106° scattering angle direction was dialed on the goniometer. Several dots around 106° are marked on one multiple exposed frame of the film. For each dot, the exact angle is known. Typically about six calibration points were taken. With this information we were able to tell the scattering angle of every point on the data negatives. This was done by using a linear extrapolation to determine the angle for each point on the picture. One edge of the negative always served as initial reference for applying the angle extrapolation to different negatives.

The whole angle calibration procedure is similar to that introduced by Langley and Marston[4]. It also automatically accounts for the effects of refraction at the water - window - air interface.

3.3 Background determination

Besides the desired scattering from the bubble, there is always unwanted background scattering which is also recorded on the film. In order to compare the data with theoretical results, we have to determine the background and subtract it out of the recorded data. A picture without bubble in the beam was taken. This represents all the background scattering that is present. Since the background is not a function of time, one background picture on each roll of film can represent the background for all data in that particular run of the experiment. Such a negative was analyzed and a background function was found as discussed in detail in a later section.

3.4 Data taking

The actual process of taking data is a fairly simple one. An air bubble is created with the needle at the bottom of the lower pipe. Then the bubble is watched rising freely through the water. When it is about to enter the light beam, the camera is triggered by hand. The shutter was closed as soon as the bubble left the beam again. The exposure time was measured with a simple clock triggered through the camera. After that, the bubble was captured under a glass slide, which was put on top of the upper pipe. While sitting under the glass slide the diameter of each bubble was measured using a measuring microscope.

During the whole process the camera was focused on infinity so that the Fraunhofer far field approximation yields. In different experiments a Nikon 85 mm lens and a Nikon 135 mm lens together with a Nikon F2 camera were used. For photographic film, Kodak Tri X pan 400 ASA was used. The laser delivered typically 300 mW power output. Throughout the experiment distiled water was used to reduce the amount of impurities which would otherwise tend to coat the bubble[7,9]. Furthermore distilled water helps reducing background scattering from small particles as well as getting as close as possible to the assumed refractive index[12].

Chapter 4

Results

4.1 Photographic data

In figure 9 a typical photograph of a scattering event is shown. We are able to recognize the high frequency oscillation in intensity resulting from the predicted interference patterns. Furthermore a disappearing of the fine structure in the middle of the picture can be noticed. This is first experimental evidence of Brewster angle scattering. But in order to get more detailed information from the picture concerning the spacing of the fringes, relative intensities and angles, the data from the photographic negatives have to be processed.

4.2 Data processing

After developing the film a digital intensity profile was taken with a microdensitometer. To get good results, the following procedure was applied. Five scanlines in horizontal direction in the middle of the negative were taken. The scanlines were 0.2 mm apart from each other. The scanning was done with the scanning optics defocused. The reason for that is that the microdensitometer resolves structures at about the grain size of the negative. If a negative is scanned somewhat out of focus, optical averaging in the horizontal direction is done. This is done to reduce grain noise and emphasize the real structure of the data. Even when defocused, the resolution of the microdensitometer greatly exceeds the spacing of the fine fringes. Other sources of random noise are imperfections of negative and scanning optics and dust. These effects were reduced by taking the five scanlines and by forming mathematical average. Usually 760 data points were taken across the negative. Considering around 600 data points in a relevant angle range of about 12°, we end up with a stepsize of

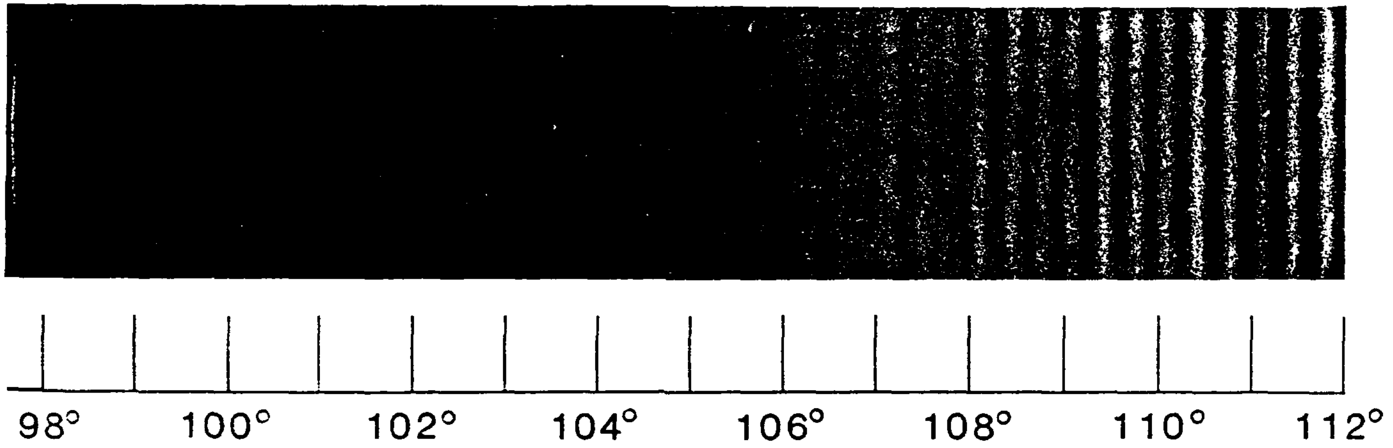

Figure 9: Photograph of a scattering pattern between 99° and 112° taken with the 85 mm lens.

around 0.02 degrees/data point. The exact stepsize depends on the camera lens which was used to record the specific negative.

Besides reducing the noise and bringing out the structure of the data as much as possible, there is another problem. In order to compare experimental data with theoretical calculations, we ideally would like to know absolute intensities for the recorded scattering pattern. The microdensitometer puts out only a relative intensity profile. Therefore we have to use an empirically obtained response curve of the photographic film. This curve is called the Hurter - Driffield (H&D) curve[14]. In this curve the logarithm of the exposure logE is plotted versus the photographic density D. The exposure is defined as

$$E = J\,T \qquad (14)$$

with J as the intensity incident during the exposure time T,

and the photographic density is determined by

$$D = \log\left(\frac{1}{\tau}\right) \qquad (15)$$

where $\tau = \frac{I_{trans}}{I_{in}}$ with I_{trans} being the local transmitted intensity through the negative and I_{in} being the local incident intensity from the densitometer.

A typical H&D curve is shown in figure 10. The interesting thing about that curve is the large linear region. If the film is used in this region the photographic density can be written as

$$D = \gamma \log E - D_0 \qquad (16)$$

where γ is the slope of the curve in the linear region and

D_0 is the intersection of the linear approximation with the D - axis.

If now the definition of the density D from equation (15) is inserted into equation (16), we are able to find an expression for the exposure and hence the intensity J in terms of know parameters.

$$\log E = -\frac{1}{\gamma}(\log\tau - D_0)$$

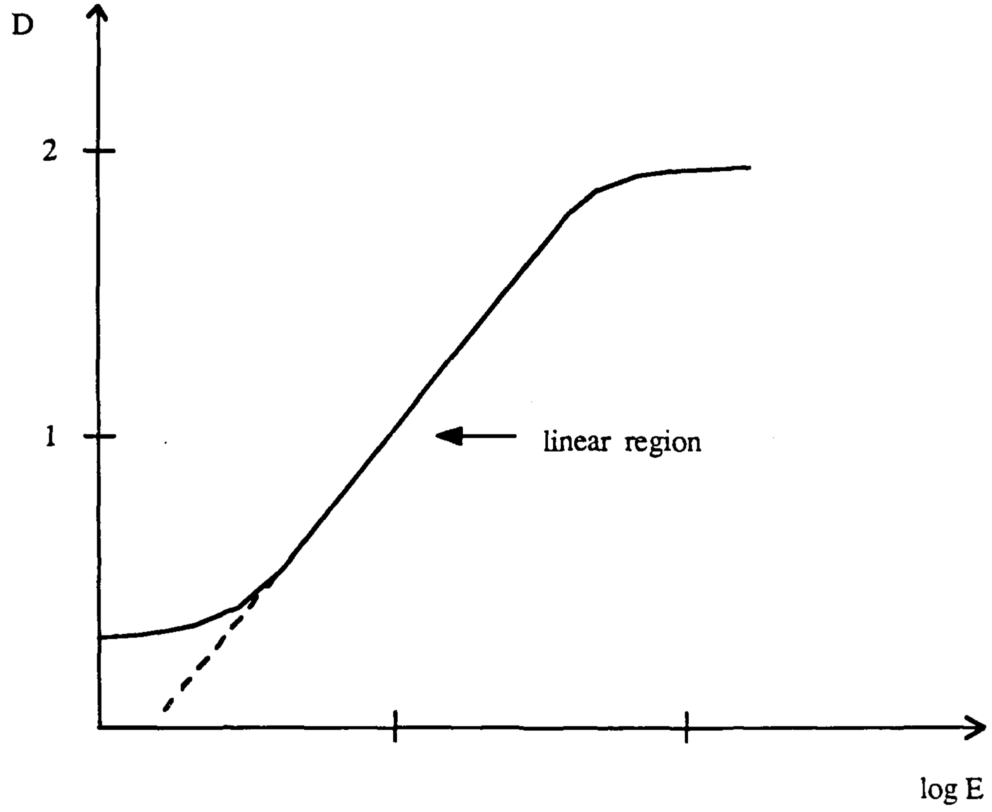

Figure 10: H & D CURVE

$$E = J\,T = \tau^{-(1/\gamma)}\,10^{(D_0/\gamma)} \qquad (17)$$

The exposure time T was measured for each picture. γ and D_0 were obtained through some calibration negatives. On each roll of film a couple of frames were exposed by uniformly spread laser light at various known exposure times. After scanning these negatives with the densitometer, each of the negatives represents one point on the actual H&D curve. Through these points a linear least square fit was made to get γ and D_0. This process was done for every roll of film, since γ and D_0 depend upon the developing process.

After converting the data negatives from relative densitometer intensities to real exposures and intensities, the angle calibration was applied to the data. Now a first look at the data could be taken (figure 11a). In order to check the quality of our results we have to compare them with valid models and theoretical calculations. Therefore we go back to Mie theory and plot a Mie calculation results for each bubble. For the calculations the directly measured radius of the bubble was used.

4.3 Averaging

By looking at figure 11a we notice that the data shows a lot more structure than the Mie calculation result (figure 12a). That suggests that the optical average was not enough and that there is still some noise in the data. Therefore we decided to do running averages in angle direction. First we took an algorithm that averages the two data points before and after with the data point of interest; this is called a "two point average". Then we did the same but only including one point before and after the data point of interest, a "one point average". The results are shown in figures 11b and 11c. We notice two effects of the average. First of all the data does not look so noisy anymore. It now looks more like the Mie calculation results in figure 12a. The second effect of the averaging is that the amplitude of the fringes is reduced. This would not be bad because we could compensate

Figure 11a: Intensity profile of experimental raw data obtained through a microdensitometer scan. (A scan of the same bubble shown in figure 9, ka = 1278, a = 78.5 μm.)

Figure 11b: Experimental data as in figure 11a, but two point averaged.

Figure 11c: Experimental data as in figure 11a, but one point averaged.

Figure 12a: Mie theory *result for the same bubble displayed in figure* 11a, ka = 1278, a = 78.5 μm, non averaged.

Figure 12b: Mie theory result as in figure 12a, but two point averaged.

Figure 12c: Mie theory result as in figure 12a, but one point averaged.

Figure 11a

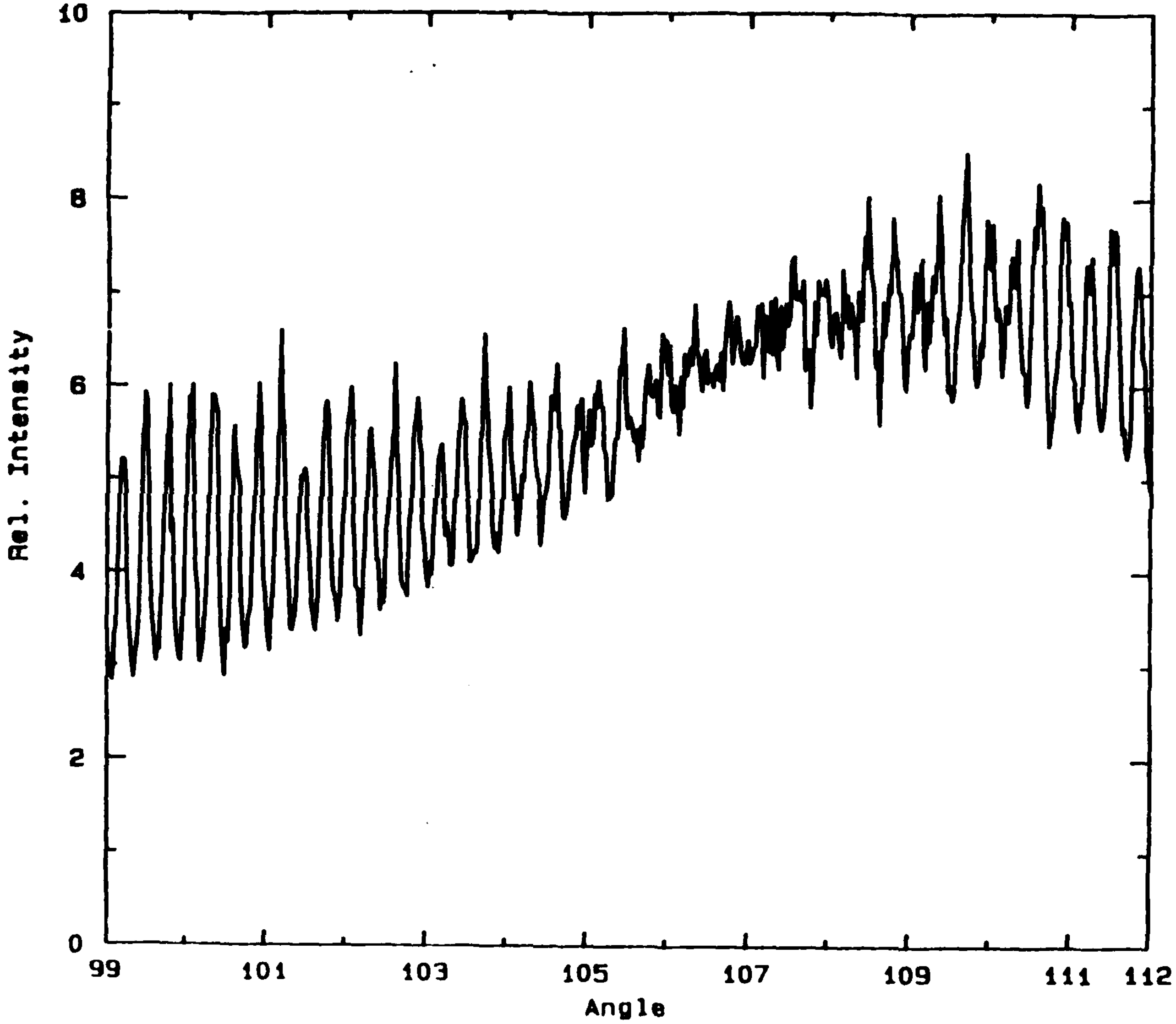

Figure 12a

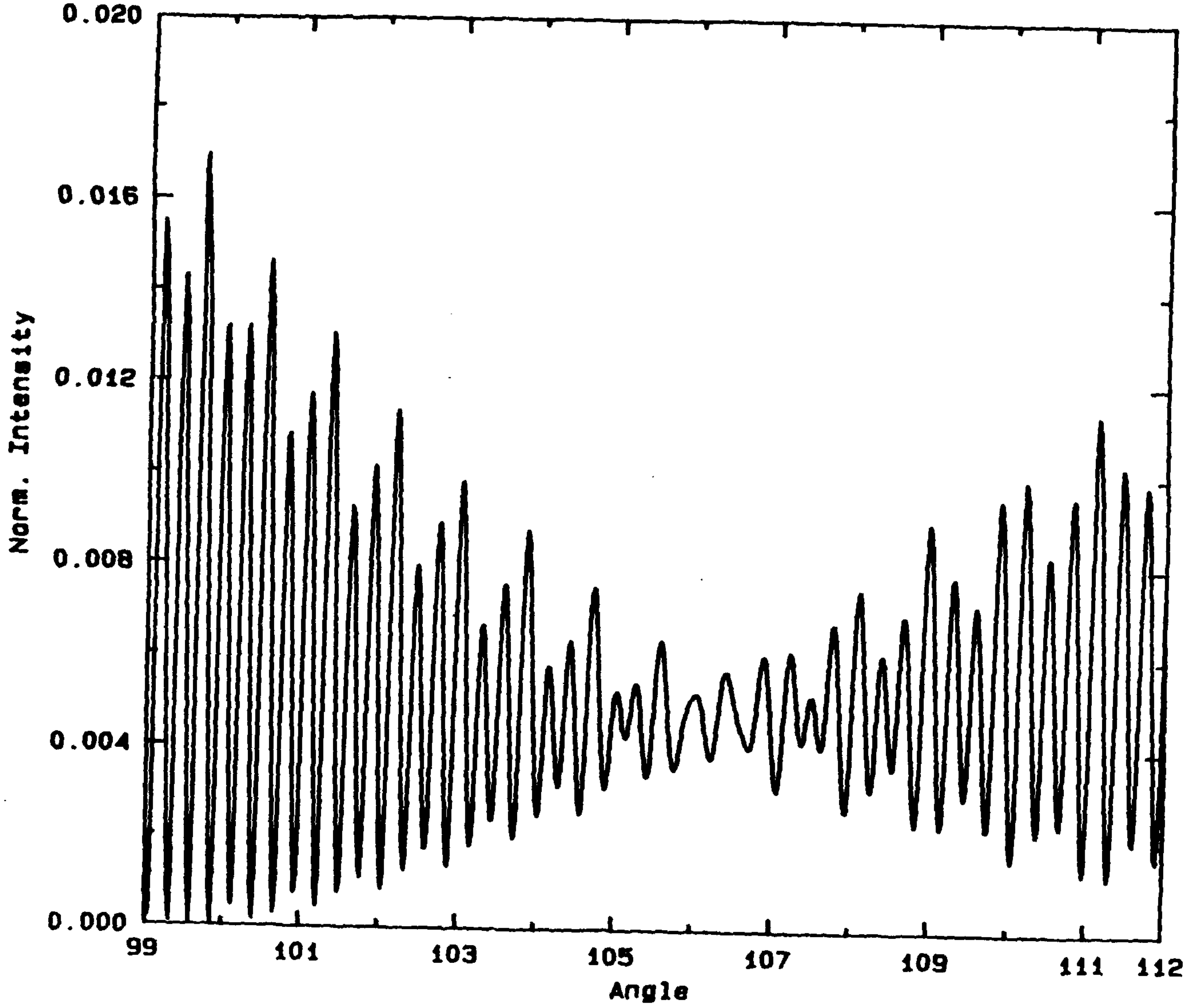
Norm. Intensity
0.020
0.016
0.012
0.008
0.004
0.000
99
101
103
105
107
109
111
112
Angle

Figure 11b

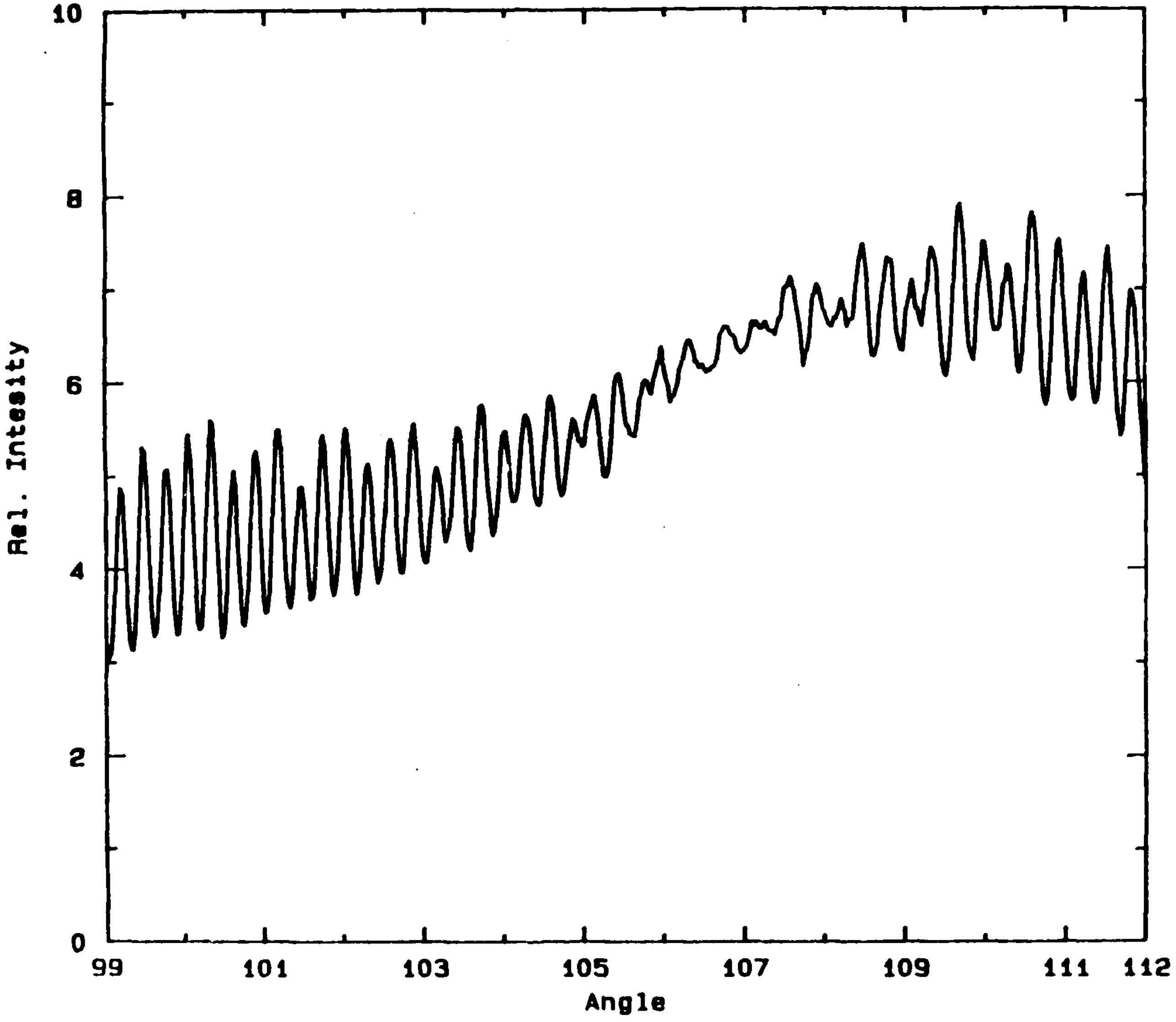

Figure 12b

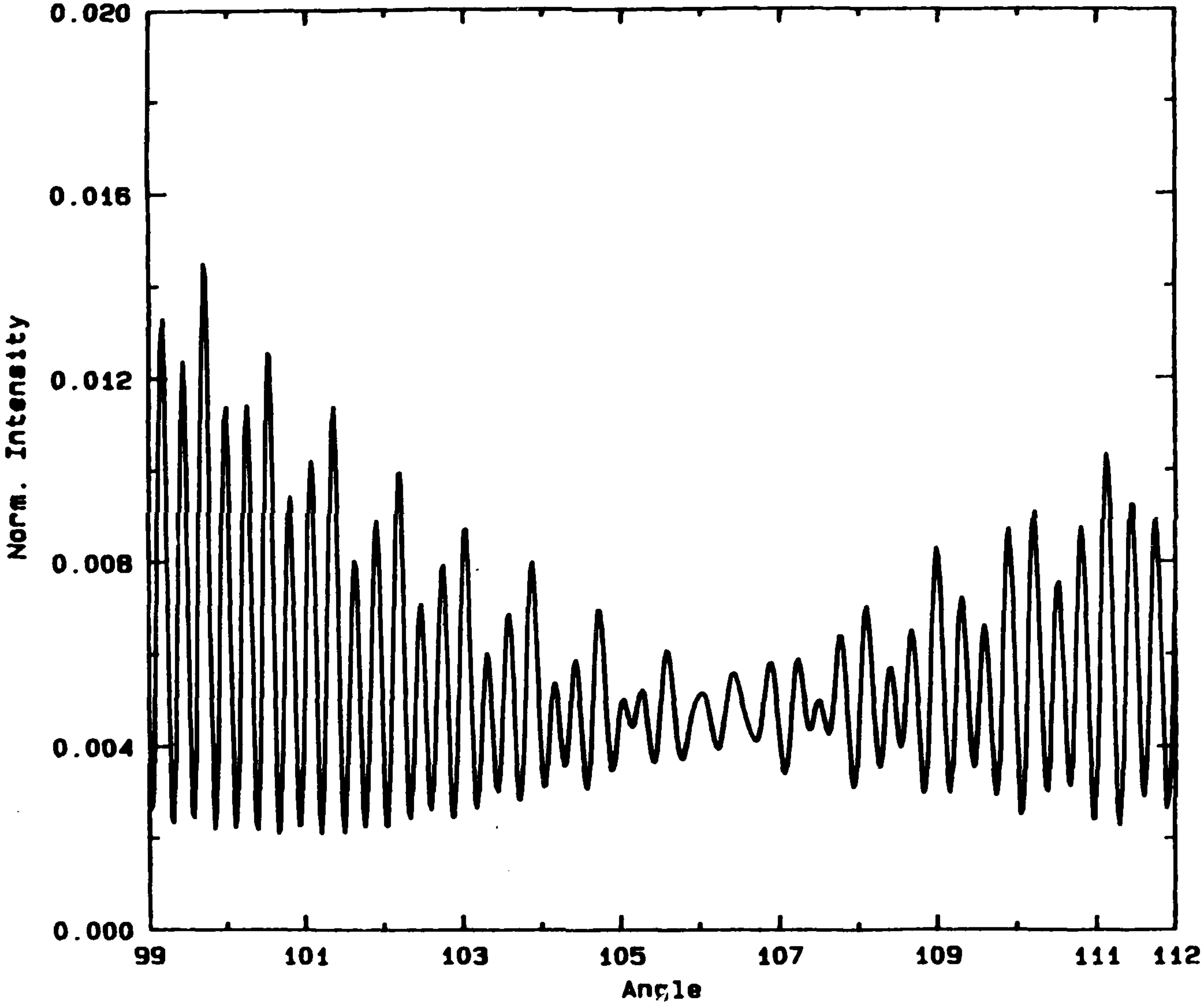
0.020
0.016
0.012
0.008
0.004
0.000
Norm. Intensity
99
101
103
105
107
109
111
112
Angle

Figure 11c

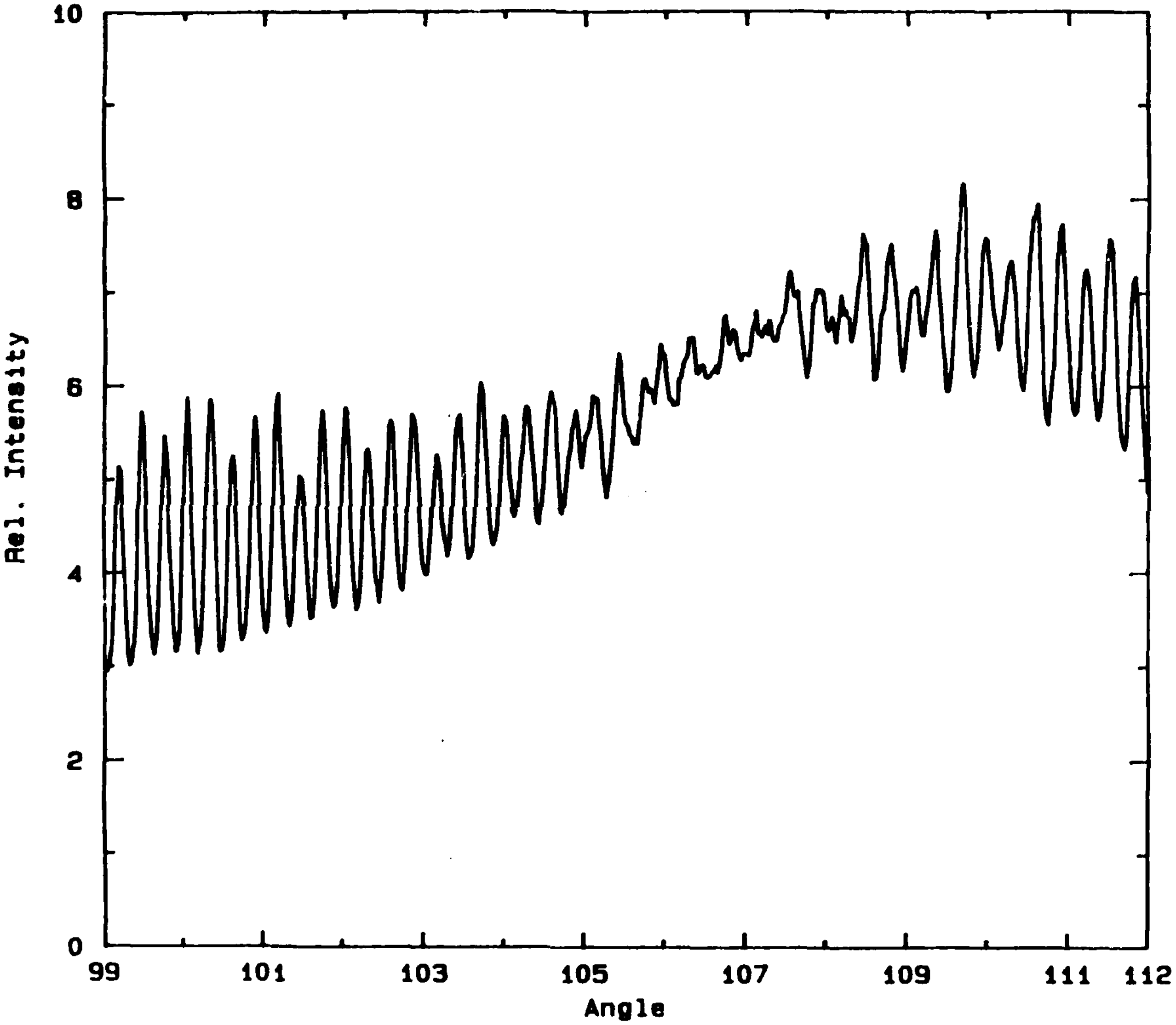

Figure 12c

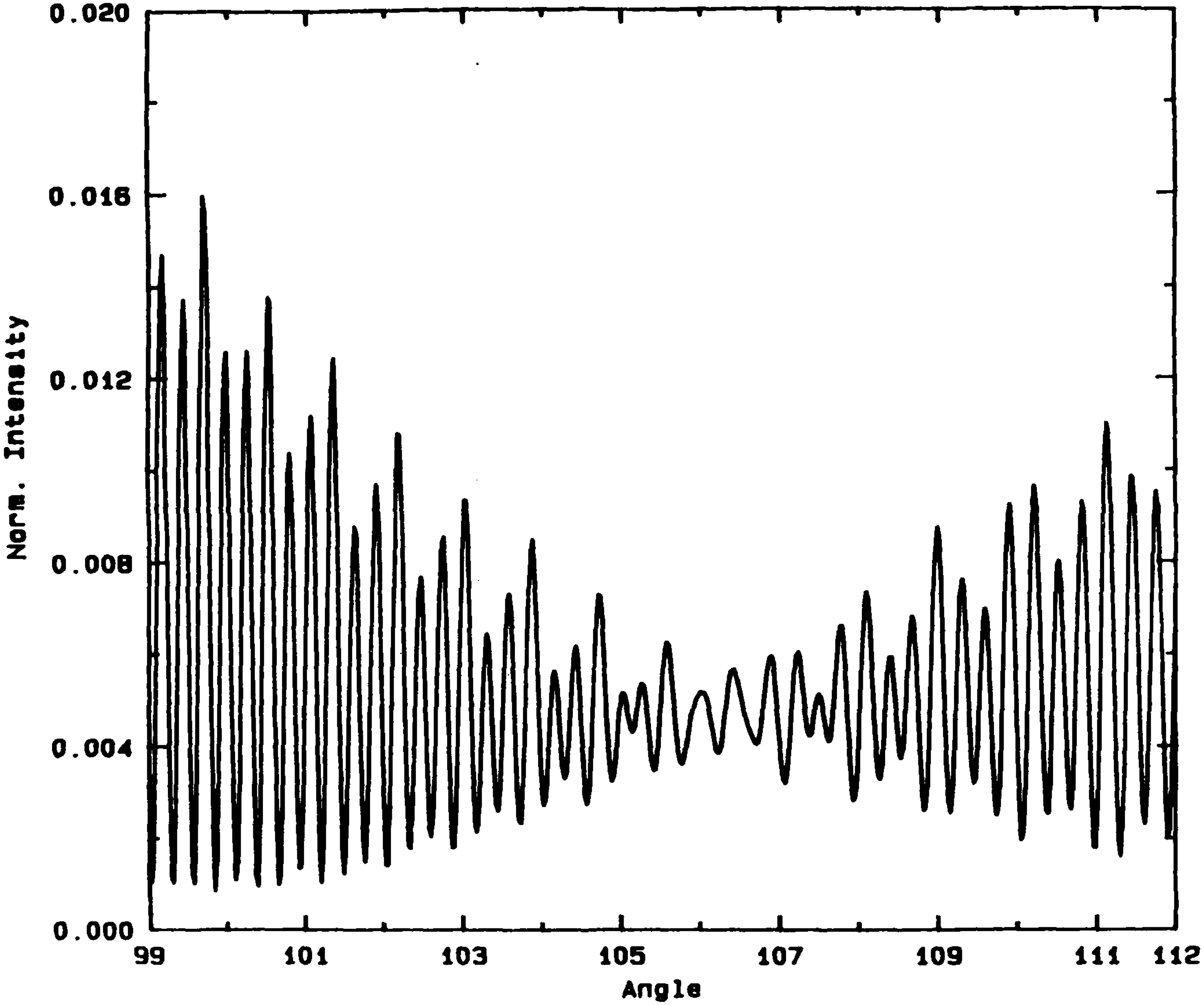
0.020
0.016
0.012
0.008
0.004
0.000
Norm. Intensity
99
101
103
105
107
109
111
112
Angle

for that with a scaling factor applied to the averaged data. But since the amplitude of the high frequency oscillation is much more affected by the averaging than the low frequency oscillations, we get a non uniform reduction of the amplitude. This makes it more difficult to compare experimental and theoretical results. Because of that we took the same averages of the Mie theory data (figure 12b and 12c). The difference between the two averaging procedures is the following. The two point average is more effective in reducing the noise, but it also reduces the high frequency amplitudes much more than the one point average. Because it is most important to analyze the structure of the data, we decided to go with the two point average for all other data shown in the appendix. The stepsize for computing Mie theory and averaged Mie theory was set to be the same as for the experimental data. Now we are able to compare experiment and theory. Doing so, we notice several things.

i) Theory and experiment agree in one very important feature, fringes caused by interference.

ii) The visibility of the fringe pattern is drastically reduced in the predicted region.

iii) The baseline structure of experimental data and Mie theory is different.

iv) The intensity scale of experiment and theory is different.

In the following section each of this points will be discussed and interpreted separately. Thereby we will follow one specific bubble through the whole process of analysis. The results for more cases are shown in the appendix.

Chapter 5

Interpretation and Discussion

5.1 Baseline structure and background

By comparing experimental data and theoretical results we see a huge difference between these two in their overall shape. While the baseline structure of the theoretical data appears to come to a broad local minimum around 106°, the shape of the experimental result is nothing like it. The reason for that is the following. The recorded intensity on the negative I_N is a composite of real scattered intensity from the bubble I_{data} and background $B(\theta)$.

$$I_N = B + I_{data} \tag{18}$$

Therefore we have to determine the background B *in order to interpret the data.* If we take a look at the background (figure 13), we notice that the background is a function of scattering angle. Since the scattering event takes place in water, a guess for one background component was dipole radiation of water.

When an electromagnetic wave goes through water, it forces the electrons of the water molecules to oscillate with the frequency of the light. Each water molecule then acts like a dipole, radiating in all directions (figure 14). Since the water molecules are randomly positioned, we get scattered light from the water. This phenomena is also known as Rayleigh scattering. The irradiated intensity I_D is a function of angle and can be written as[13,15]

$$I_D = A \cos^2\theta \tag{19}$$

By looking at the geometry of the problem we observe that we are just in the position to see some dipole scattering of water, varying with angle. If we try to fit the function given through equation 19 to the background with A as a free strength parameter proportional to

Figure 13: Intensity profile for a background picture

Figure 13

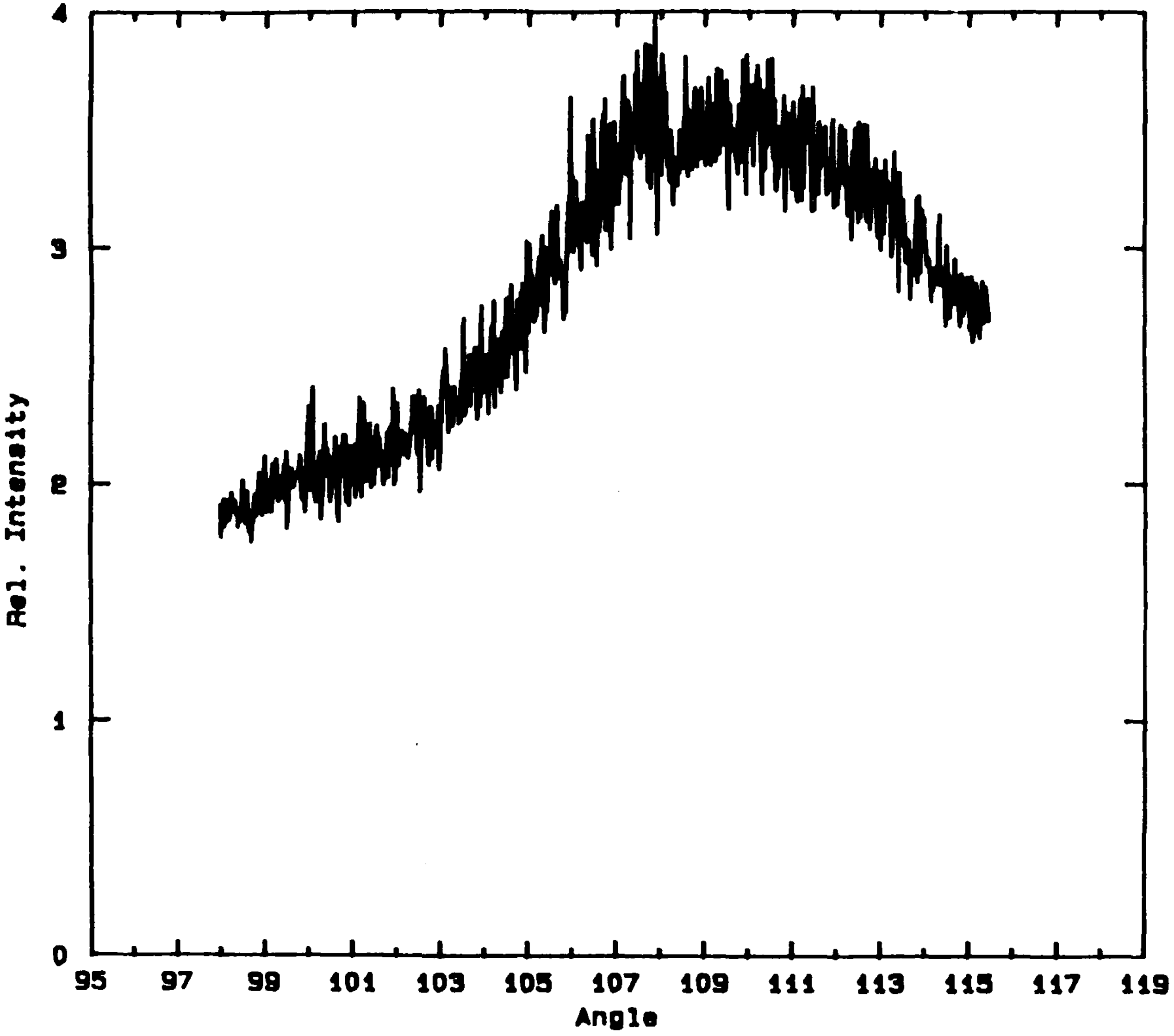
4
3
2
1
0
Rel. Intensity
95
97
99
101
103
105
107
109
111
113
115
117
119
Angle

Figure 14: Polar plot of $I_N = \cos^2\theta$
The scattered intensity I_N is displayed by the magnitude of the vector pointing from the origin to the arc starting at (1,0) for 0° scattering angle.

Figure 14

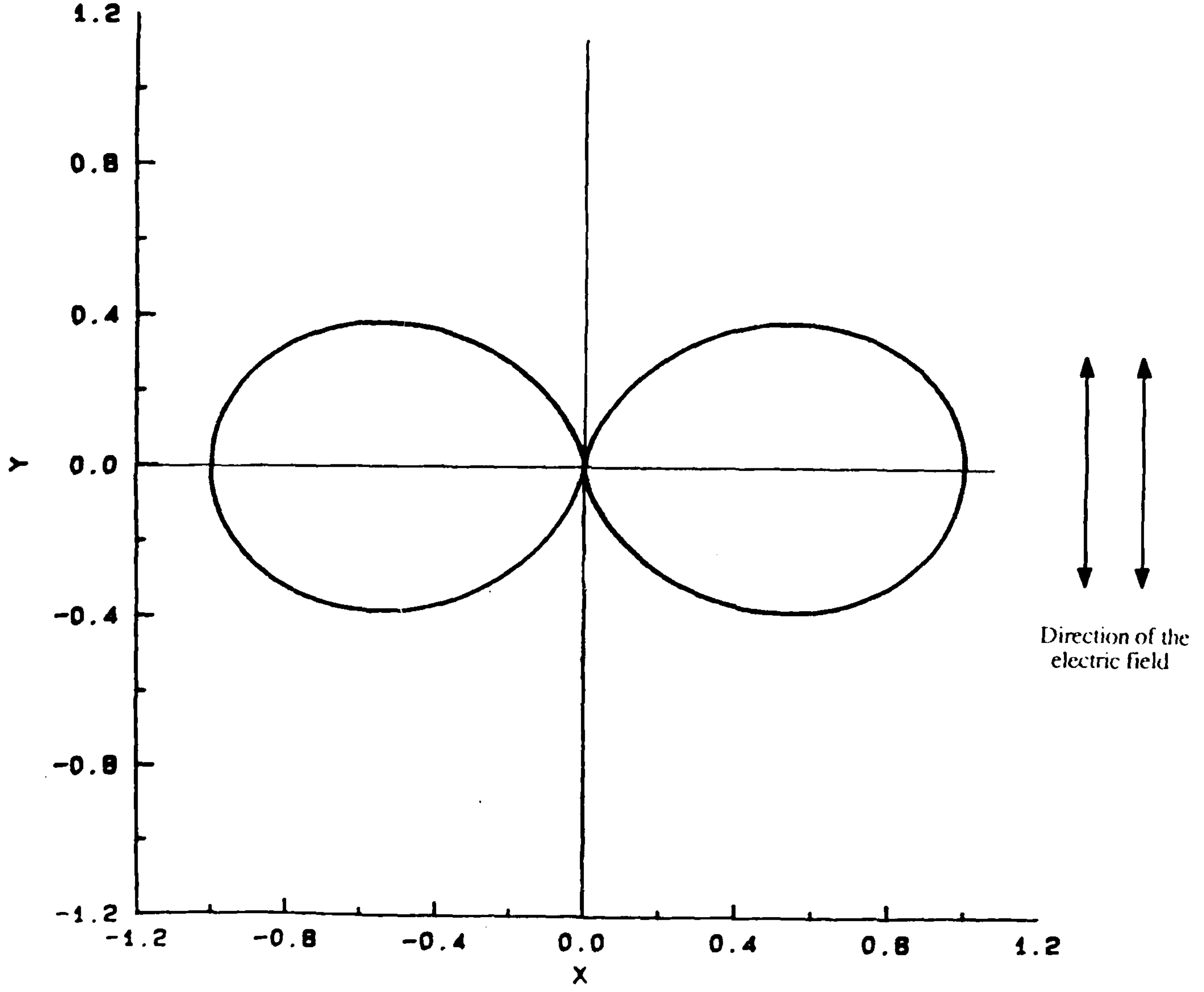
1.2
0.8
0.4
0.0
-0.4
-0.8
-1.2
Y
-1.2
-0.8
-0.4
0.0
0.4
0.8
1.2
X
Direction of the electric field

the exposure time, we find that only the middle part of the background fits well (figure 15). The other parts are different and because of that, it is not possible to use Rayleigh scattering from water to describe the detailed shape of the background function.

Therefore a different approach was taken. Instead of subtracting out the Rayleigh scattering of water, a fourth order polynomial was fitted to the background data in the range of the used data, e.g. 99° - 112° (figure 16).

$$f(\theta) = a + b\theta + c\theta^2 + d\theta^3 + e\theta^4 \qquad (20)$$

This procedure provides a better fit in the interesting region than fitting a function to the entire background data. It is valid to take only part of the background as long as it includes the range of angle seen in the data pictures.

After determining a background function this background function $f(\theta)$ was subtracted from the the recorded data I_N to obtain the actual data (figure 17).

$$I_{data} = I_N - \alpha f(\theta) \qquad (21)$$

where α was an adjustable free parameter. α was chosen such that the data showed about the same baseline structure as the Mie calculation results. One remaining problem however is intensity matching.

5.2 Intensity matching

The next step is to adopt the intensities of the background subtracted data to the normalized intensities of the Mie theory results. All intensities shown so far in figures of raw data and background subtracted data are basically in arbitrary units. However this does not diminish the quality of the data or its validity, since the important thing is the structure. We now want to make some comments about problems and possible errors in trying to find normalized intensities.

As described earlier the absolute intensities are obtained through the H&D curve. Using the H&D curve involves several premises.

Figure 15: The function $I_N = A \cos^2\vartheta$ fitted to the background.
Solid line: I_N; dotted line: background

Figure 16: Fourth order polynomial fitted to the background between 99° and 112°
Solid line: polynomial fit; dotted line: background

Figure 15

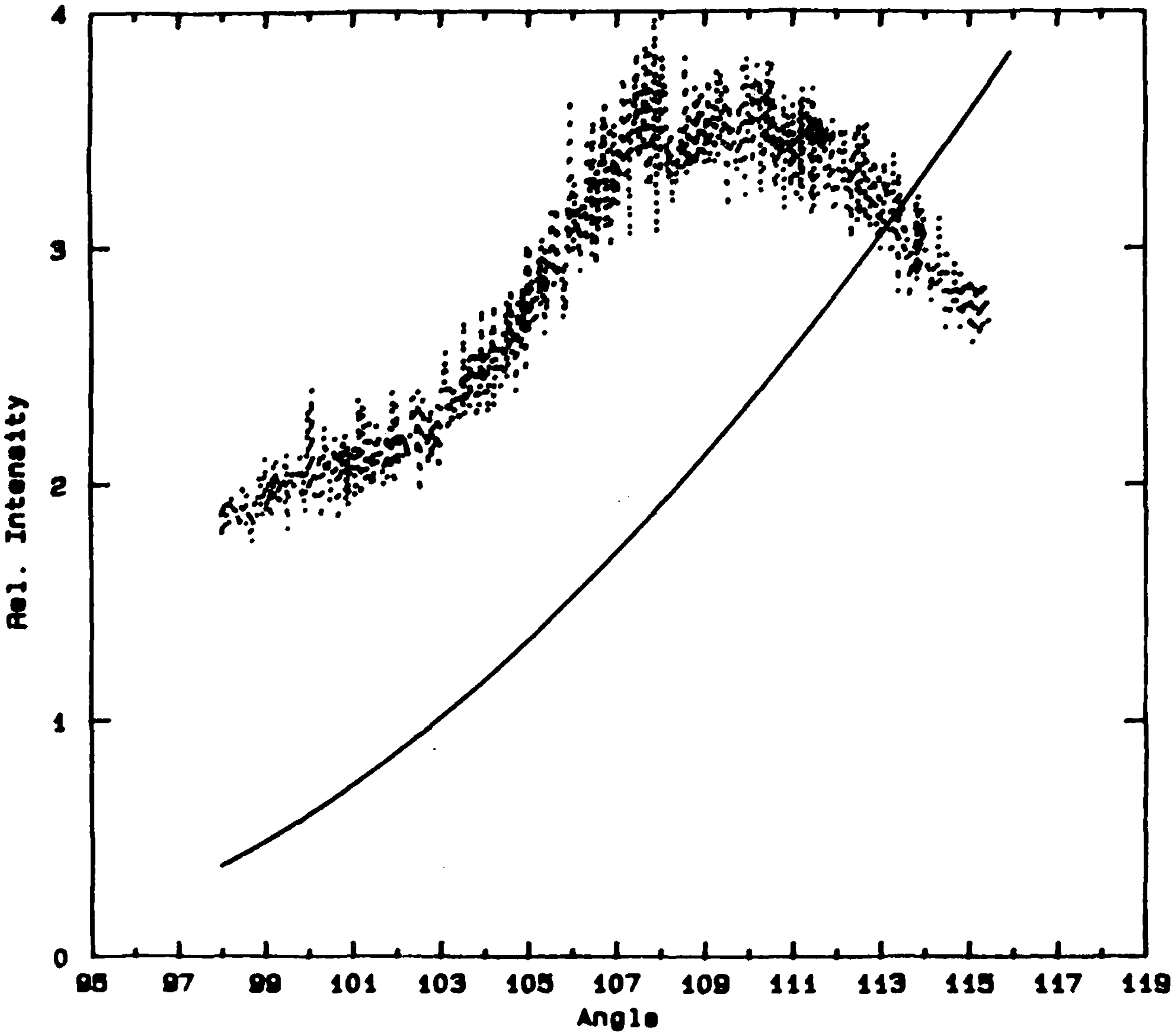
4
3
2
1
0
Rel. Intensity
95
97
99
101
103
105
107
109
111
113
115
117
119
Angle

Figure 16

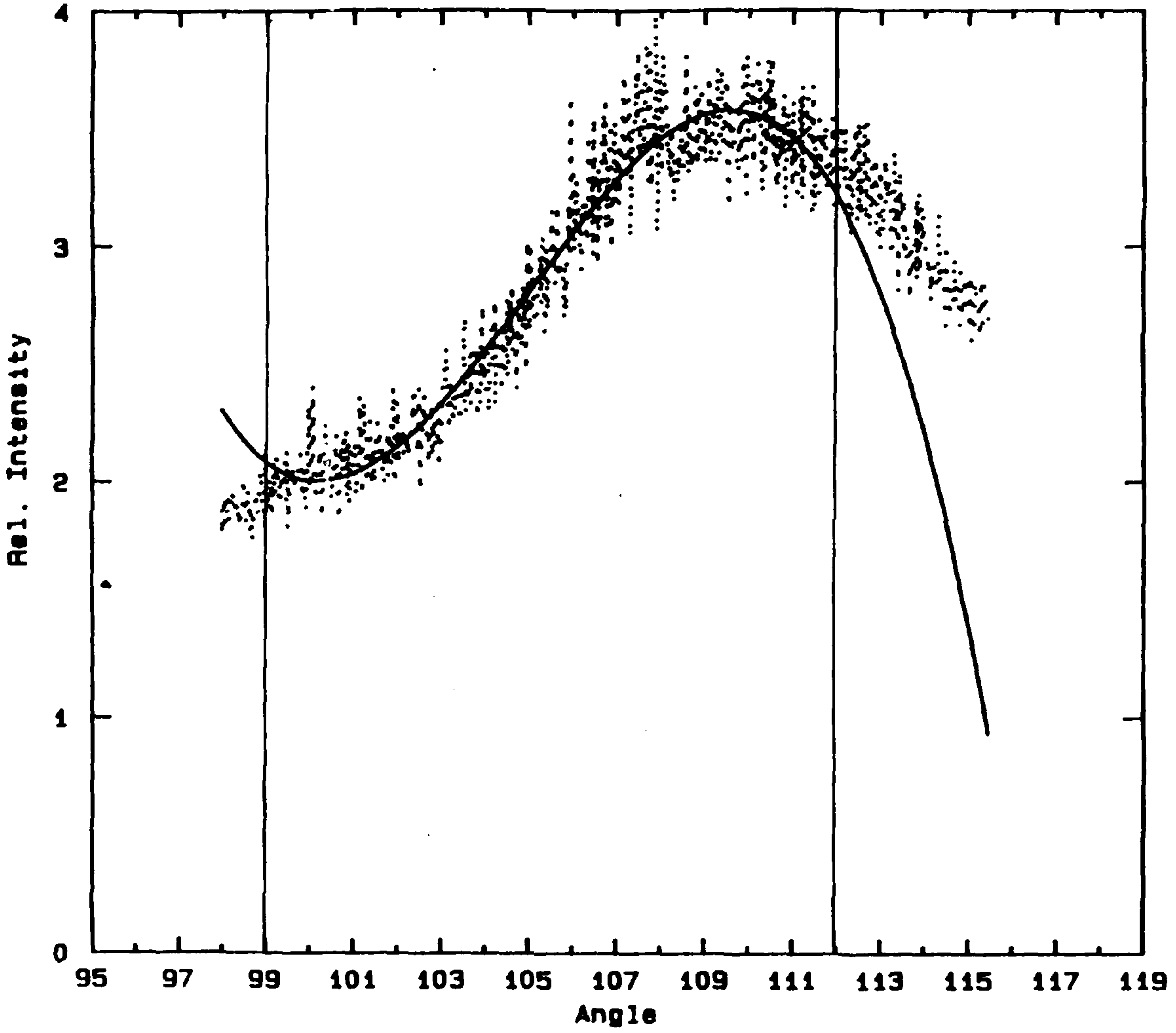
Rel. Intensity
0
1
2
3
4
95
97
99
101
103
105
107
109
111
113
115
117
119
Angle

BLANK

Figure 17a: Background subtracted, two point averaged, unscaled data,
ka = 1278, a = 78.5 μm

Figure 17b: Background subtracted data as in figure 17a, but one point averaged.

Figure 17a

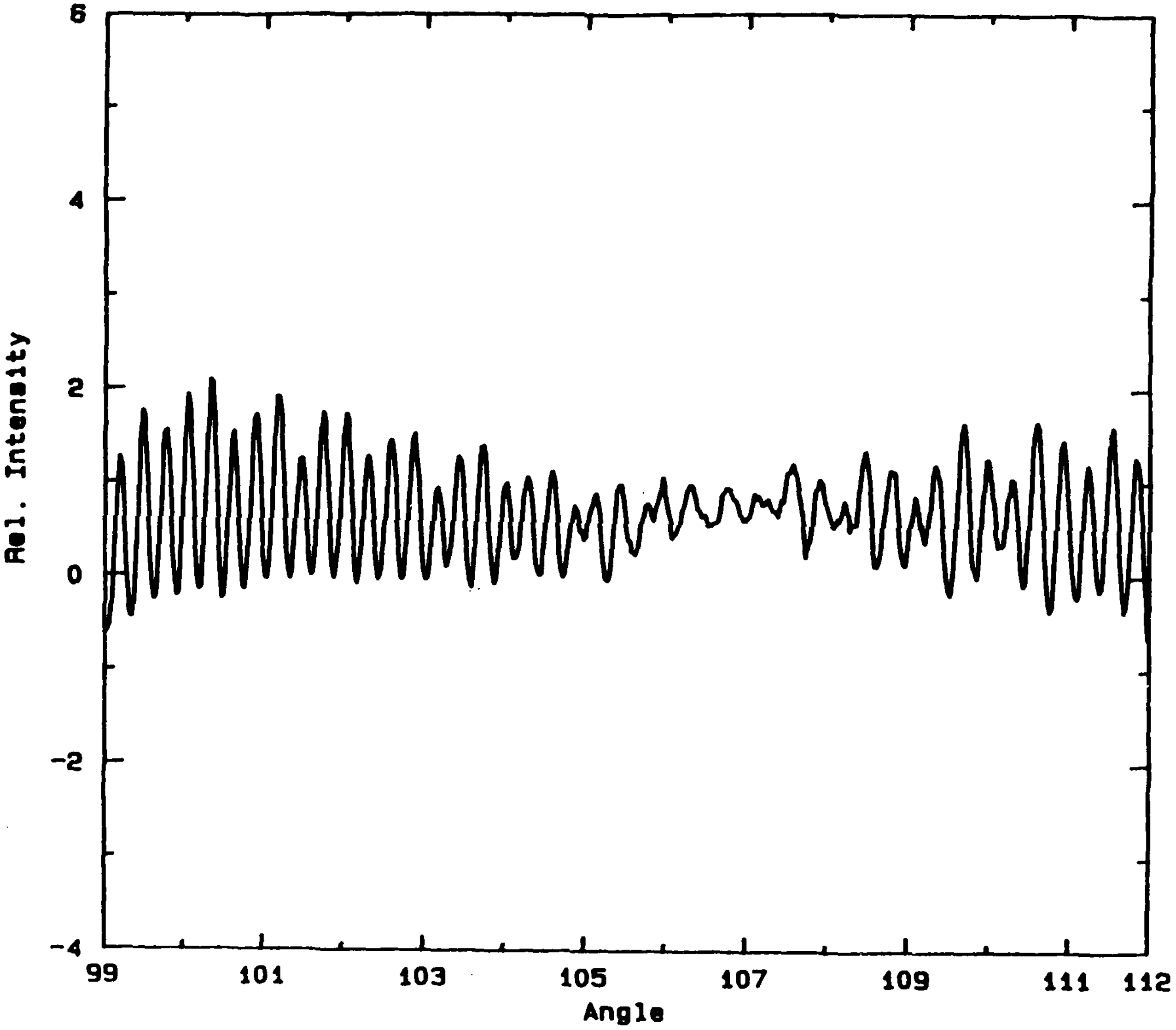

Figure 17b

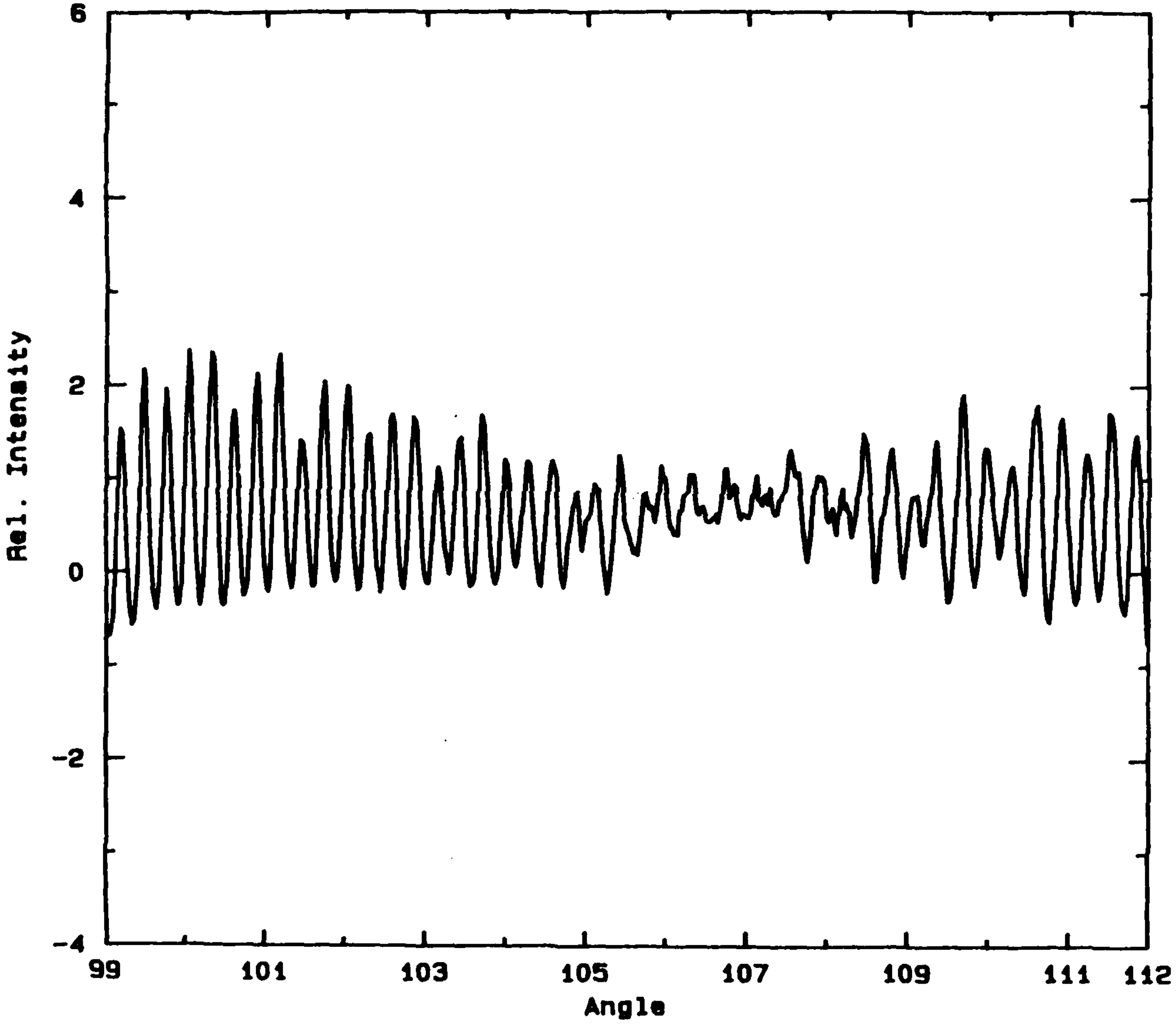

i) In producing the H&D curve uniformly spread laser light was used. To determine an absolute H&D curve, the absolute incident intensity onto the negative would have to be known (equation 14). However in this experiment this could not be directly measured. Therefore there is an undetermined scaling factor. This does affect the values for γ and D_0.

ii) It was assumed that the film was used in the linear region of the H&D curve. If however the incident intensity is very low (or very high) the actual H&D curve diverges from linear behavior (figure 10). Since the linear approach is used throughout all data, this might be a source of error especially for low intensities. Inspection of figure 10 suggests that one effect of nonlinearity of the H & D curve would be to offset the inferred intensities. In our final analysis we add a constant to the intensities in order to compensate for these and other effects. The value for this constant is taken to be a free parameter for each negative.

iii) Furthermore it was assumed that the densitometer reading is a linear function of the incident light provided by that device. However this may not be exactly the case. The output of the densitometer may be slightly nonlinear. However this behavior does not affect the general shape and structure.

iv) The air glass water interfaces at the entrance window and observation window were not accounted for. Although they are perpendicular to most of the light, they do introduce an error in obtaining intensities which might depend weakly on angle. The severity of the problem is reduced because of the antireflection coating on the outside of the observation window. The coating reduces the strength of internal reflections slightly. Additional experiments on scattering from a reflecting cylindrical wire suggest that the transmittance through the observation window depends very weakly on angle.

Therefore, the following procedure to match experimental and theoretical intensities was applied. Since all theoretical results are normalized to the irradiance of a perfectly reflecting sphere of the same size as the bubble, the experimental data were multiplied by a scaling factor β such that the distance between minima and maxima of fringes at a given angle were the same as for the Mie theory result of that particular bubble. Then a constant c was subtracted to lower the whole spectrum to the desired level defined by the Brewster angle scattering region. Both constants, for multiplication and subtraction, were necessary because of the above described implications in obtaining absolute intensities.

$$I_{Norm} = \beta\, I_{data} - c \qquad (22)$$

The final result is shown in figure 18. These results are now taken into further investigations about fringe patterns and their agreement with the theory.

5.3 Disappearing of fringe pattern

The clearly visible reduction of the fringe pattern strongly suggests that we do see the Brewster angle effect in the experiment. We especially note the disappearing of the high frequency oscillation which was attributed to interference of the (0,0) and (2,1) rays. That indicates that the (0,0) ray really goes through a local minimum in intensity. The (2,1) ray however is still there and causes low angular frequency interference with the (3,2) ray as identified earlier. We also find the observed location of the Brewster angle region in general agreement with the calculated results from both, equation 6 and the Mie theory data shown in figure 12. By comparing figures 12 and 18 we note that the general structure in the Brewster angle region is quite similar. This is a very nice result, considering the weakness of the signal.

However there is one source of error. We always tried to launch the bubbles such that they rose through the center of the laser beam. However due to the statistical nature of that process, it was not always possible for the bubble to go straight through the center of the beam. The problem in that case is that the relative magnitudes of the rays contributing to the scattering pattern could be out of proportion. Because all relevant rays enter the bubble at a different point those rays closer to the edge of the beam are weaker than they should be and

Figure 18a: Final result: background subtracted, two point averaged, scaled data, ka = 1278, a = 78.5 μm. The 85 mm lens was used. The scaling was done according to the non averaged Mie theory result of figure 12a.

Figure 18b: Final result, the same experimental data as in figure 18a, but scaled to the two point averaged Mie theory result of figure 12b.

Figure 18c: Final result, the same experimental data as in figure 18a, but scaled to the one point averaged Mie theory result of figure 12c.

Figure 18a

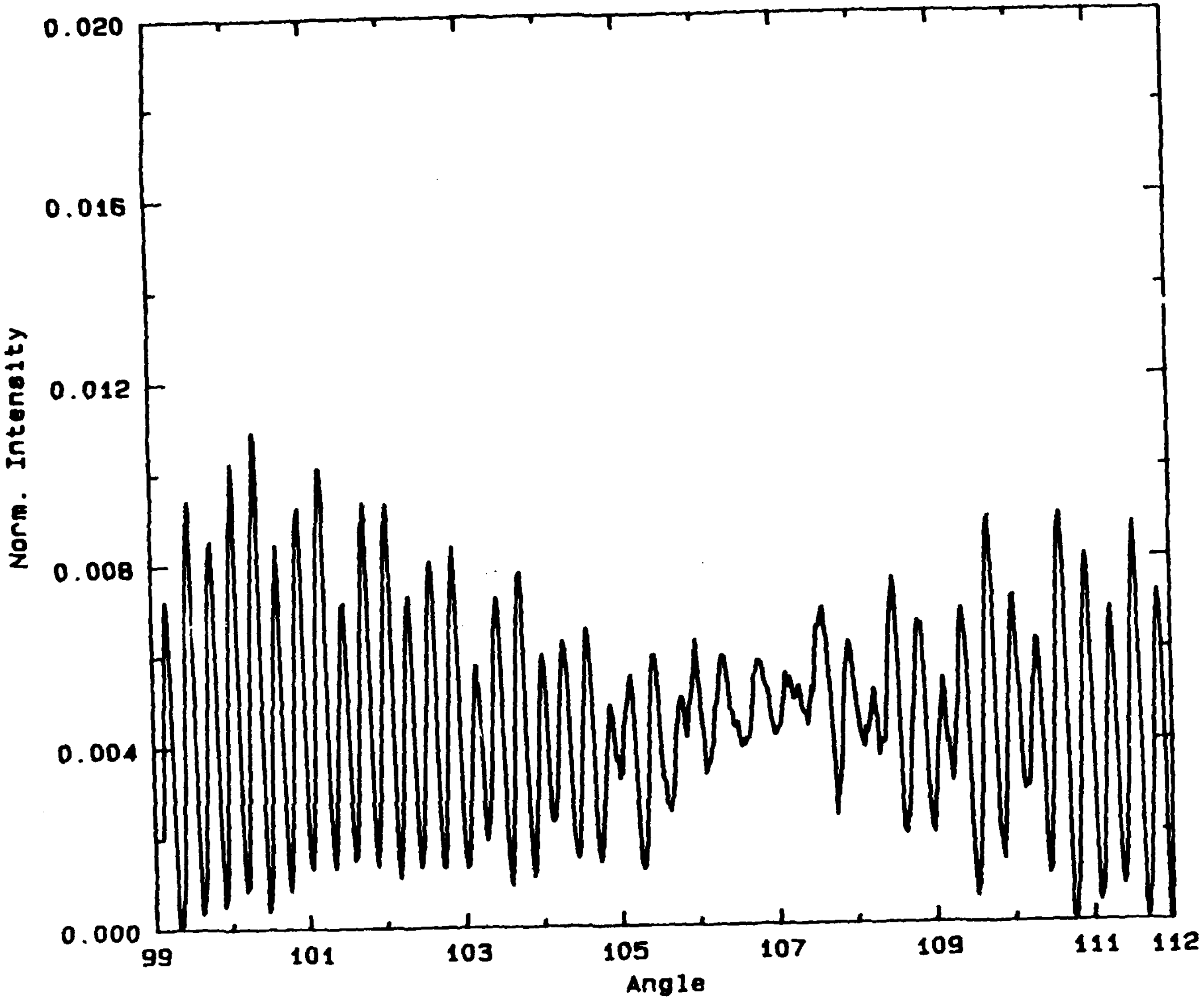
0.020
0.016
0.012
0.008
0.004
0.000
Norm. Intensity
99
101
103
105
107
109
111
112
Angle

Figure 18c

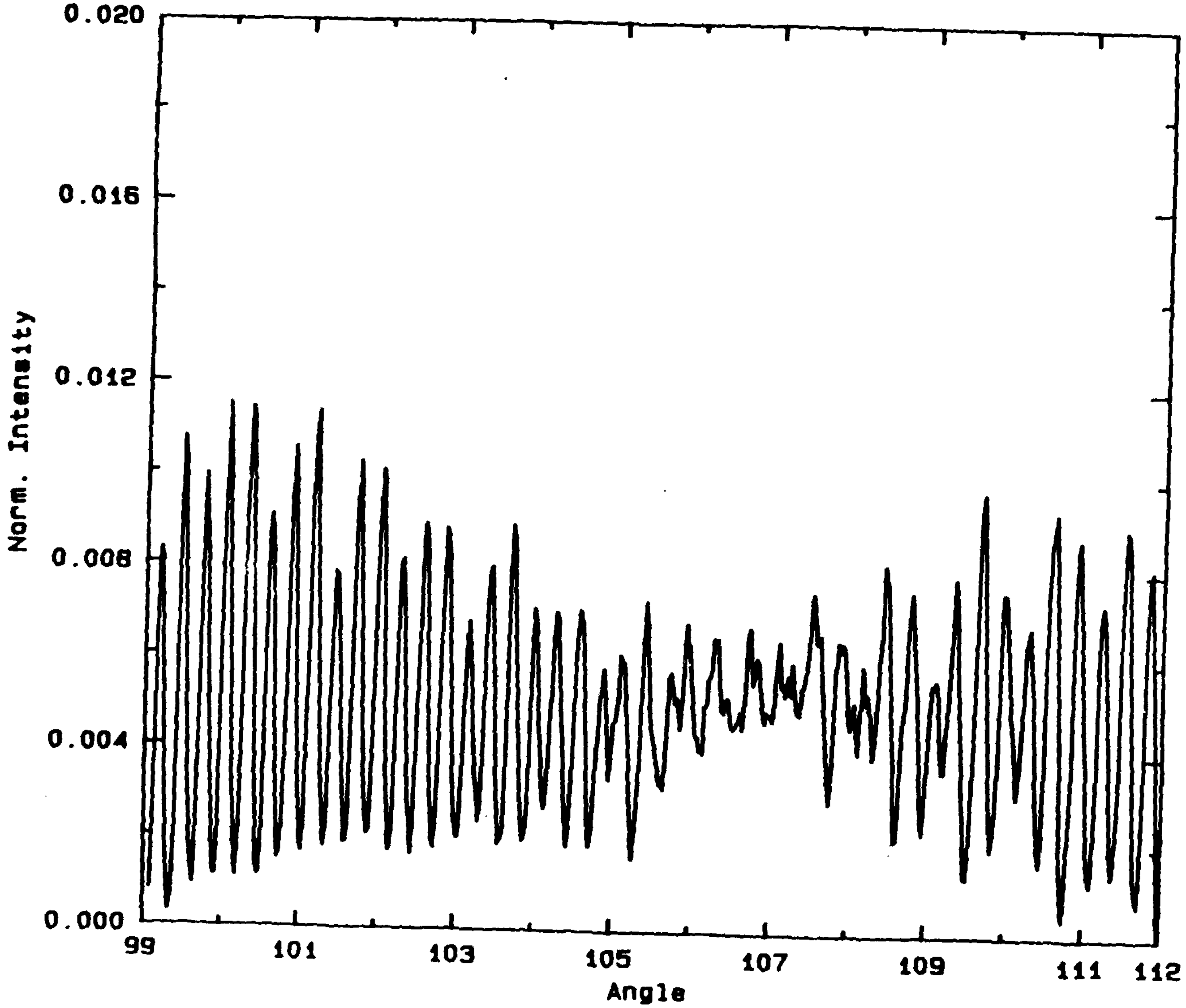
0.020
0.016
0.012
0.008
0.004
0.000
Norm. Intensity
99
101
103
105
107
109
111
112
Angle

the rays closer to the center of the beam are relatively strong. Therefore we may not always find the relative magnitude of the fringes to be as in the Mie theory results. Fortunately the bubble diameter was always much smaller than the beam width, so that this effect should usually be small.

5.4 Fringe pattern

Both experiment and theory exhibit the predicted oscillatory fine structure. As shown earlier this structure is caused by interference from mainly the (0,0) ray with the (2,1) ray. To check results of the experiment we calculate the separation between adjacent extreme $\Delta\theta$ for a given measured size using formula 11. Comparing fringe spacing between theoretical and experimental results gives information about the size of the bubble since the separation between adjacent extreme is inversely proportional to the size. Results of this comparison are shown in table 4. The numbers were obtained by superposing a very fine grid on the plot and using it to measure the period of interest. Using the measured bubble radius, the fringe spacing for all possible interferences was calculated. Then a comparison with the fringe spacing detected in the experimental data was done. In addition from the observed fringe spacing, a radius value for each bubble was calculated using the measured (0,0), (2,1) interference period. This is the most pronounced structure and in all cases the (0,0),(2,1) interference could be measured with good accuracy. This inferred radius value was then compared with the measured radius. It was found to be in general agreement considering the circumstances of the size measurement. The measuring microscope had an intrinsic error of about ±3 μm. Besides that there was always the problem of determining the edge of the bubble while trapped under the glass slide and measured. Furthermore there we had to deal with the problem of vibration. Considering the size of the bubbles, even very small vibrations could add a considerable error to the measurement. All together we believe to have an error of about ±10 μm in the measurement of the bubble diameter.

Table 4: Analysis of the occurring interferences

Figure 18

Radius of the bubble in microns		Difference
observed	calculated	
78.50000	76.3	-2.2

Interference	Angular separation in deg. calculated	observed	Difference
(0,0) (2,1)	0.291768	0.3	2.7%
(0,0) (3,1)	0.232058		
(0,0) (3,2)	0.936399	0.85	9.2%
(2,1) (3,1)	1.133936		
(2,1) (3,2)	0.423825	0.4	5.6%
(3,1) (3,2)	0.308514		

Inspection of the data reveals a low frequency modulation outside the Brewster scattering angle region caused by (0,0),(3,2) interference. Right at the Brewster scattering angle region, basically only the (2,1),(3,2) interference was found. However a problem in this region is the weakness of the signal. Therefore the signal is much more succeptible to noise, which makes it a lot harder to determine the frequency of the fringe spacing. Another source of error is the earlier discussed size measurement of the bubble. Since the fringe spacing is very sensitive to the radius of the bubble, inaccuracies in determining the size of the bubble cause variations in $\Delta\theta$. Nevertheless we get fairly good agreement between theory and experiment.

Chapter 6

Conclusion

The principal effects of Brewster angle reflection on the scattering from uncoated air bubbles in water were observed experimentally. The final results also show all the important features predicted by Mie calculations. The disappearing fringe pattern as well as the relative minimum in scattered intensity were observed experimentally. The periods of interference patterns for several refracted and reflected rays were found to agree reasonably well with the measured size of the bubble and geometrical consideration. These effects might be used to distinguish between bubbles and other scatterers[7,9]. (Solid particles in water would not show a Brewster angle effect near 106°.) Furthermore this technique might be useful to detected coatings on bubbles since the Brewster angle effect is strongly dependent upon the relative index of refraction. If investigated more, it might become a useful tool for getting information about the type of coating material and the thickness of the coat on bubbles in dielectric media[7,9].

REFERENCES

1. P.L. Marston, D.S. Langley, D.L. Kingsbury, "Light scattering by bubbles in liquids Mie theory, physical - optics approximation, and experiments," Appl. Sci. Res. 38, 373 - 383 (1982).

2. D.L. Kingsbury, P.L. Marston, "Scattering by bubbles in glass: Mie theory and physical optics approximation," App. Opt. 20, 2348 - 2350 (1981).

3. P.L. Marston, D.L. Kingsbury, "Scattering by a bubble in water near the critical angle: interference effects," J. Opt. Soc. Am. 71, 192 - 196 (1981); 71, 917(E) (1981).

4. D.S. Langley, P.L. Marston, "Critical - angle scattering of laser light from bubbles in water: measurements, models, and application to sizing of bubbles," App. Opt. 23, 1044 - 1054 (1984).

5. P.L. Marston, D.S. Langley, "Glory in backscattering: Mie and model predictions for bubbles and conditions on refractive index in drops," J. Opt. Soc. Am. 72, 456 - 459 (1982).

6. D.S. Langley, P.L. Marston, "Scattering of laser light from bubbles in water at angles from 68 to 85 degrees," Proc. SPIE 489, Ocean Optics VII 142 - 145 (1984).

7. P.L. Marston, S.C. Billette, C.E. Dean, "Scattering of light by a coated bubble in water near the critical and Brewster scattering angles," Proc. SPIE 925, Ocean Optics IX (in press).

8. P.L. Marston, J.L. Johnson, S.P. Love, B.L. Brim, "Critical - angle scattering of white light from a cylindrical bubbles in glass: photographs of colors and computations," J. Opt. Soc. Am. 73, 1658 - 1664 (1983).

9. S.C. Billette, "Computational analysis of the effects of surface films on the optical scattering properties of bubbles in water," Master's thesis (Washington Sate University, Pullman, WA., 1986). Available from Defense Technical Information Center (Alexandria, VA) Accession No. AD - A173992.

10. D.S. Langley, P.L. Marston, "Glory in optical backscattering from air bubbles," Phys. Rev. Lett. 43, 913 - 916 (1981).

11. G.E. Davis, "Scattering of light by an air bubble in water," J. Opt. Soc. Am. 45, 572 - 581 (1955).

12. G.M. Hale, M.R. Querry, "Optical constants of water in the 200-nm to 200-µm wavelength region," App. Opt. 12, 555 - 561 (1973).

13. H.C. van de Hulst, Light scattering by small particles (Dover, N.Y. 1981).

14. J.W. Goodman, Introduction to Fourier optics (McGraw - Hill, N.Y. 1968).

15. M. Born, E. Wolf, Principles of optics (Pergamon Press, N.Y. 1980).

16. E. Hecht, Optics (Addison - Wesley, Reading, MA 1987).

17. M. Kerker, The scattering of light and other electromagnetic radiation (Academic Press, N.Y. 1969).

18. W.J. Wiscombe, "Improved Mie scattering algorithms," Appl. Opt. 19, 1505 - 1509 (1980).

19. M.V. Klein, T.E. Furtak, Optics (Wiley, N.Y. 1986).

20. G. Mie, "Beiträge zur Optik trüber Medien, speziell kolloidaler Metallösungen," Ann. Phys. 25, 377 - 445 (1908).

21. D. Brewster, "On the laws which regulate the polarization of light by reflection from transparent bodies," Phil. Trans. (London) 125 - 159 (1815).

BLANK

APPENDIX A

A. Additional data

In the Appendix a few more examples of experimental data shall be presented. For each case the experimental data is shown next to the Mie theory results. This is done with and without the two-point average. Furthermore a complete analysis of all detectable fringes was done. The results were obtained in the same way as described earlier.

Table A1: Analysis of the occurring interferences

Figure A1

Radius of the bubble in microns		Difference
observed	calculated	
61.00000	65.4	+4.4

Interference	Angular separation in deg.		Difference
	calculated	observed	
(0,0) (2,1)	0.375472	0.35	6.8%
(0,0) (3,1)	0.298632		
(0,0) (3,2)	1.205037	1.1	8.7%
(2,1) (3,1)	1.459246		
(2,1) (3,2)	0.545415	0.52	4.7%
(3,1) (3,2)	0.397022		

Figure A2

Radius of the bubble in microns		Difference
observed	calculated	
80.00000	76.3	-3.7

Interference	Angular separation in deg.		Difference
	calculated	observed	
(0,0) (2,1)	0.286297	0.3	4.6%
(0,0) (3,1)	0.227707		
(0,0) (3,2)	0.918841	0.9	2.1%
(2,1) (3,1)	1.112675		
(2,1) (3,2)	0.415879	0.4	3.8%
(3,1) (3,2)	0.302729		

Figure A3

Radius of the bubble in microns		Difference
observed	calculated	
72.00000	76.3	+4.3

Interference	Angular separation in deg.		
	calculated	observed	Difference
(0,0) (2,1)	0.318108	0.3	5.7%
(0,0) (3,1)	0.253008		
(0,0) (3,2)	1.020935	0.85	16.7%
(2,1) (3,1)	1.236306		
(2,1) (3,2)	0.462087	0.45	2.6%
(3,1) (3,2)	0.336366		

Figure A4

Radius of the bubble in microns		Difference
observed	calculated	
73.50000	65.4	-8.1

Interference	Angular separation in deg.		
	calculated	observed	Difference
(0,0) (2,1)	0.311616	0.35	11.0%
(0,0) (3,1)	0.247844		
(0,0) (3,2)	1.000099	1.025	2.5%
(2,1) (3,1)	1.211075		
(2,1) (3,2)	0.452657	0.55	17.3%
(3,1) (3,2)	0.329501		

Figure A5

Radius of the bubble in microns observed	 calculated	Difference
71.50000	83.4	+11.9

Interference	Angular separation in deg. calculated	 observed	Difference
(0,0) (2,1)	0.320332	0.275	14.2%
(0,0) (3,1)	0.254777		
(0,0) (3,2)	1.028074	0.825	19.8%
(2,1) (3,1)	1.244951		
(2,1) (3,2)	0.465319	0.45	3.3%
(3,1) (3,2)	0.338718		

Figure A6

Radius of the bubble in microns observed	 calculated	Difference
61.50000	65.4	+3.9

Interference	Angular separation in deg. calculated	 observed	Difference
(0,0) (2,1)	0.372419	0.35	6.0%
(0,0) (3,1)	0.296204		
(0,0) (3,2)	1.195240	1.1	8.0%
(2,1) (3,1)	1.447382		
(2,1) (3,2)	0.540980	0.55	1.6%
(3,1) (3,2)	0.393794		

<u>Figure A1.1a:</u> Experimental data, ka = 993, a = 61 μm, 135 mm lens, two point averaged and scaled to the non averaged Mie theory result.

<u>Figure A1.2a:</u> Mie theory result, ka = 993, non averaged

<u>Figure A1.1b:</u> Experimental data as in figure A1.1a, but scaled to the averaged Mie theory result.

<u>Figure A1.2b:</u> Mie theory result as in figure A1.2a, but two point averaged.

Figure A1.1a

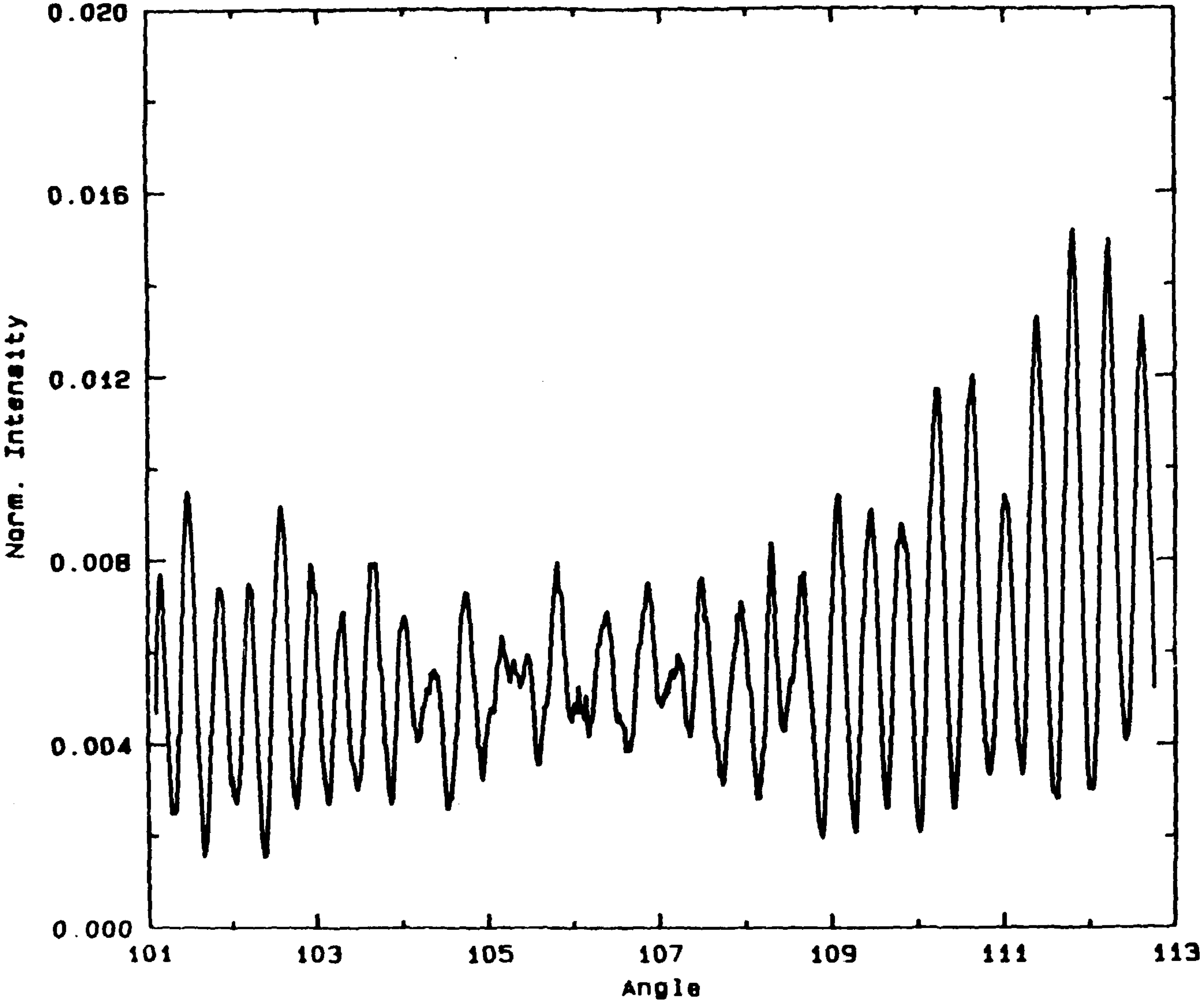
0.020
0.016
0.012
0.008
0.004
0.000
Norm. Intensity
101
103
105
107
109
111
113
Angle

Figure A1.1b

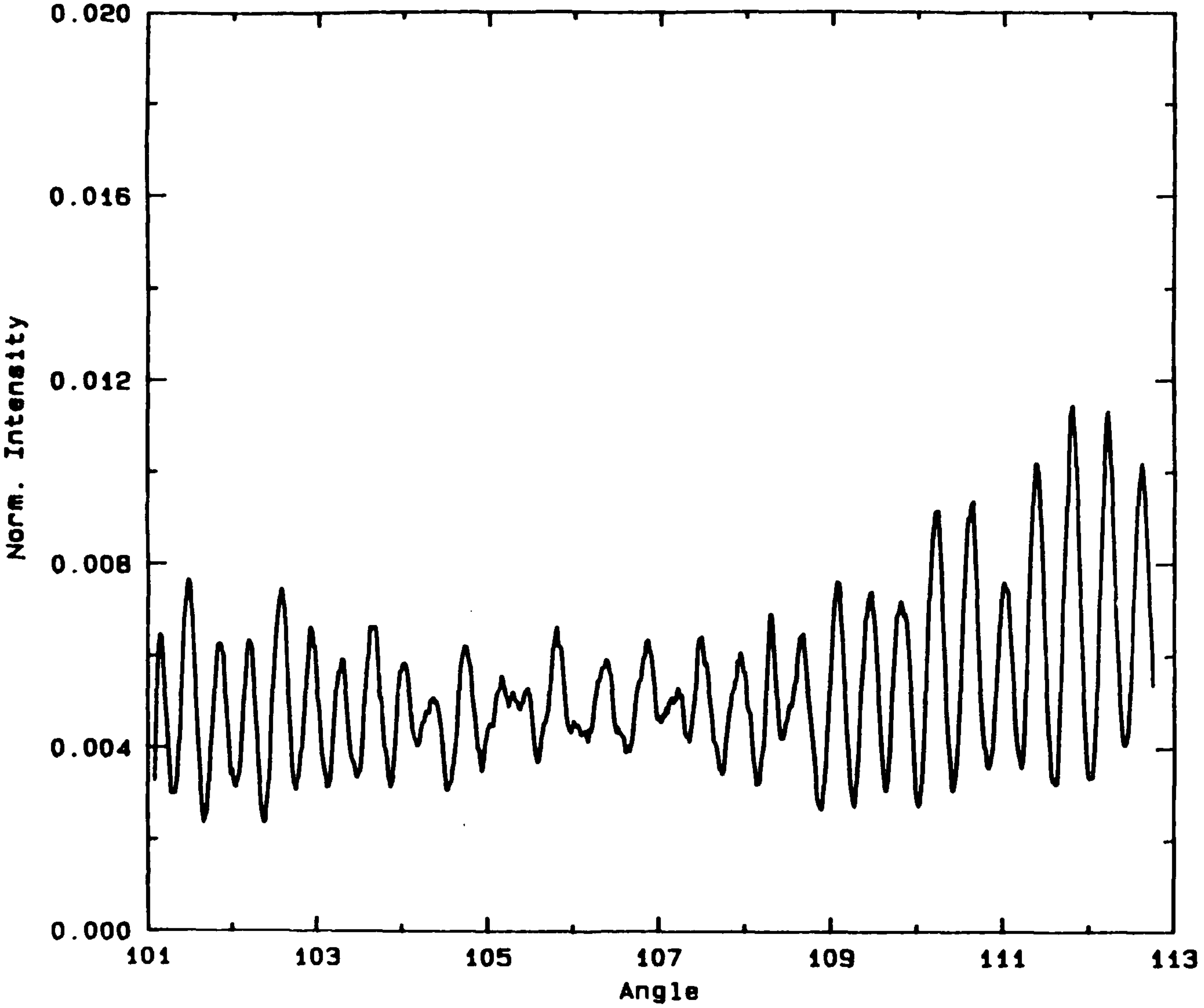
0.020
0.016
0.012
0.008
0.004
0.000
Norm. Intensity
101
103
105
107
109
111
113
Angle

Figure A1.2e

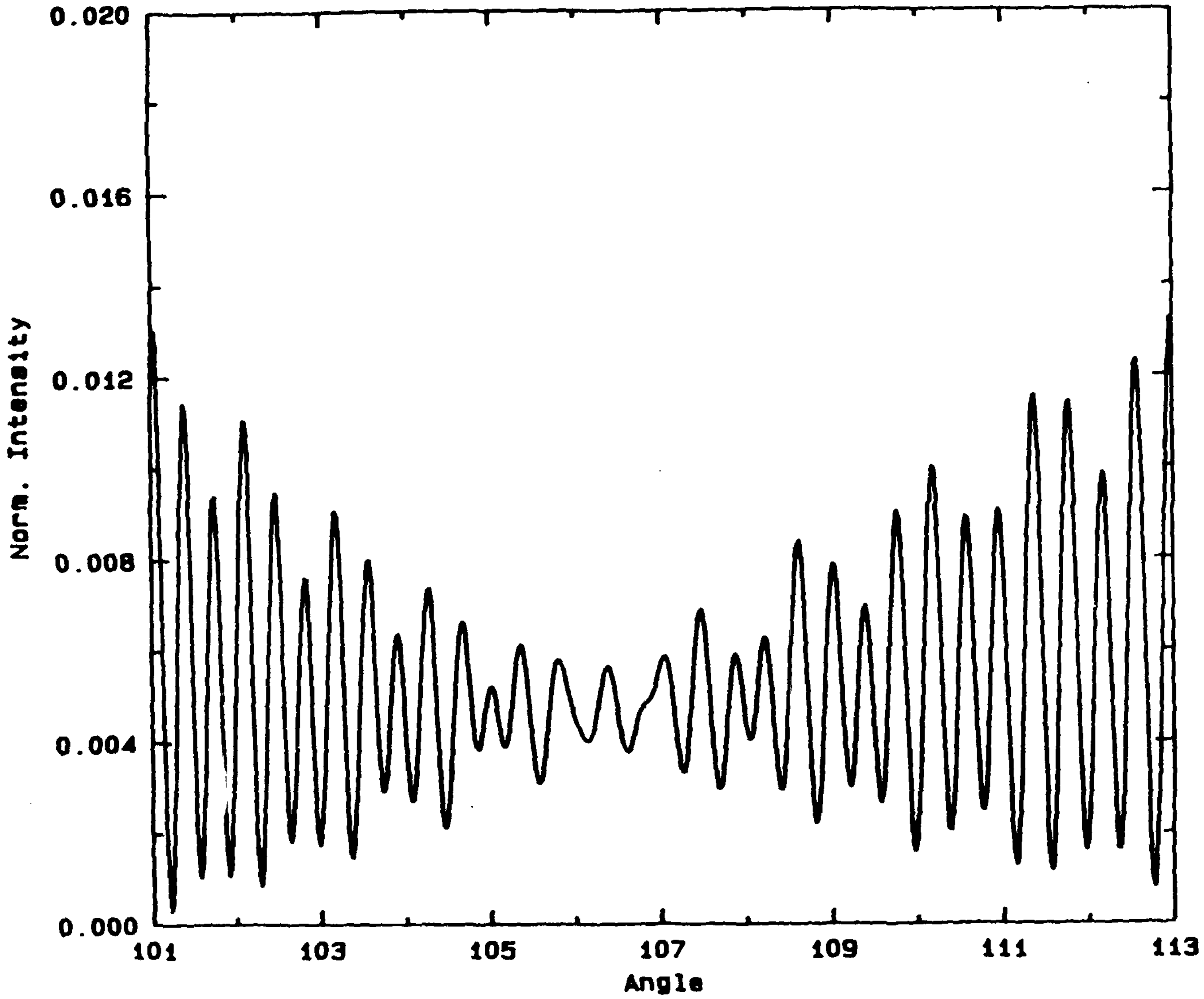
0.020
0.016
0.012
0.008
0.004
0.000
Norm. Intensity
101
103
105
107
109
111
113
Angle

Figure A1.2b

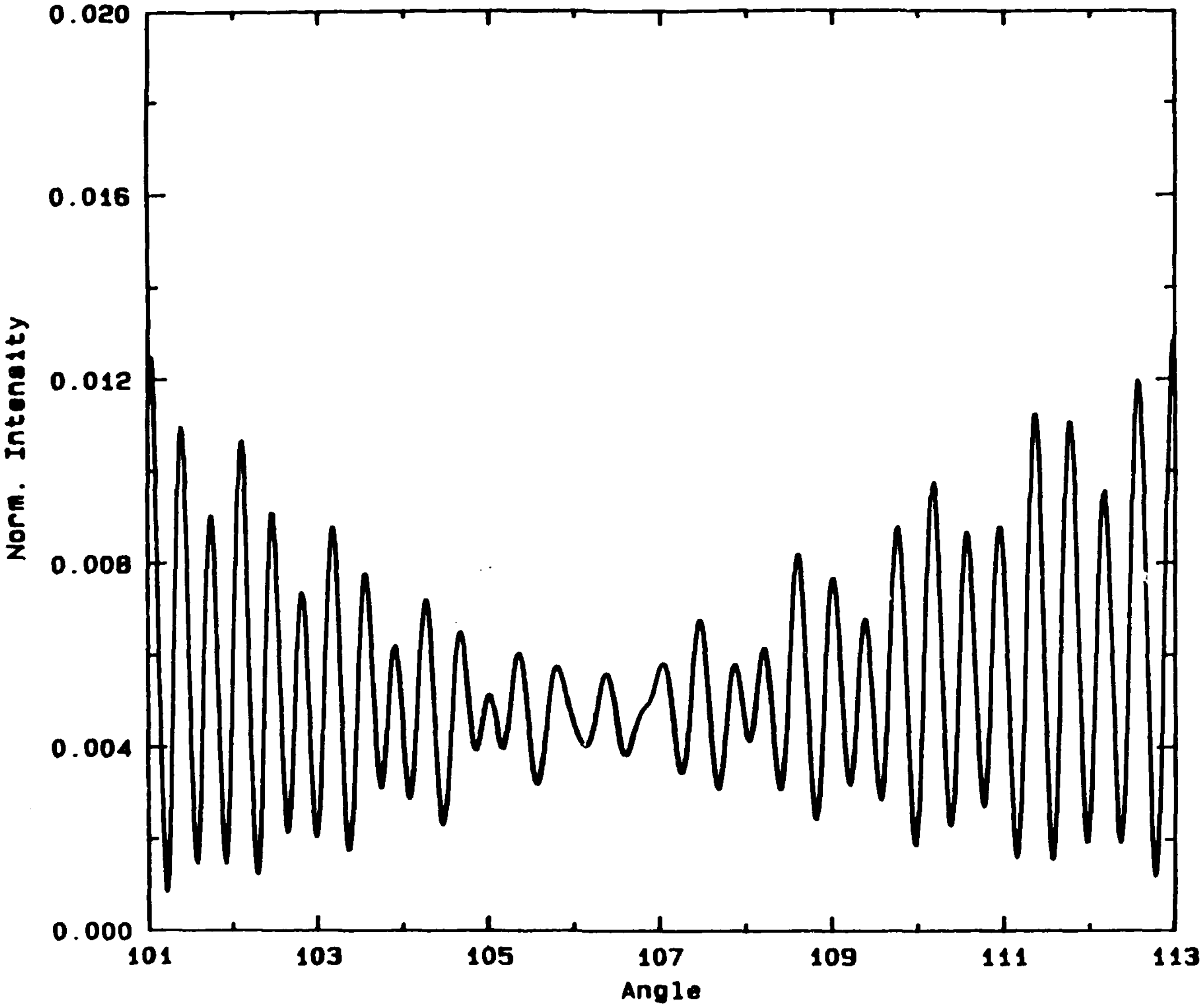
0.020
0.016
0.012
0.008
0.004
0.000
Norm. Intensity
101
103
105
107
109
111
113
Angle

BLANK

Figure A2.1a: Experimental data, ka = 1303, a = 80 μm, 135 mm lens, two point averaged, scaled to the non averaged Mie theory result

Figure A2.2a: Mie theory result, ka = 1303, non averaged

Figure A2.1b: Experimental data as in figure A2.1a, but scaled to the averaged Mie theory result.

Figure A2.2b: Mie theory result as in figure A2.2a, but two point averaged.

Figure A2.1a

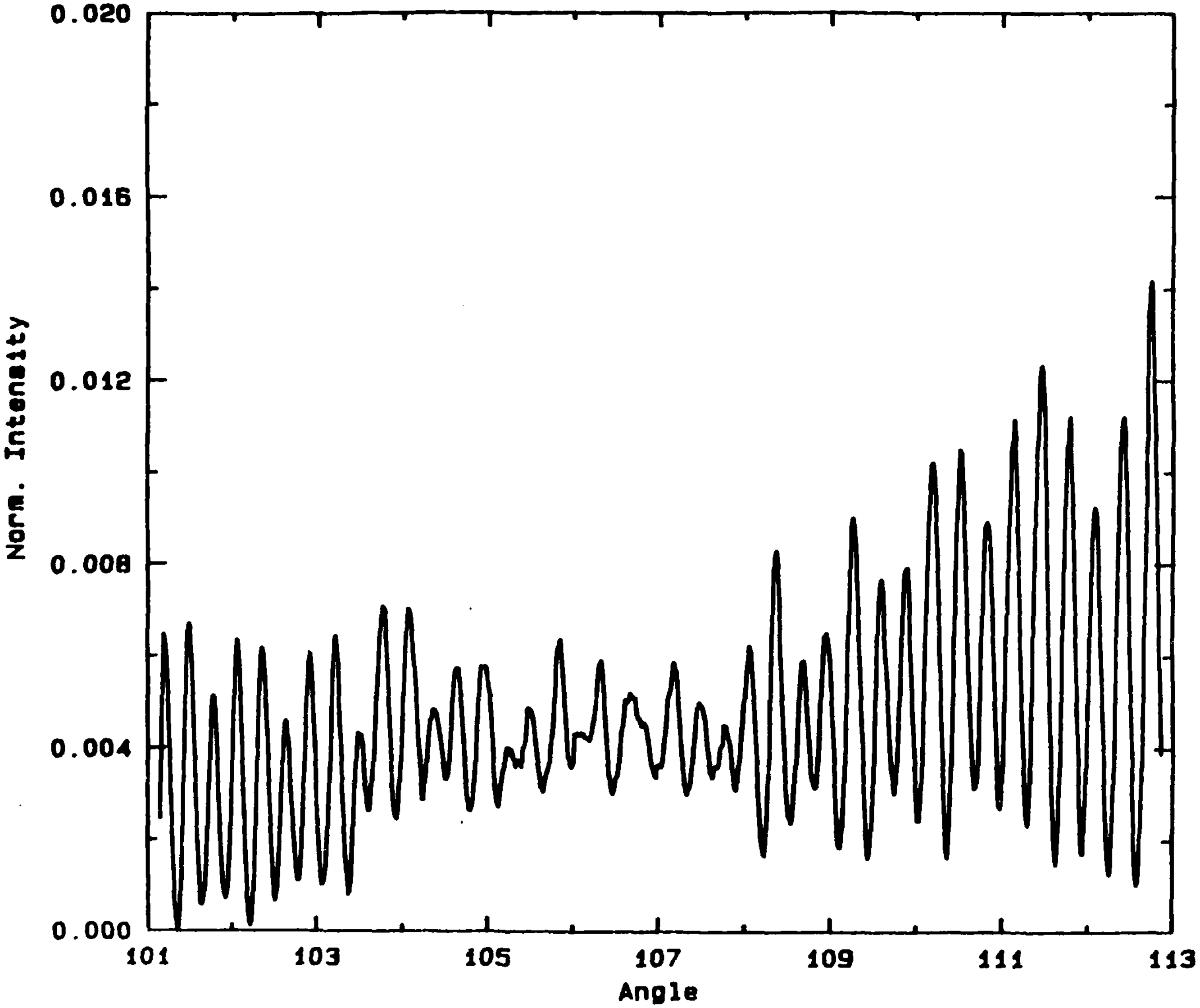
0.020
0.016
0.012
0.008
0.004
0.000
Norm. Intensity
101
103
105
107
109
111
113
Angle

Figure A2.1b

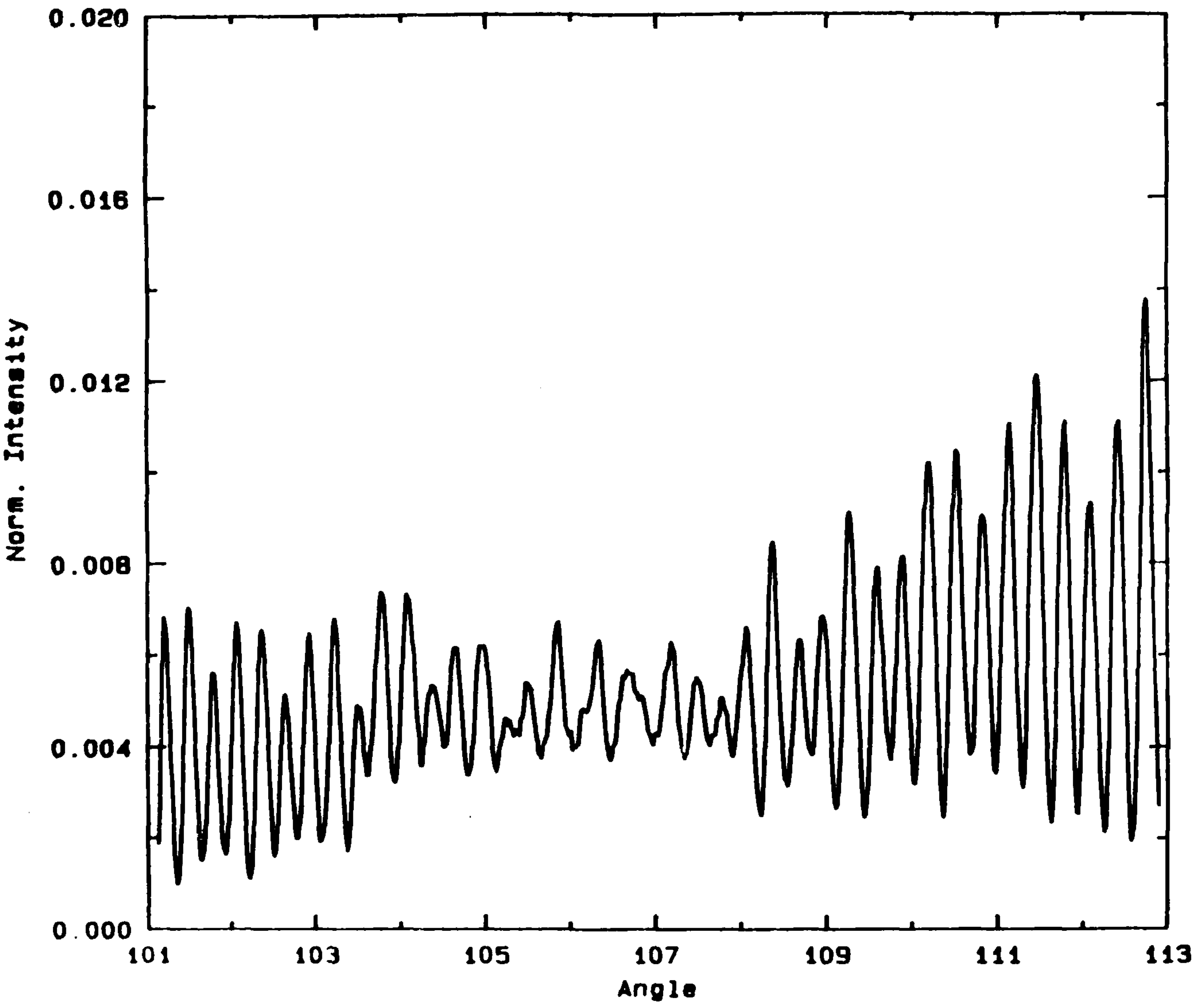
0.020
0.016
0.012
0.008
0.004
0.000
Norm. Intensity
101
103
105
107
109
111
113
Angle

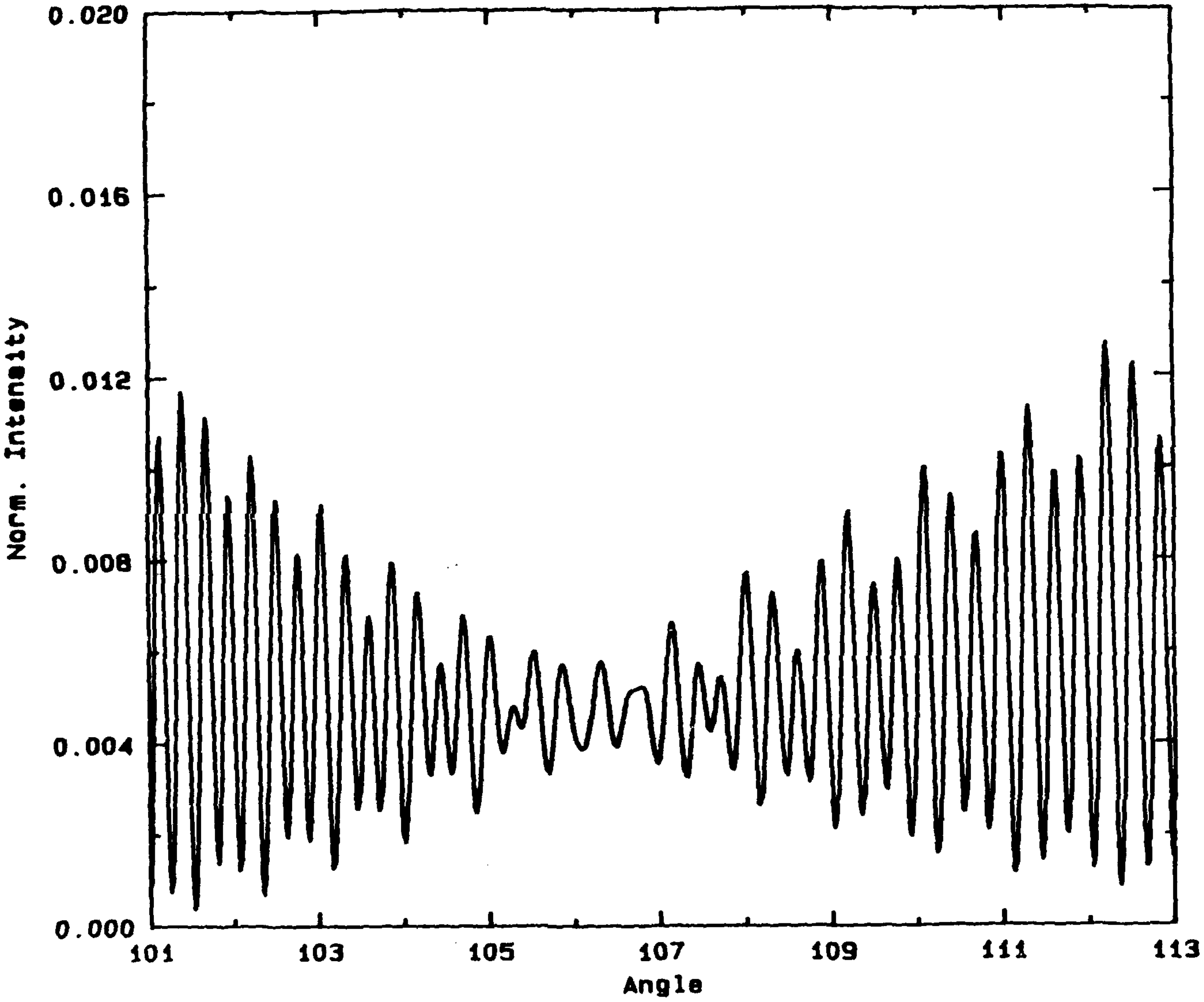

Figure A2.2a

Norm. Intensity
0.020
0.016
0.012
0.008
0.004
0.000
101
103
105
107
109
111
113
Angle

Figure A2.2b

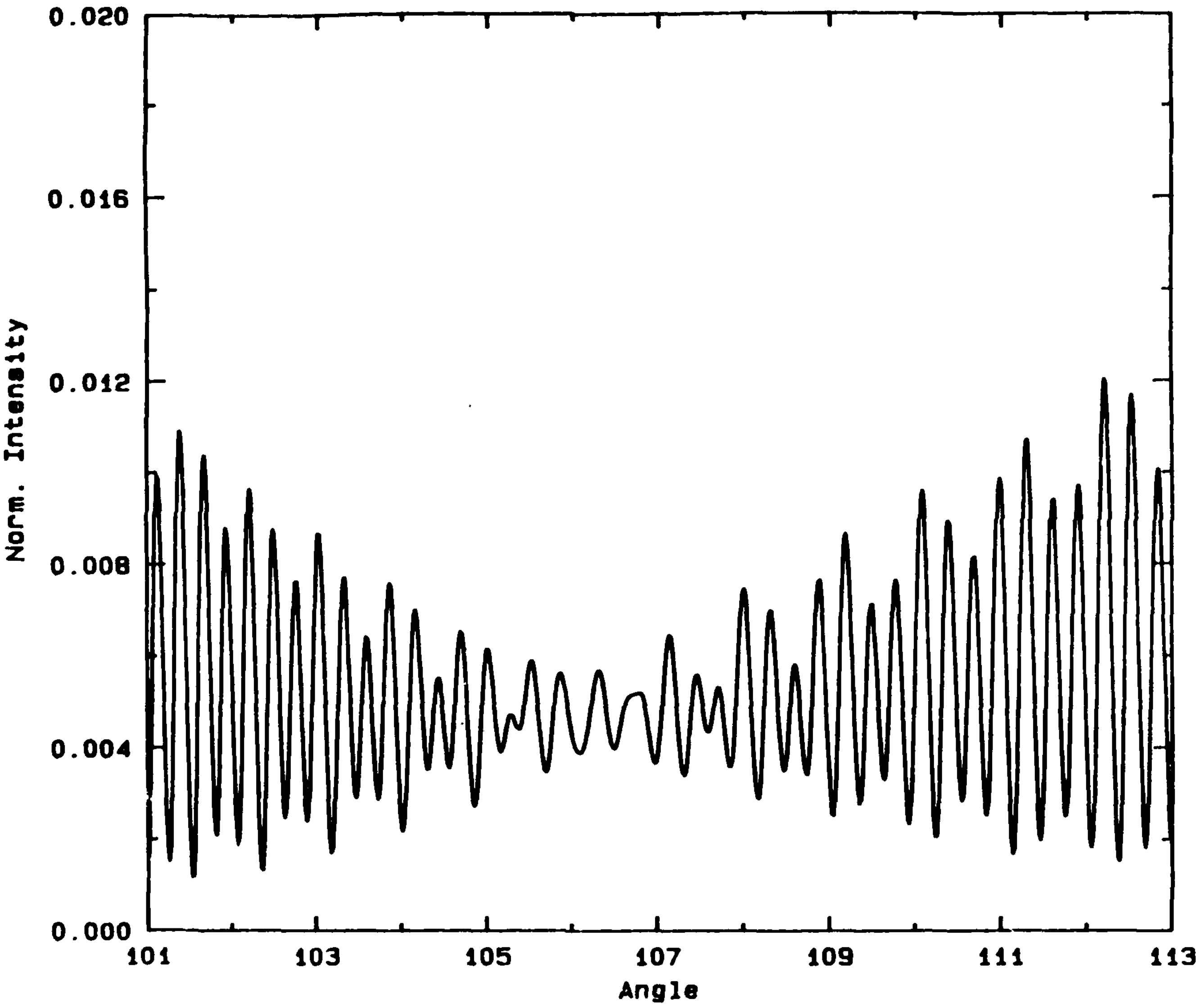
0.020
0.016
0.012
0.008
0.004
0.000
Norm. Intensity
101
103
105
107
109
111
113
Angle

BLANK

Figure A3.1a: Experimental data, ka = 1172, a = 72 μm, 85 mm lens, two point averaged, scaled to the non averaged Mie theory.

Figure A3.2a: Mie theory result, ka = 1172, non averaged

Figure A3.1b: Experimental data as in figure A3.1a, but scaled to the averaged Mie theory result.

Figure A3.2b: Mie theory result as in figure A3.2a, but two point averaged.

Figure A3.1a

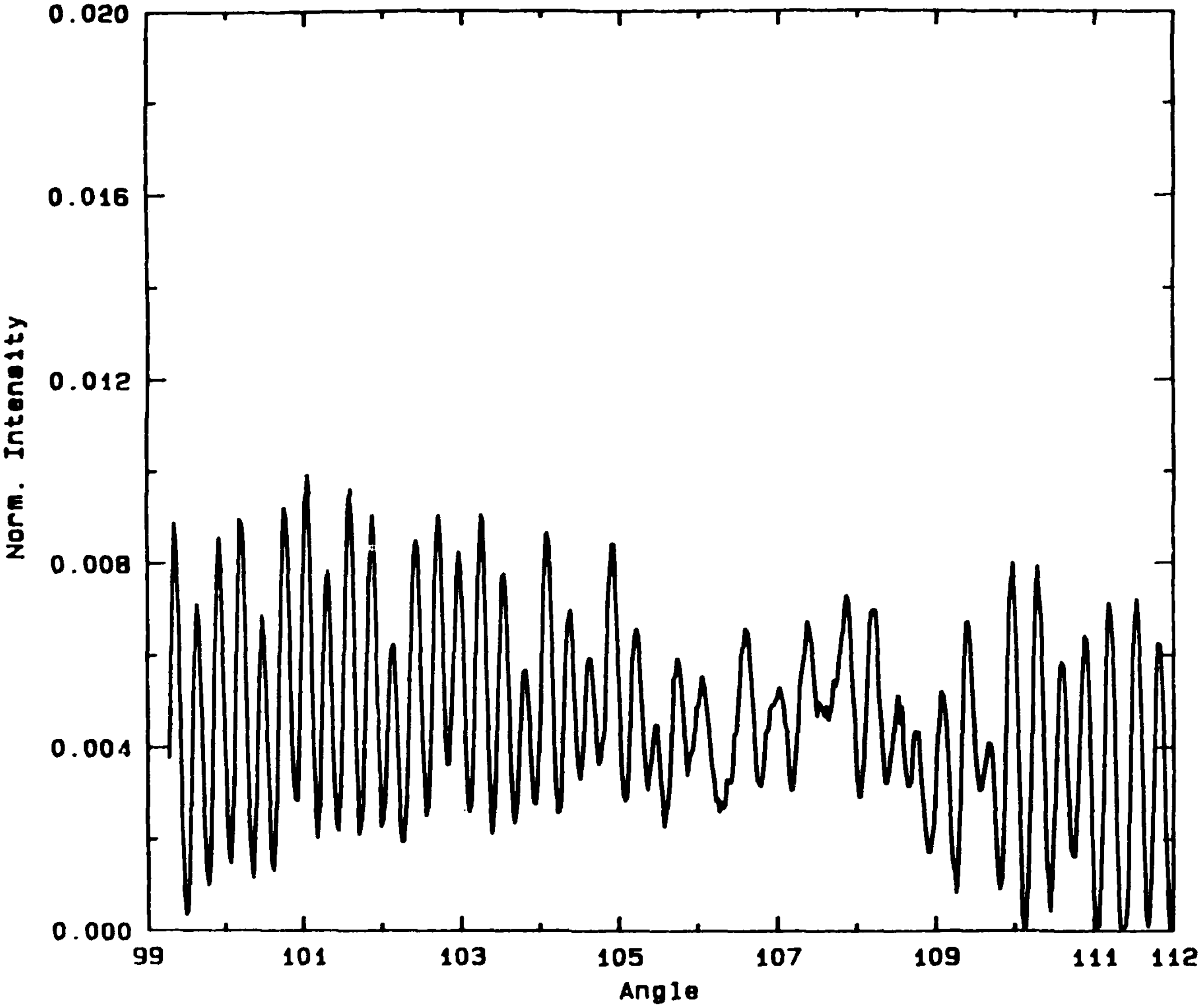
0.020
0.016
0.012
0.008
0.004
0.000
Norm. Intensity
99
101
103
105
107
109
111
112
Angle

Figure A3.1a

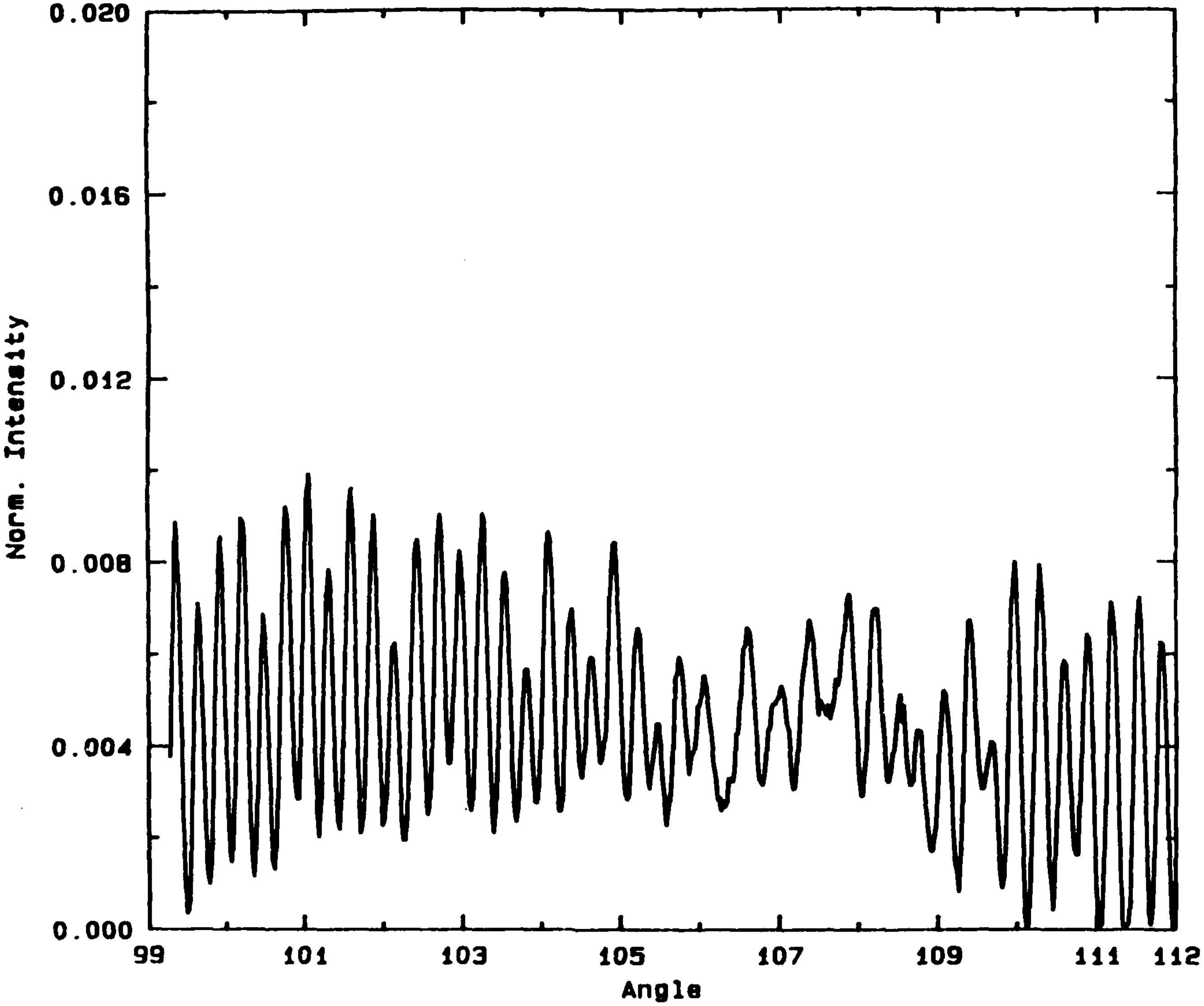
0.020
0.016
0.012
0.008
0.004
0.000
Norm. Intensity
99
101
103
105
107
109
111
112
Angle

Figure A3.1b

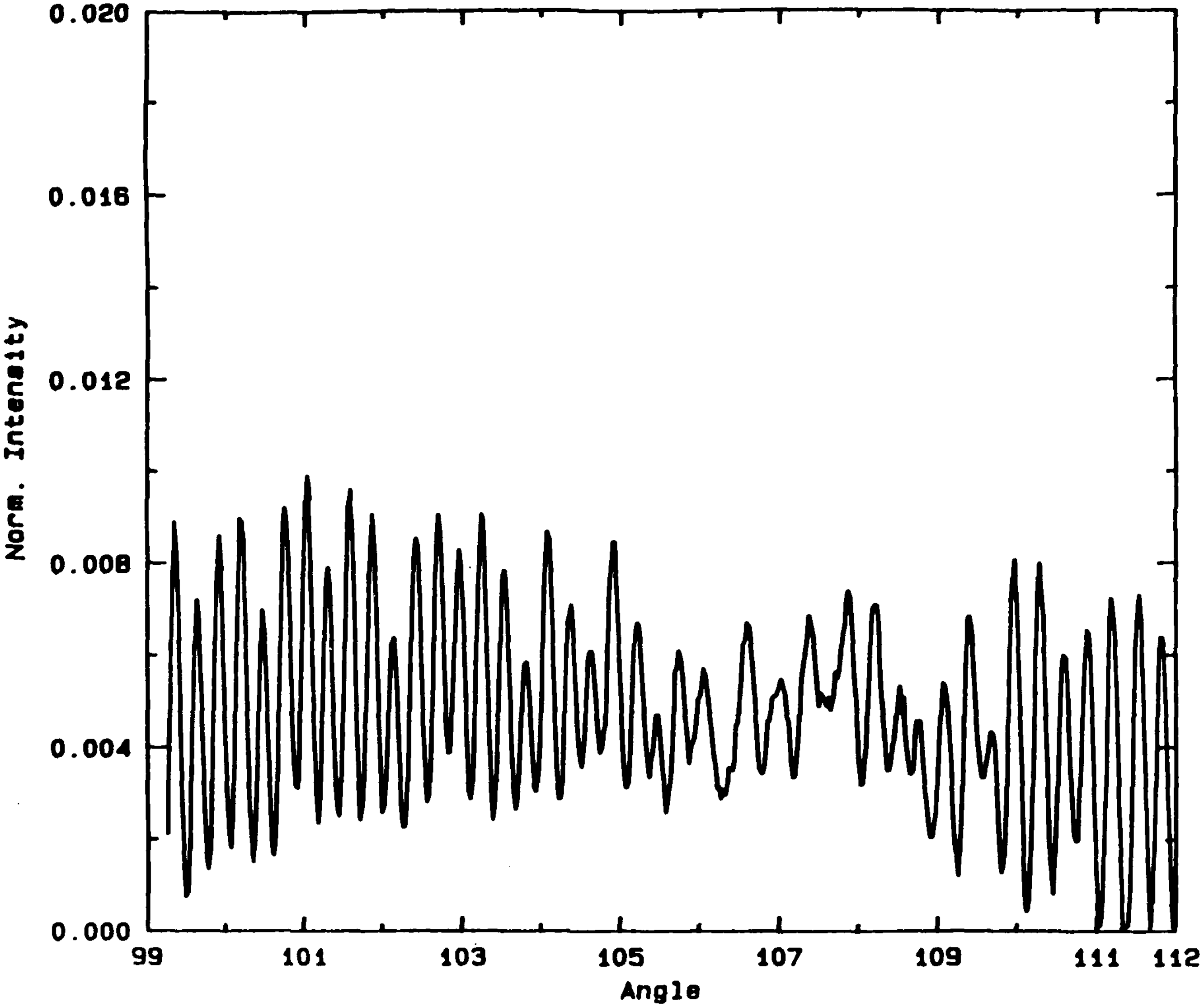
0.020
0.016
0.012
0.008
0.004
0.000
Norm. Intensity
99
101
103
105
107
109
111
112
Angle

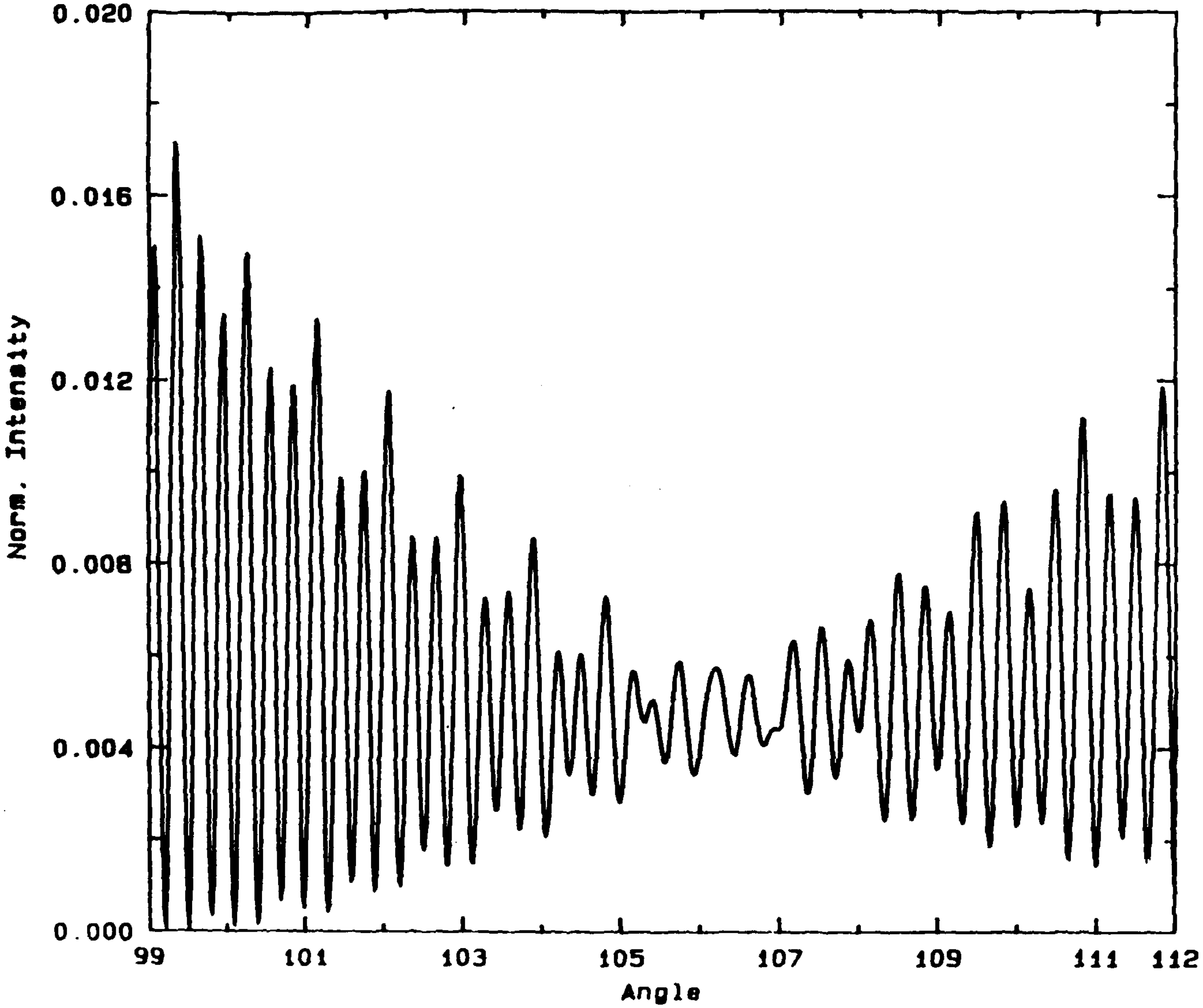
0.020
0.016
0.012
0.008
0.004
0.000
Norm. Intensity
99
101
103
105
107
109
111
112
Angle

Figure A3.2a

Figure A3.2b

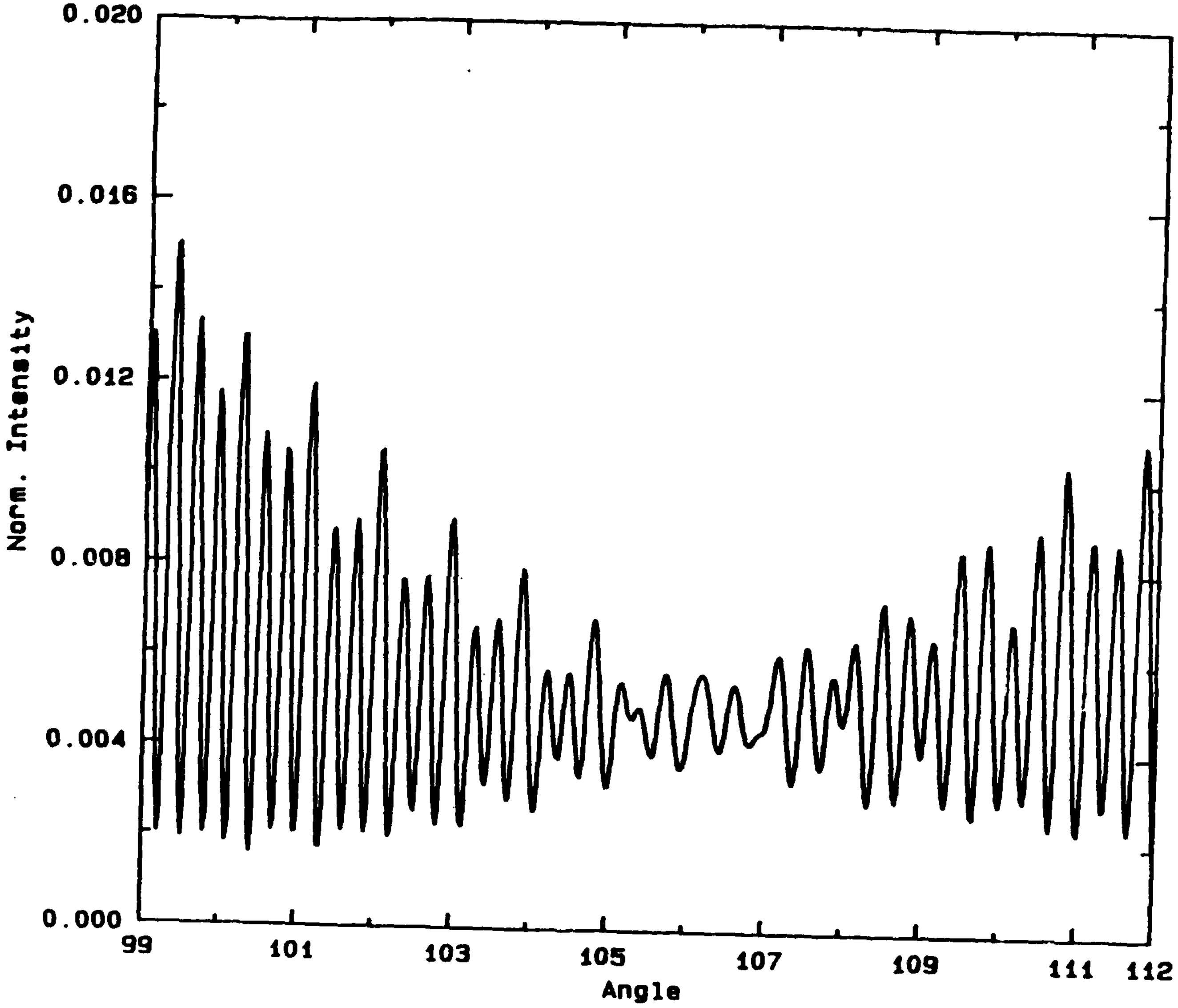
0.020
0.016
0.012
0.008
0.004
0.000
Norm. Intensity
99
101
103
105
107
109
111
112
Angle

BLANK

Figure A4.1a: Experimental data, ka = 1197, a = 73.5 μm, 85 mm lens, two point averaged, scaled to the non averaged Mie theory result.

Figure A4.2a: Mie theory result, ka = 1197, non averaged.

Figure A4.1b: Experimental data as in figure A4.1a, but scaled to the averaged Mie theory result.

Figure A4.2b: Mie theory result as in figure A4.2a, but two point averaged.

Figure A4.1a

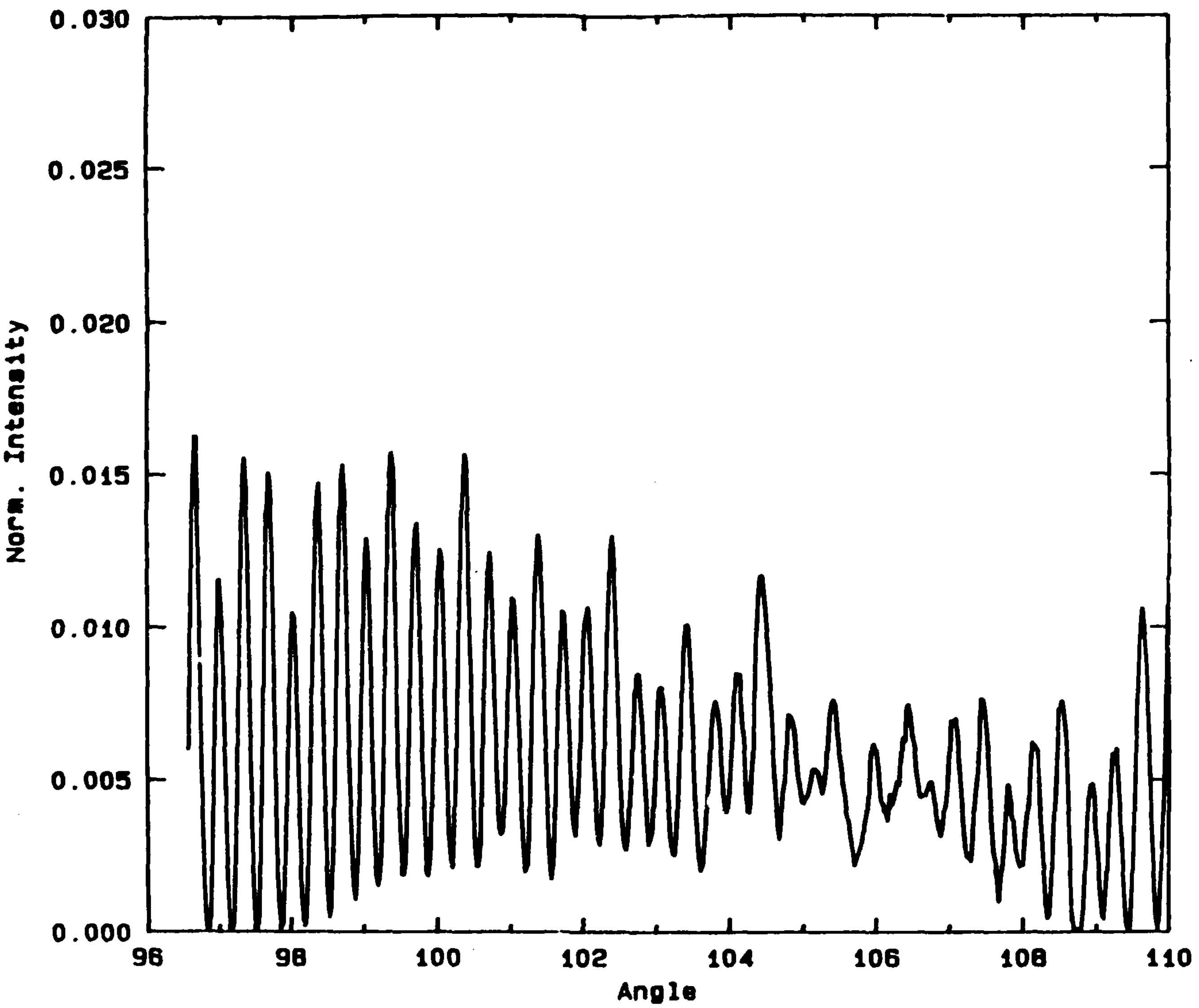
Norm. Intensity
0.030
0.025
0.020
0.015
0.010
0.005
0.000
96
98
100
102
104
106
108
110
Angle

Figure A4.1b

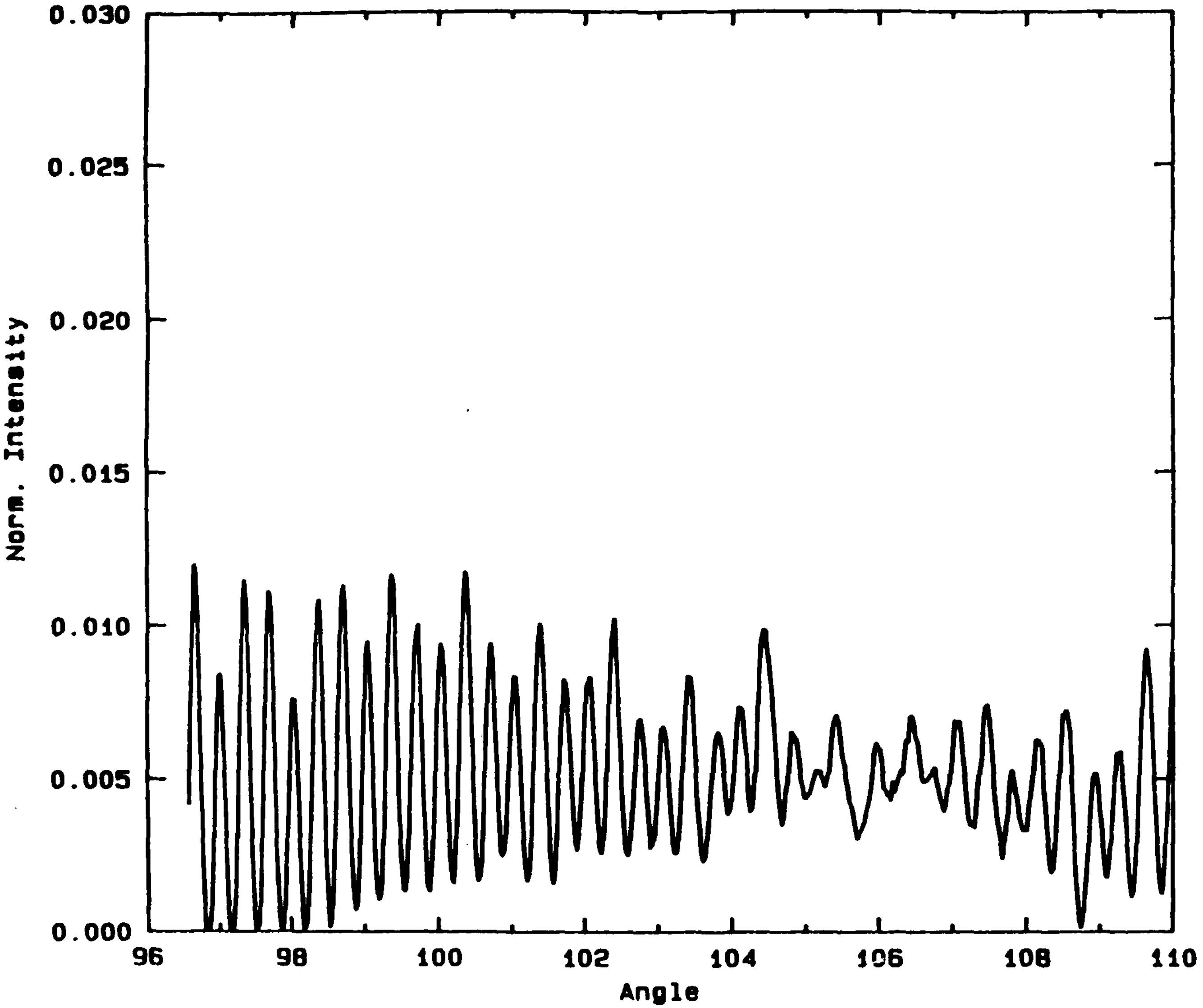
0.030
0.025
0.020
0.015
0.010
0.005
0.000
Norm. Intensity
96
98
100
102
104
106
108
110
Angle

Figure A4.2a

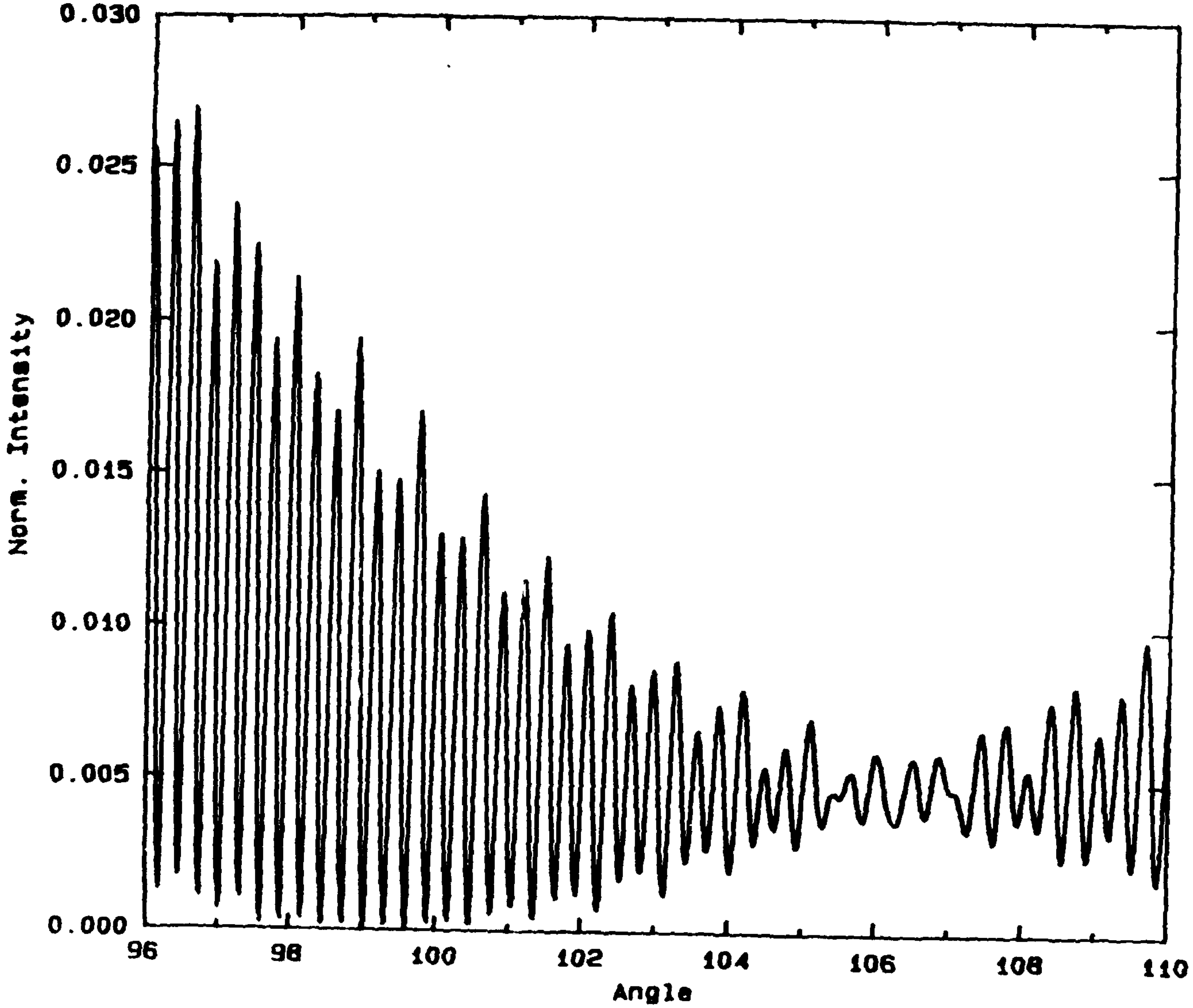
0.030
0.025
0.020
0.015
0.010
0.005
0.000
Norm. Intensity
96
98
100
102
104
106
108
110
Angle

Figure A4.2b

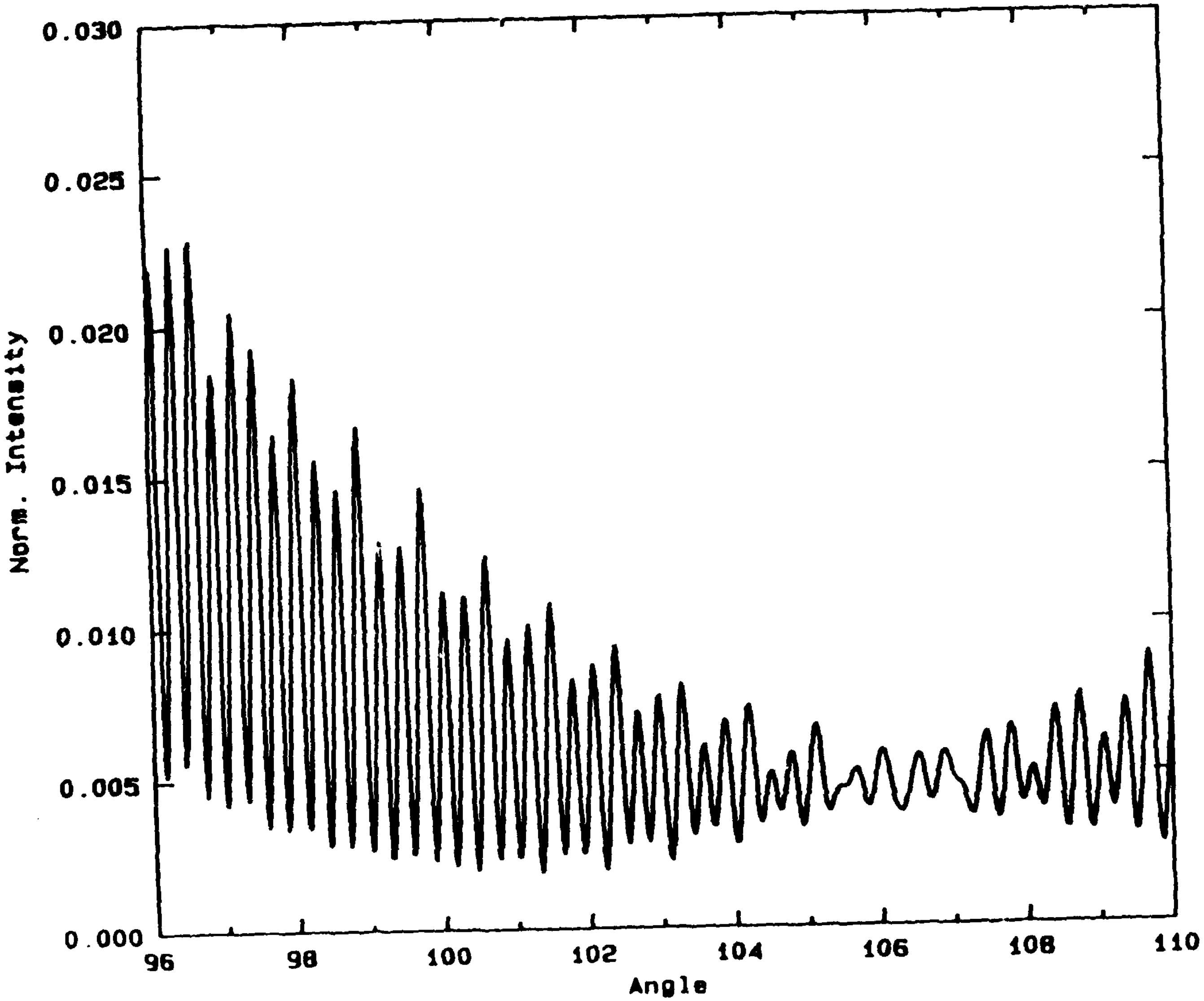
0.030
0.025
0.020
0.015
0.010
0.005
0.000
Norm. Intensity
96
98
100
102
104
106
108
110
Angle

BLANK

Figure A5.1a: Experimental data, ka = 1164, a = 71.5 µm, 85 mm lens, two point averaged, scaled to the non averaged Mie theory.

Figure A5.2a: Mie theory result, ka = 1164, non averaged.

Figure A5.1b: Experimental data as in figure A5.1a, but scaled to the averaged Mie theory result.

Figure A5.2b: Mie theory result as in figure A5.2a, but two point averaged.

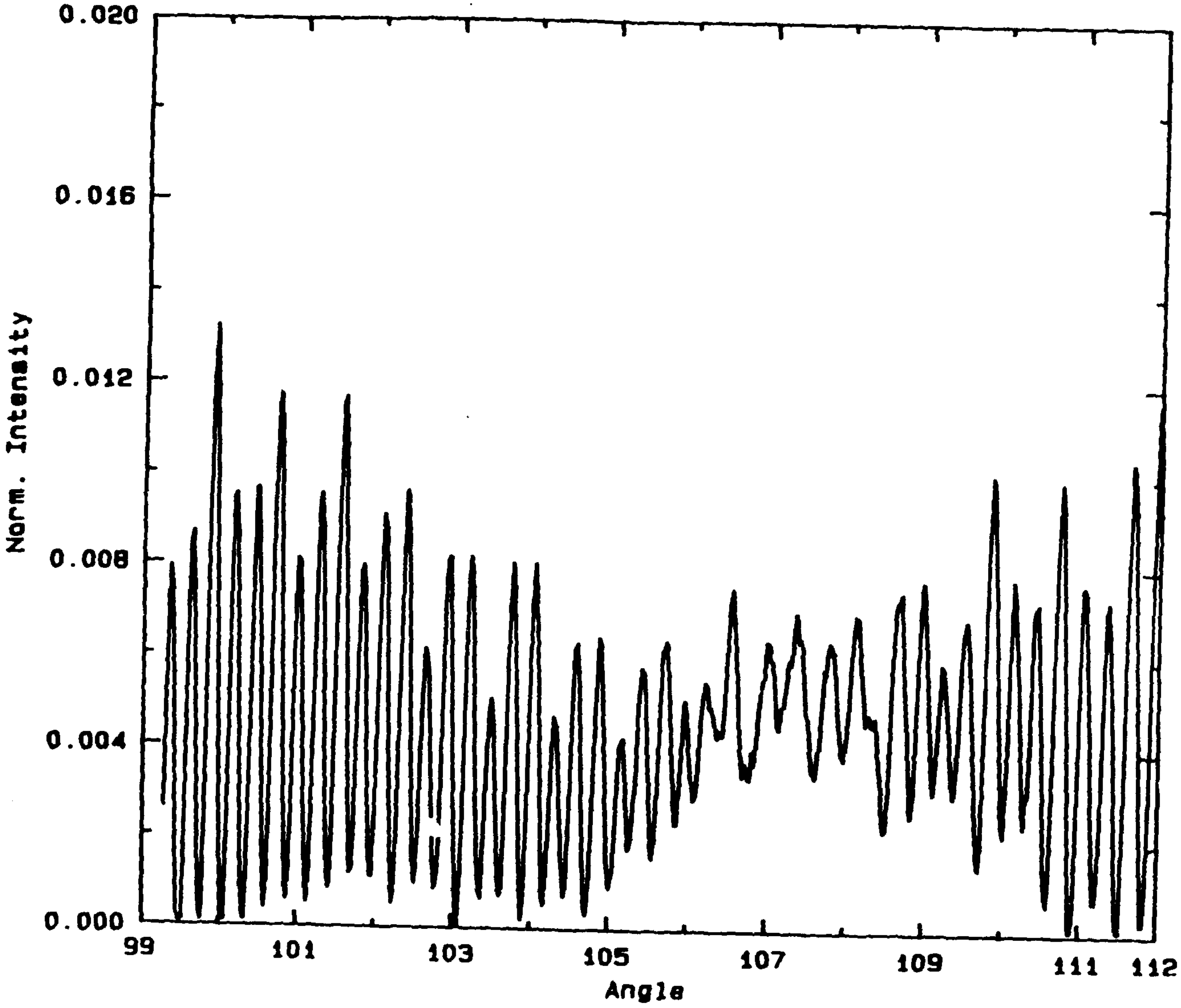

Figure A5.1a

0.020
0.016
0.012
0.008
0.004
0.000
Norm. Intensity
99
101
103
105
107
109
111
112
Angle

Figure A5.1b

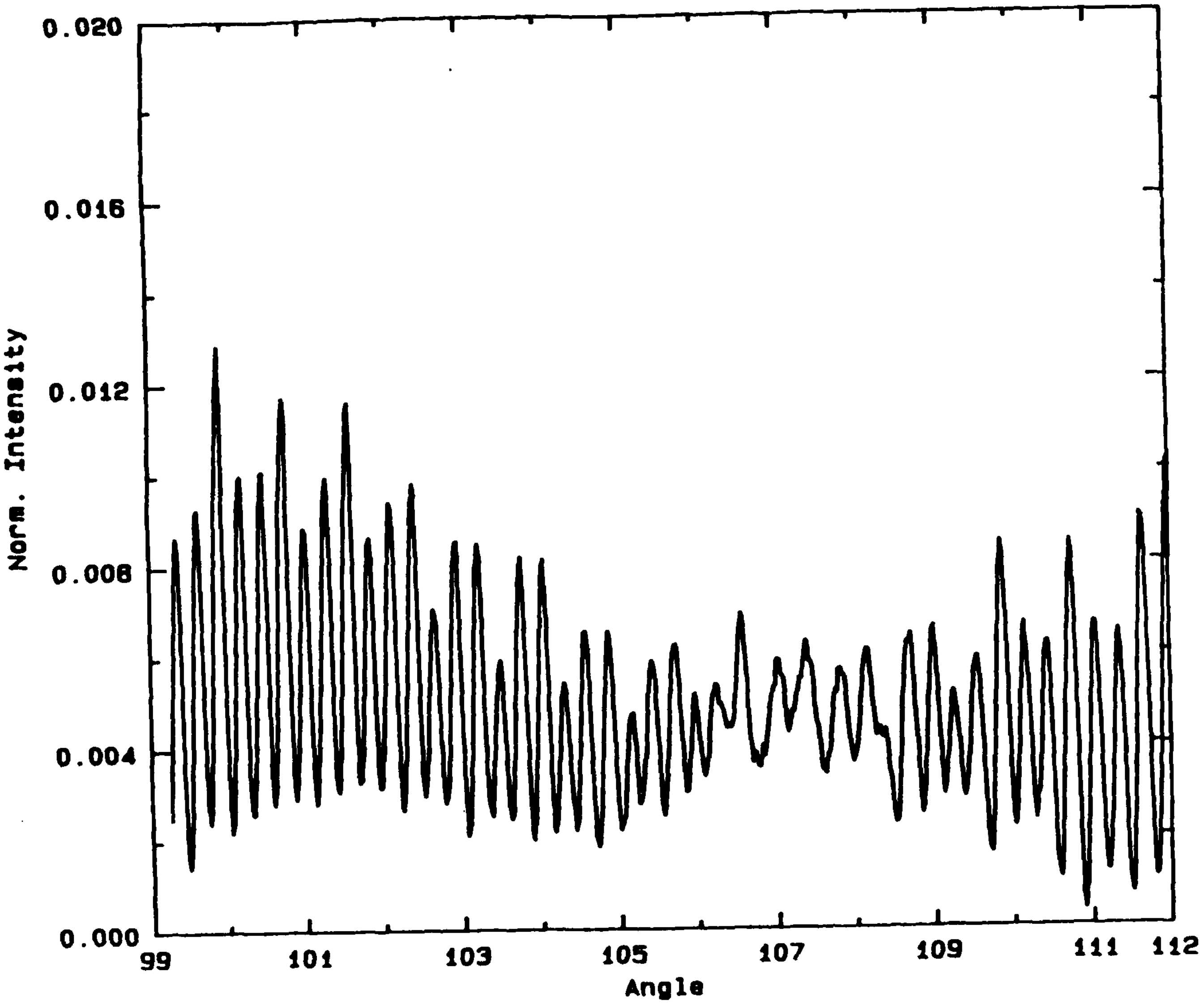
0.020
0.016
0.012
0.008
0.004
0.000
Norm. Intensity
99
101
103
105
107
109
111
112
Angle

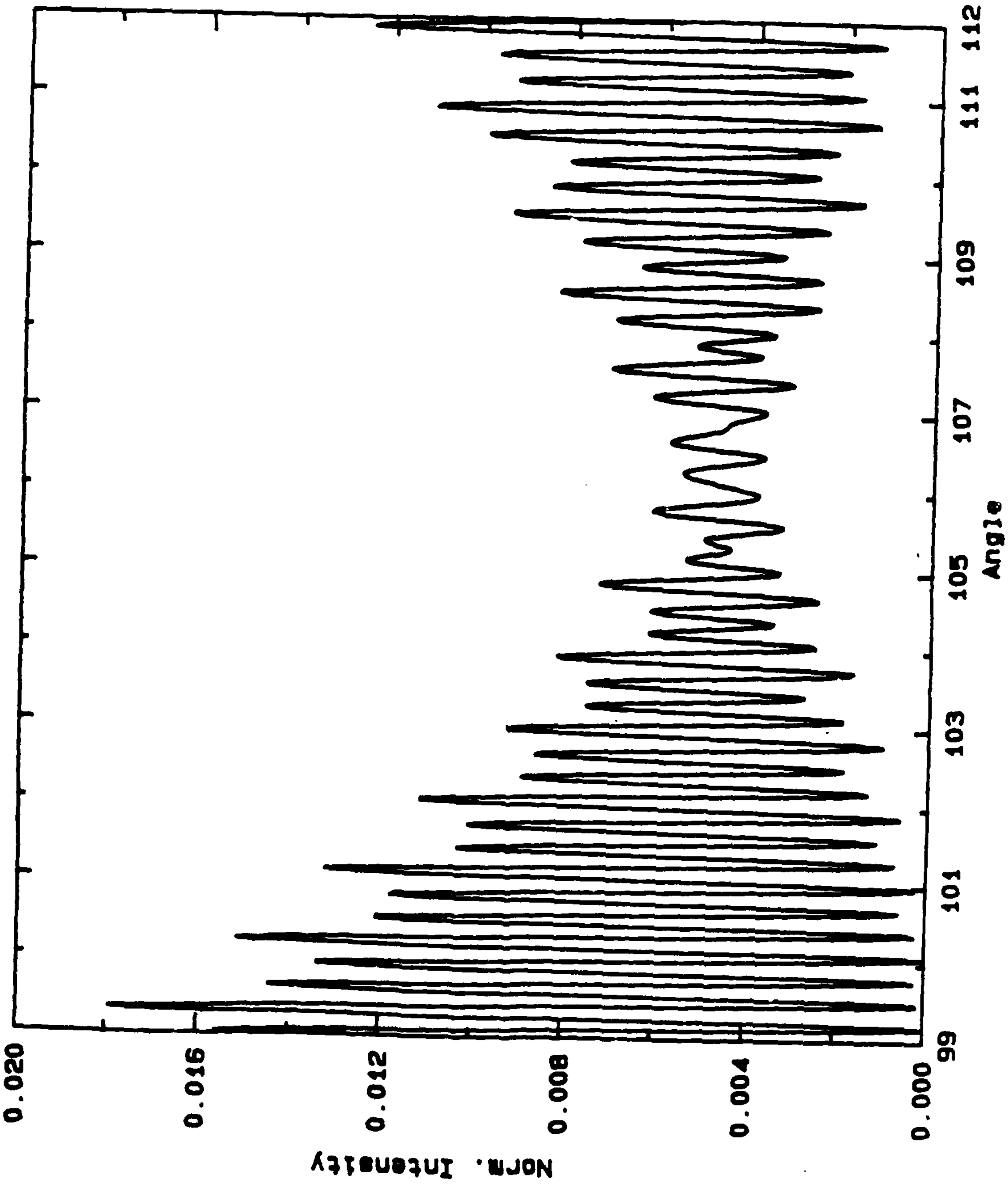

Figure A5.2a

Norm. Intensity
0.000
0.004
0.008
0.012
0.016
0.020
Angle
99
101
103
105
107
109
111
112

Figure A5.2b

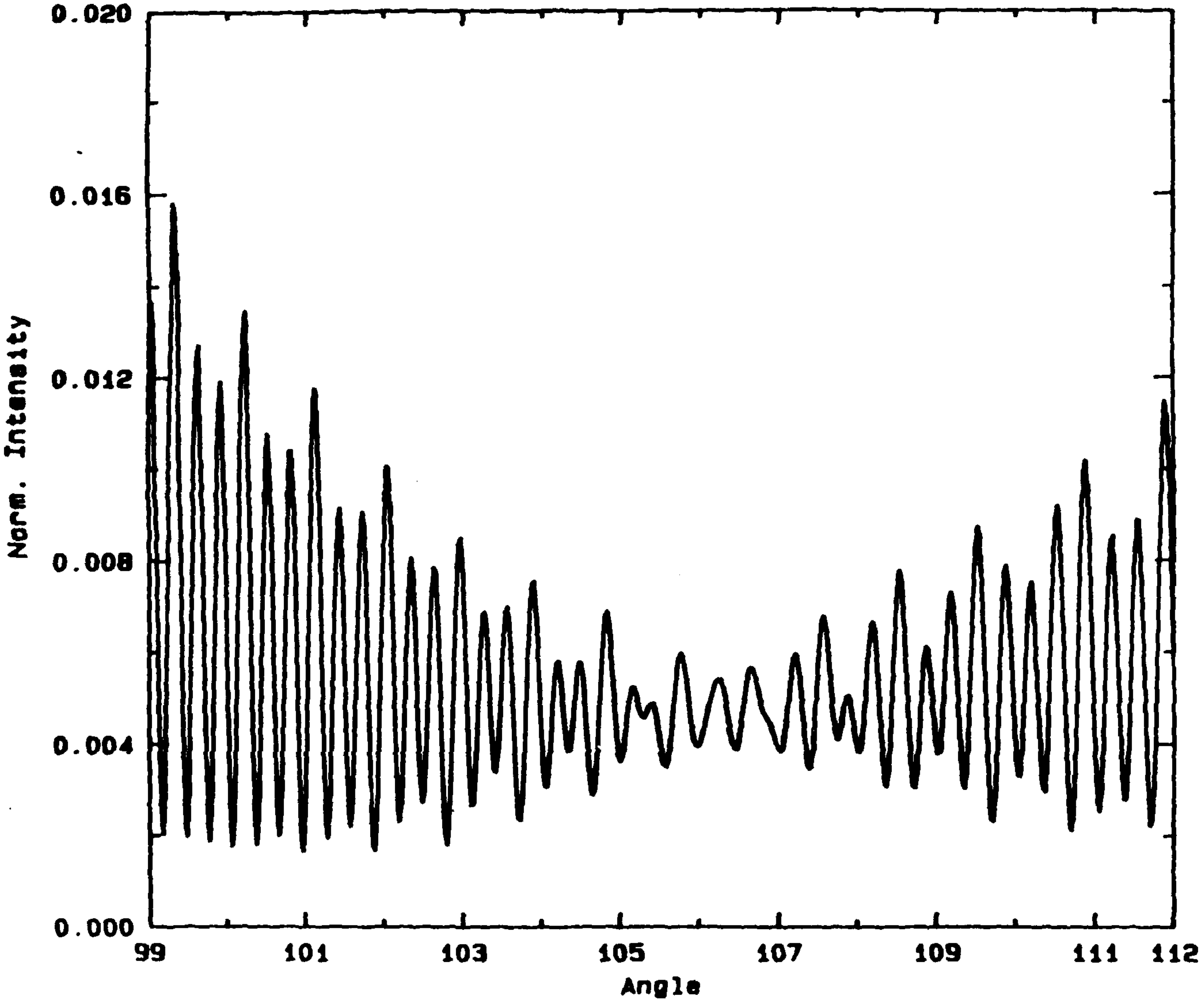
0.020
0.016
0.012
0.008
0.004
0.000
Norm. Intensity
99
101
103
105
107
109
111
112
Angle

BLANK

Figure A6.1a: Experimental data, ka = 1001, a = 61.5 μm, 135 mm lens, two point averaged, scaled to the non averaged Mie theory result.

Figure A6.2a: Mie theory result, ka = 1001, non averaged.

Figure A6.1b: Experimental data as in figure A6.1a, but scaled to the averaged Mie theory result.

Figure A6.2b: Mie theory result as in figure A6.2a, but two point averaged.

Figure A6.1a

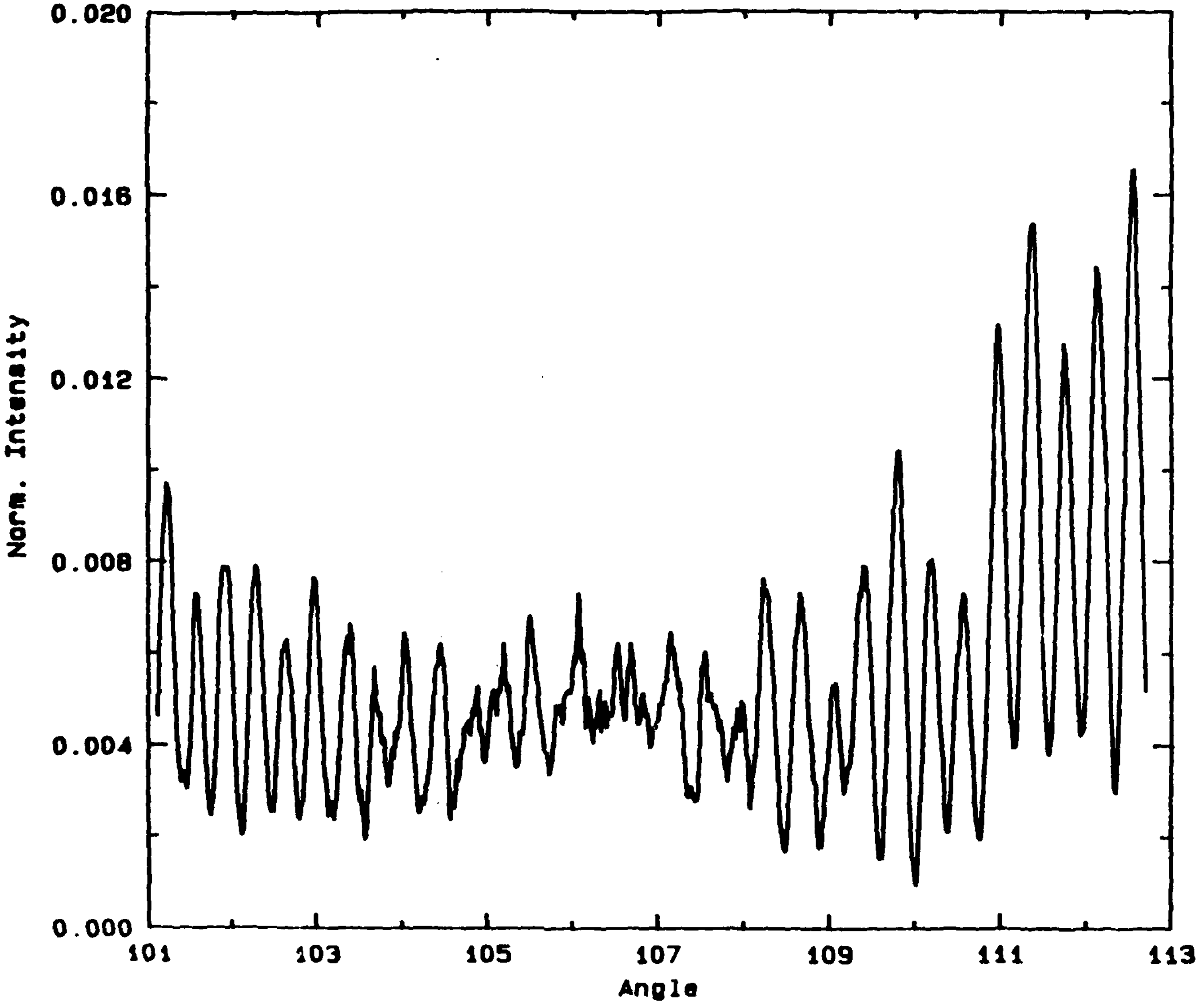
Norm. Intensity
0.020
0.016
0.012
0.008
0.004
0.000
101
103
105
107
109
111
113
Angle

Figure A6.1b

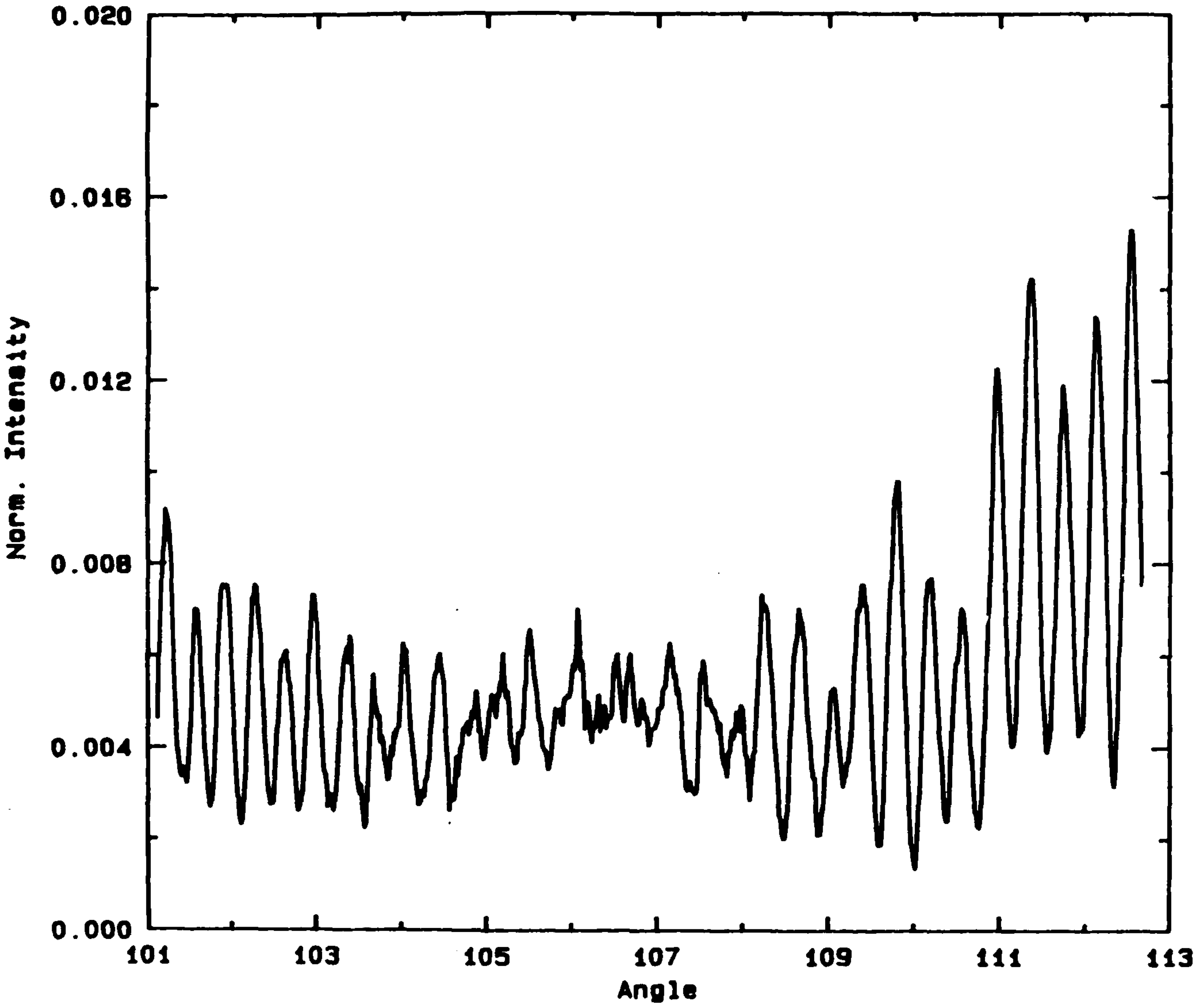
0.020
0.016
0.012
0.008
0.004
0.000
Norm. Intensity
101
103
105
107
109
111
113
Angle

Figure A6.2a

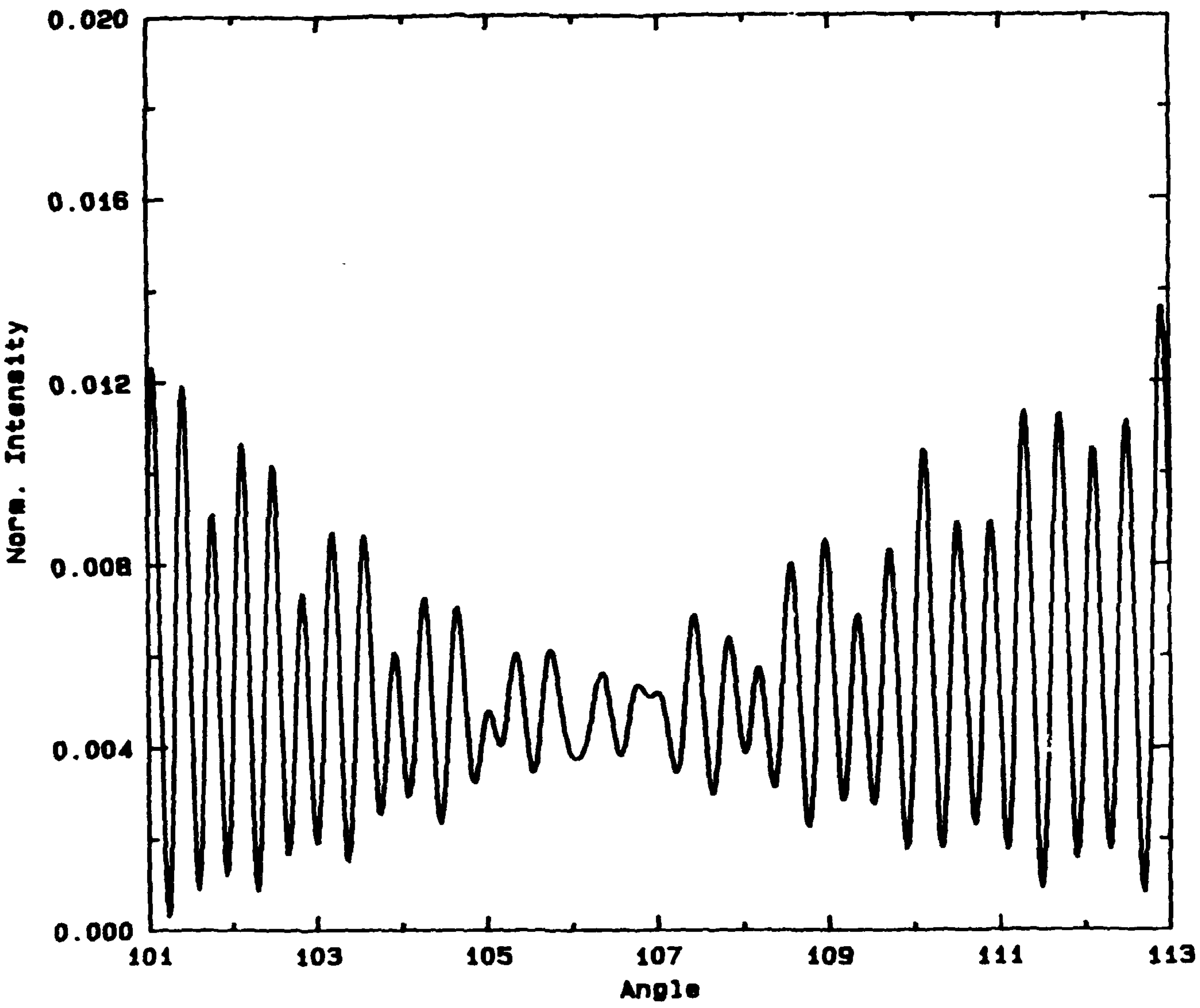
0.020
0.016
0.012
0.008
0.004
0.000
Norm. Intensity
101
103
105
107
109
111
113
Angle

Figure A6.2b

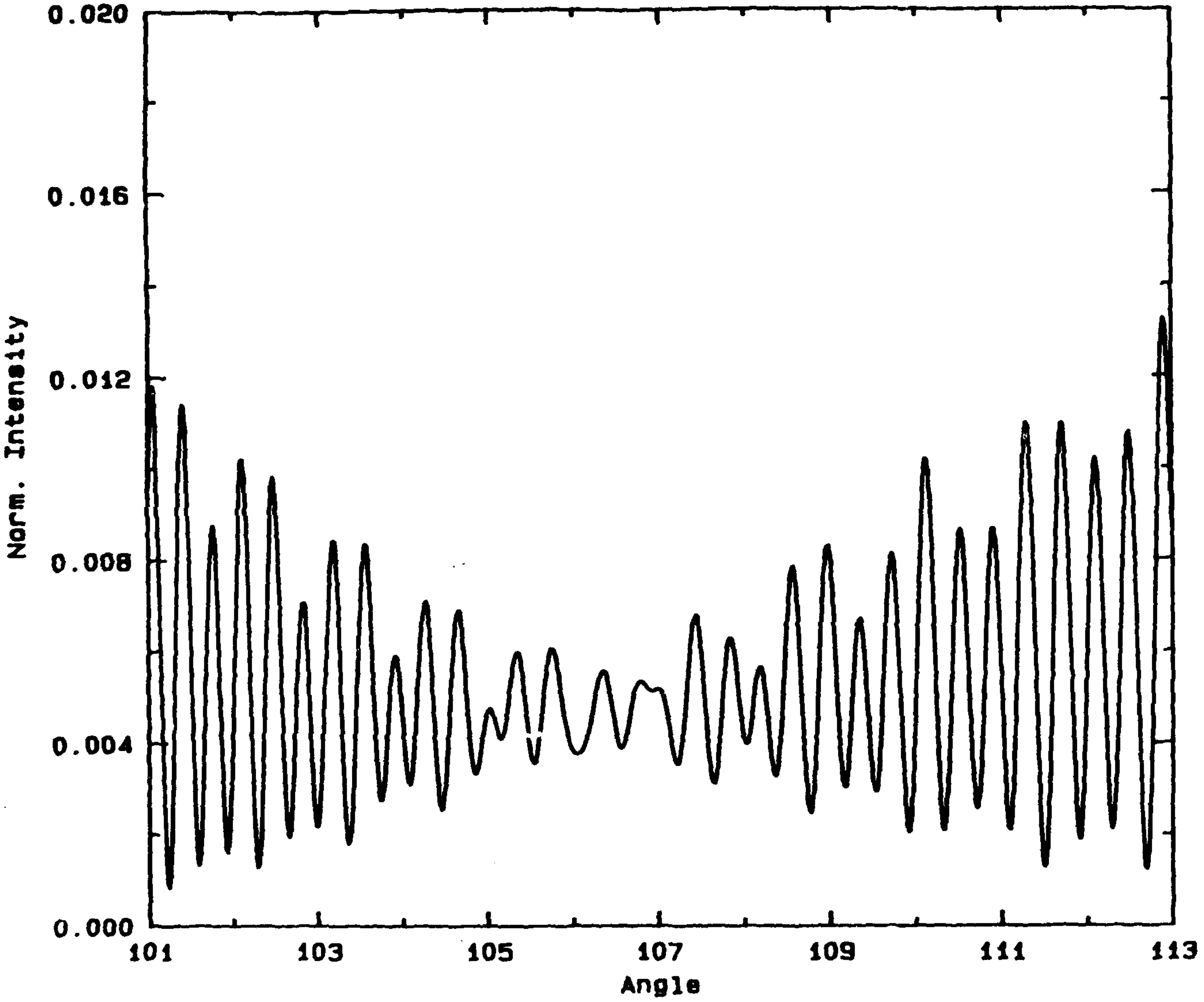
0.020
0.016
0.012
0.008
0.004
0.000
Norm. Intensity
101
103
105
107
109
111
113
Angle

REPORT DISTRIBUTION LIST

Dr. Logan E. Hargrove
Physics Division - Code 1112
Office of Naval Research
Arlington, VA 22217-5000

Defense Technical Information Center
Cameron Station
Alexandria, VA 22314 (2 copies)

Professor Robert E. Apfel
Yale University
P.O. Box 2159
New Haven, CT 06520

Professor Anthony A. Atchley
Department of Physics - Code 61AY
Naval Postgraduate School
Monterey, CA 93943-5000

Professor Lawrence A. Crum
National Center for Physical Acoustics
P.O. Box 847
University, MS 38677

Professor Robert E. Green
Materials Science and Engineering
The Johns Hopkins University
Baltimore, MD 21218

Dr. Roger H. Hackman
Code 4120
Naval Coastal Systems Center
Panama City, FL 32407-5000

Professor Edward C. Monahan
Marine Sciences Institute
University of Connecticut
Avery Point
Groton, CT 06340

Professor Andrea Prosperetti
Department of Mechanical Engineering
John Hopkins University
Baltimore, MD 21218

Dr. Richard W. Spinrad
Ocean Optics - Code 112540
Office of Naval Research
Arlington, VA 22217-5000

Ming-Yang Su
Code 331
Naval Ocean Research & Development Activity
NSTL Station, MS 39529-5004